J. Fluid Mech. (1991), *vol.* 225, *pp.* 21–80
Printed in Great Britain

Steady compressible flow of cohesionless granular materials through a wedge-shaped bunker

By J. RAVI PRAKASH† AND K. KESAVA RAO
Department of Chemical Engineering, Indian Institute of Science, Bangalore-560012, India

(Received 9 October 1989 and in revised form 30 April 1990)

A continuum model based on the critical-state theory of soil mechanics is used to generate stress, density, and velocity profiles, and to compute discharge rates for the flow of granular material in a mass flow bunker. The bin–hopper transition region is idealized as a shock across which all the variables change discontinuously. Comparison with the work of Michalowski (1987) shows that his experimentally determined rupture layer lies between his prediction and that of the present theory. However, it resembles the former more closely. The conventional condition involving a traction-free surface at the hopper exit is abandoned in favour of an exit shock below which the material falls vertically with zero frictional stress. The basic equations, which are not classifiable under any of the standard types, require excessive computational time. This problem is alleviated by the introduction of the Mohr–Coulomb approximation (MCA). The stress, density, and velocity profiles obtained by integration of the MCA converge to asymptotic fields on moving down the hopper. Expressions for these fields are derived by a perturbation method. Computational difficulties are encountered for bunkers with wall angles $\theta_w \geqslant 15°$; these are overcome by altering the initial conditions. Predicted discharge rates lie significantly below the measured values of Nguyen *et al.* (1980), ranging from 38% at $\theta_w = 15°$ to 59% at $\theta_w = 32°$. The poor prediction appears to be largely due to the exit condition used here. Paradoxically, incompressible discharge rates lie closer to the measured values. An approximate semi-analytical expression for the discharge rate is obtained, which predicts values within 9% of the exact (numerical) ones in the compressible case, and 11% in the incompressible case. The approximate analysis also suggests that inclusion of density variation decreases the discharge rate. This is borne out by the exact (numerical) results – for the parameter values investigated, the compressible discharge rate is about 10% lower than the incompressible value. A preliminary comparison of the predicted density profiles with the measurements of Fickie *et al.* (1989) shows that the material within the hopper dilates more strongly than predicted. Surprisingly, just below the exit slot, there is good agreement between theory and experiment.

1. Introduction

The handling and storage of granular materials such as coal, food grains, plastic beads, and catalyst pellets are operations which are commonly encountered in various industries (Jenike 1964*a*, p. 1; Marchello 1976; Shamlou 1988, p. 1). Though considerable industrial experience has accumulated over the years, the theoretical description of granular flow is still in its infancy. Here we discuss some theoretical aspects of one problem, namely the flow of granular materials through a bunker.

† Present address: Chemical Engineering Division, National Chemical Laboratory, Pune 411 088, India.

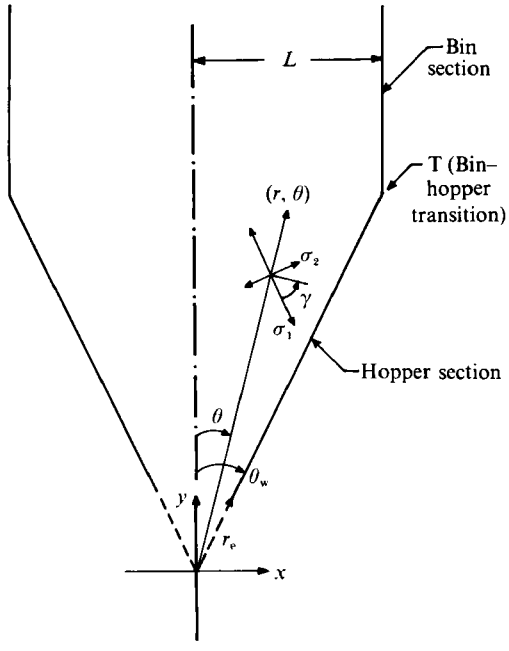

FIGURE 1. Coordinate systems used for a mass-flow bunker. Cartesian coordinates (x, y) in the bin section and polar coordinates (r, θ) in the hopper section. σ_1 = major principal stress, σ_2 = minor principal stress.

A bunker consists of a box-like 'bin' section, mounted above a 'hopper' section, as shown in figure 1. The bunker is filled from above and the material is allowed to discharge through a slot at the bottom. It is desired to predict the rate of discharge of material from the bunker, and also the forces acting on its walls.

With free-flowing materials, such as coarse sand and glass beads, two regimes of flow are observed, depending on the slope of the hopper walls, and the amount of material in the bunker (Nguyen, Brennen & Sabersky 1980). These are called 'mass flow' and 'funnel flow', respectively. In mass flow, the motion of all the material in the bunker is fairly uniform, whereas in funnel flow, there is a central core of rapidly moving material, surrounded by 'dead' regions adjacent to the bunker walls, where the material is either stagnant or moves very slowly. The mass-flow regime appears to be less complex, and hence will be the focus of this work.

The evolution of flow patterns in mass-flow bunkers has been the subject of a number of experimental studies, such as those of Blair-Fish & Bransby (1973), Lee, Cowin & Templeton (1974), and Michalowski (1984, 1987). Some of the relevant observations are briefly summarized below.

When the exit slot is opened, thin regions called 'rupture surfaces' form, across which the density and velocity change sharply. These surfaces originate from the edges of the discharge slot, and gradually spread upwards. During the initial stages of flow, the hopper is criss-crossed by a pattern of rupture surfaces, which are seen from radiographs to be thin bands of dilated or loosely packed material sandwiched between blocks of denser material. This pattern is confined to the hopper section; for some reason, it does not propagate far into the bin section of the bunker. Thus rupture surfaces are trapped at the bin–hopper transition. At the moment, there is no convincing physical explanation for this phenomenon.

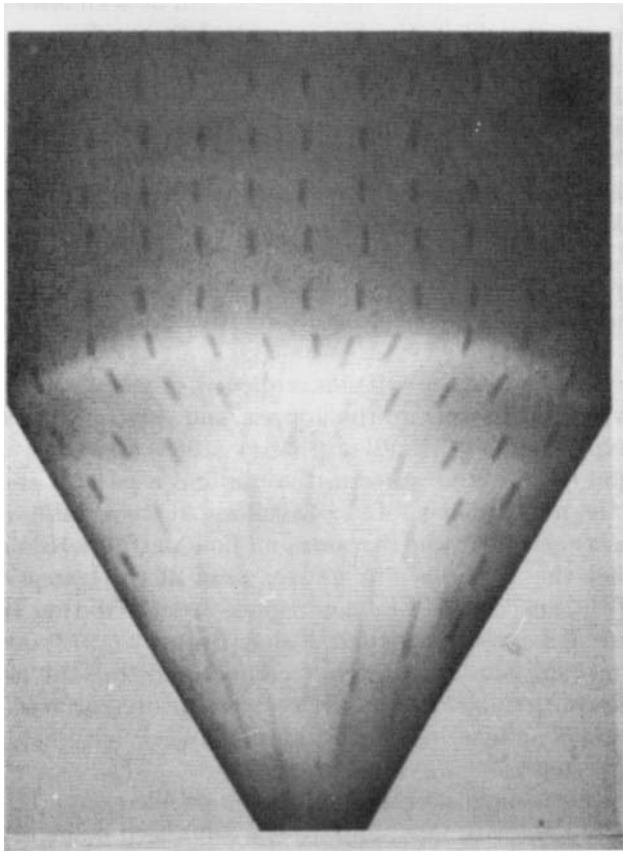

FIGURE 2. Radiograph of sand flowing through a bunker ($\theta_w = 30°$). Reproduced from Lee *et al.* (1974) with permission from John Wiley and Sons. Dark regions indicate material having a higher bulk density. The streaks are trajectories of lead shot, used as marker particles.

In the advanced stages of flow, the rupture surfaces in the lower part of the hopper fade out, leaving a single surface separating dense material in the bin from dilated material in the hopper. This may be seen from the radiograph of Lee *et al.* (1974) (figure 2), where dark regions indicate material having a higher bulk density. The density of the material in the bin appears to remain close to its initial (poured) value; however, Michalowski (1987) has observed a mild dilation for initially dense materials.

The streaks in figure 2 are trajectories of lead shot, which were used as marker particles. Based on this and other evidence (Nedderman & Laohakul 1980), we have the following picture of the velocity field in a bunker. Particles moves vertically downwards in the bin with constant speed, except for narrow shear zones adjacent to the bin walls. In the hopper section, they move radially towards the exit slot, at least when the hopper walls are steep.

So far, we have discussed the kinematics of flow through bunkers. A few remarks about wall stresses are now in order. The experiments of Blair-Fish & Bransby (1973), Rao & Venkateswarlu (1974), Clague (quoted in Blight 1986), Manjunath (1988), and others show that the normal stress on the wall increases on moving downwards from the upper surface of the fill. If the height of fill in the bin section is large compared to the lateral dimensions of the bunker, the normal stress tends to

attain a constant value as the depth increases. It will be seen later that the existence of an asymptotic stress field in the bin is central to our formulation of boundary conditions for a steady-state problem.

The normal stress shows a sharp increase or peak at the bin–hopper transition, and then begins to decrease along the hopper wall. It is believed that the peak in stress occurs because the orientation of the major principal stress switches from an 'active' or nearly vertical state in the bin, to a 'passive' or nearly horizontal state in the hopper (Jenike & Johanson 1968; Bransby & Blair-Fish 1974). Jenike & Johanson (1968) attribute this change to the dilation of the material as it flows through the hopper, causing a horizontal compression; this in turn tends to increase the magnitude of the horizontal normal stress relative to that of the vertical normal stress.

It is conjectured that when the exit slot is opened, a 'switch wave' which separates active and passive states travels up the hopper, and gets trapped at the bin–hopper transition. The experiments of Handley & Perry (1967) and Perry & Handley (1967) support the notion of an active state in the bin and a passive state in the hopper. However, there is no evidence of a travelling switch wave in the literature. Simultaneous observations of wall stresses and flow patterns (Blair-Fish & Bransby 1973) suggests that the occurrence of a stress peak at the transition coincides with the formation of rupture surfaces in this region, at least during the initial stage of flow. In the advanced stage of flow, Blair-Fish & Bransby (1973) observed oscillatory wall stresses in the transition region. They conjectured that the oscillations may be related to the intermittent growth and decay of rupture surfaces. However, in the absence of continuous monitoring of the velocity and density fields, it is difficult to draw a firm conclusion.

The above discussion suggests that the bunker problem may be viewed from two angles: (*a*) the initial stage of flow, and (*b*) the advanced stage of flow. The former involves the formation and growth of rupture layers, and the initiation of flow. So far, no attempts have been made to model this behaviour. As it appears to be a formidable problem, we shall examine only the advanced stage of flow, where one can consider a single, fully developed rupture layer separating dense material in the bin from loose material in the hopper. Even with this simplification, the use of a steady-state analysis is suspect if wall stresses usually oscillate, in the manner reported by Blair-Fish & Bransby (1973). However, it is intuitively expected that some of the gross features of the stress and velocity fields will be revealed by a steady-state approach. This is in keeping with Jenike's remark that 'in mass flow hoppers, oscillations are slight' (Jenike 1987). Further, such models have not yet been carefully examined; indeed, there do not appear to have been any attempts to simultaneously predict the stress, density, and velocity fields in a mass-flow bunker.

With the above considerations in mind, we shall confine attention to a steady-state analysis based on a continuum model. Though the bulk of the literature on granular flow is concerned with continuum models, discrete models have also begun to appear (Campbell & Brennen 1985). Some of the other assumptions used here are discussed below; the rest will be indicated later.

(i) The material will be regarded as cohesionless, i.e. one that cannot support tensile normal stresses. Materials such as coarse sand, seeds, and glass beads fall into this category, whereas fine powders such as cement and cracking catalyst usually exhibit some amount of cohesion. Though the latter are industrially important materials, we shall confine attention to cohesionless materials as the theory is simpler and contains fewer parameters.

(ii) Assuming that the distance between the front and back faces of the bunker is large compared with the other dimensions, the flow may be regarded as being parallel to these faces. Further, the variation in all the field variables perpendicular to the plane of flow may be considered negligible. The assumption of plane flow greatly simplifies the form of the constitutive relations and reduces the number of dependent variables. To the best of our knowledge, there have been no attempts to solve truly three-dimensional granular-flow problems. However, Schaeffer & Pitman (1988) have recently examined some aspects of such problems.

(iii) Though the bulk of the literature on bunker flow is concerned with incompressible analyses (Savage 1965; Davidson & Nedderman 1973; Brennen & Pearce 1978; Kaza & Jackson 1982*a*, *b*; Meric & Tabarrok 1982), the effect of density variation will be included in our work for the following reasons: (*a*) as discussed earlier, the density of the material in the bin section is likely to be different from that in the hopper section, and (*b*) density measurements in hoppers and bins (Bosley, Schofield & Shook 1969; Blair-Fish & Bransby 1973; Van Zuilichem, Van Egmond & de Swart 1974; Lee *et al.* 1974; Tüzün & Nedderman 1982; Michalowski 1984, 1987; Fickie, Mehrabi & Jackson 1989) show that there is a marked dilation in the vicinity of the exit slot. One other reason is discussed below.

Though a frictional theory will be used here, it appears that momentum transfer by collisions between particles may also be important in certain parts of the flow field. It is felt intuitively that frictional effects are important in slow flows at high densities, whereas collisional effects are important in rapid flows at lower densities (Sayed & Savage 1983; Savage *et al.* 1983; Johnson & Jackson 1987). Hence a comprehensive frictional–collisional theory must allow for density variation. The present work may therefore be regarded as a precursor to the eventual inclusion of collisional effects.

It is the purpose of this work to predict the stress, density, and velocity fields in a bunker, and to assess the importance of compressibility effects. To this end, we now turn to the basic equations.

2. Basic equations

2.1. *Balance laws*

Using polar coordinates with origin at the vertex of the hopper (figure 1), and confining attention to plane flow, the balance laws for steady flow take the form

Continuity

$$\frac{1}{r}\frac{\partial}{\partial r}(r\rho v_r)+\frac{1}{r}\frac{\partial}{\partial\theta}(\rho v_\theta)=0, \tag{1}$$

Momentum balance (r-component)

$$\rho\left[v_r\frac{\partial v_r}{\partial r}+\frac{v_\theta}{r}\frac{\partial v_r}{\partial\theta}-\frac{v_\theta^2}{r}\right]+\frac{1}{r}\frac{\partial}{\partial r}(r\sigma_{rr})+\frac{1}{r}\frac{\partial}{\partial\theta}(\sigma_{r\theta})-\frac{\sigma_{\theta\theta}}{r}+\rho g\cos\theta=0, \tag{2}$$

Momentum balance (θ-component)

$$\rho\left[v_r\frac{\partial v_\theta}{\partial r}+\frac{v_\theta}{r}\frac{\partial v_\theta}{\partial\theta}+\frac{v_r v_\theta}{r}\right]+\frac{1}{r^2}\frac{\partial}{\partial r}(r^2\sigma_{r\theta})+\frac{1}{r}\frac{\partial}{\partial\theta}(\sigma_{\theta\theta})-\rho g\sin\theta=0. \tag{3}$$

Here $\rho\equiv\rho_s\epsilon_s$ is the bulk density, where ρ_s is the density of the solid, which is assumed to be constant and ϵ_s is the volume fraction occupied by the solid; σ_{rr}, $\sigma_{r\theta}$,

and $\sigma_{\theta\theta}$ are the components of the stress tensor, which is defined in the compressive sense; v_r and v_θ are the radial and circumferential components of velocity, respectively; and g is the acceleration due to gravity.

2.2. *Constitutive models*

At present, there appear to be three broad types of constitutive models for describing granular flow in various geometries (Tüzün *et al.* 1982; Savage *et al.* 1983; Jackson 1986):

(*a*) kinematic models;

(*b*) 'rate independent' or frictional models based on plasticity theory and soil mechanics;

(*c*) 'rate dependent' or collisional models based on the kinetic theory of gases.

Before discussing some features of these models, we note that none of them is wholly satisfactory or even superior to the others in all respects. Perhaps this reflects the present level of development of the theory.

Kinematic models are 'incomplete' in the sense that they provide no information about stresses. Nevertheless, they have been reasonably successful in predicting velocity profiles in the 'converging-flow' zone of the flat-bottomed bins (Tüzün & Nedderman 1979). They will not be pursued here, as it is not clear how they should be modified to account for density variation, and to predict the stress field.

Frictional models have been in use for over two decades. The results of these studies show that the models can predict some, but not all, of the phenomena observed when granular materials flow through hoppers and bunkers (see for example, Blair-Fish & Bransby 1973; Spink & Nedderman 1978; Meric & Tabarrok 1982; Bridgwater & Scott 1983; Jackson 1983; Michalowski 1984; Nedderman 1988).

Apart from the pioneering work of Bagnold (1954), collisional models have been explored largely from the 1970's onwards. They can predict some features of plane shear between parallel plates, and of flow down inclined planes (Ackermann & Shen 1982; Savage 1983). More recently, hybrid frictional–collisional models have been developed and applied to these problems, with encouraging results (Sayed & Savage 1983; Johnson & Jackson 1987). Both the collisional and frictional–collisional equations are formidable, and have yet to be used for two-dimensional problems such as bunker flow.

In view of the above discussion, attention will be confined to frictional equations. For an account of the physical motivation behind these equations, see for example Jenike (1964*a*), Schofield & Wroth (1968), Atkinson & Bransby (1978), and Jackson (1983). Even though they are older than their collisional counterparts, and have been used more frequently, the present status is such that there is still ample scope for a detailed examination of certain aspects.

2.3. *Frictional constitutive equations*

Frictional equations are composed of two elements, namely yield conditions and flow rules. It is assumed that the flowing material satisfies a yield condition of the form (Naylor 1978)

$$F_0(\boldsymbol{\sigma}, \mu) = 0, \tag{4}$$

where F_0 is a scalar function of the stress tensor $\boldsymbol{\sigma}$ and a 'hardening parameter' μ. The literature contains several choices for μ, such as the plastic work (Hill 1950, p. 25), the plastic volumetric strain, or equivalently, the density (Roscoe, Schofield & Wroth 1958; Roscoe & Burland 1968; Zienkiewicz, Humpheson & Lewis 1977; Naylor 1978), and the total plastic strain (Hill 1950, p. 30; Desai & Siriwardane 1984,

p. 379). Here we set $\mu = \rho$, the bulk density, in keeping with the critical-state theory of soils (Schofield & Wroth 1968; Jackson 1983). Assuming that the material is isotropic, (4) may be rewritten as

$$F_1(\sigma_1, \sigma_2, \sigma_3, \rho) = 0, \tag{5}$$

where F_1 is a symmetric function of the principal stresses σ_1, σ_2 and σ_3 (Hill 1950, pp. 15, 16).

The yield condition does not directly give any information about the kinematics of motion at yield. This is provided by the flow rule. The plastic potential flow rule assumes that the rate-of-deformation tensor depends only on the stress tensor and a hardening parameter, such as the bulk density. Under this assumption, it can be shown that the principal axes of stress and rate-of-deformation or strain-rate tensors coincide (Hunter 1983, pp. 136, 137). This is called the coaxiality condition (Mroz & Szymanski 1978; Spencer 1982; Jackson 1983).

In terms of principal values, the plastic potential flow rule for an isotropic material is generally assumed to be given by (Drucker & Prager 1952; Mroz & Szymanski 1978; Jackson 1983; Hunter 1983, p. 481)

$$c_i = \lambda \frac{\partial Q_1}{\partial \sigma_i}; \quad i = 1, 2, 3, \tag{6}$$

where c_1, c_2, and c_3 are the principal compressive strain rates, i.e. the principal values of the rate-of-deformation tensor, defined in the compressive sense, $Q_1(\sigma_1, \sigma_2, \sigma_3, \rho)$ is a scalar function called the plastic potential, and λ is a scalar factor of proportionality. Since λ has to be determined as a part of the solution, (6) constitutes only two independent relations between the principal strain rates, the principal stresses, and the density. For a discussion of other types of flow rules, see Mroz & Szymanski (1978) and Spencer (1982).

For plane flow, it is easy to show that one of the principal axes of the rate-of-deformation tensor must be perpendicular to the plane of flow. Consequently, the other two principal axes, say the c_1 and c_2 axes, must lie in the plane of flow and, on account of coaxiality, two of the principal stress axes, say the σ_1, and σ_2 axes, are similarly disposed. Since $c_3 = 0$ for plane flow, (6) implies that

$$\frac{\partial Q_1}{\partial \sigma_3} = 0. \tag{7}$$

Using (7) to eliminate σ_3, (5) may be rewritten as

$$F_2(\sigma_1, \sigma_2, \rho) = 0. \tag{8}$$

An illustration of this procedure is given in Prakash & Rao (1988).

It is convenient to express the principal stresses in terms of the invariants

$$\sigma = \tfrac{1}{2}(\sigma_1 + \sigma_2); \quad \tau = \tfrac{1}{2}(\sigma_1 - \sigma_2); \quad \sigma_1 \geqslant \sigma_2, \tag{9}$$

which are called the mean stress and the deviatoric stress, respectively. In terms of σ and τ, the yield condition for plane flows (8) takes the form

$$f(\tau, \sigma, \rho) = F_2(\sigma + \tau, \sigma - \tau, \rho) = 0. \tag{10}$$

Similarly, the flow rule (6) may be rewritten as

$$c_i = \lambda \frac{\partial Q_2}{\partial \sigma_i}; \quad i = 1, 2, \tag{11}$$

where $Q_2(\sigma_1, \sigma_2, \rho)$ is a 'two-dimensional' plastic potential which is obtained from the 'three-dimensional' plastic potential $Q_1(\sigma_1, \sigma_2, \sigma_3, \rho)$ by using (7) to eliminate σ_3. Introducing an alternative plastic potential $q(\tau, \sigma, \rho)$, defined by

$$q(\tau, \sigma, \rho) \equiv Q_2(\sigma+\tau, \sigma-\tau, \rho) \tag{12}$$

and the angle of dilation ν (Roscoe 1970), defined by

$$\sin\nu \equiv -\frac{(c_1+c_2)}{(c_1-c_2)}, \tag{13}$$

the flow rule for plane flows (11) may be rewritten as

$$\sin\nu = -\frac{(\partial q/\partial\sigma)}{(\partial q/\partial\tau)}. \tag{14}$$

In polar coordinates, the coaxiality condition takes the form (Jackson 1983; Prakash & Rao 1988)

$$\cos 2\gamma\left[\frac{\partial v_\theta}{\partial r}+\frac{1}{r}\frac{\partial v_r}{\partial\theta}-\frac{v_\theta}{r}\right]-\sin 2\gamma\left[\frac{\partial v_r}{\partial r}-\frac{1}{r}\frac{\partial v_\theta}{\partial\theta}-\frac{v_r}{r}\right]=0, \tag{15}$$

where γ is the angle that the major principal stress axis makes with the circumferential direction (figure 1). Similarly, (13) may be rewritten as

$$\cos 2\gamma\left[\frac{\partial v_r}{\partial r}+\frac{1}{r}\frac{\partial v_\theta}{\partial\theta}+\frac{v_r}{r}\right]-\sin\nu\left[\frac{\partial v_r}{\partial r}-\frac{1}{r}\frac{\partial v_\theta}{\partial\theta}-\frac{v_r}{r}\right]=0. \tag{16}$$

Equation (16) is the flow rule for plane flows, with $\sin\nu$ given by (14).

The specific forms used here for the yield condition and the plastic potential will now be described. The choice of forms is guided to some extent by the critical-state theory of soils (Roscoe *et al.* 1958; Schofield & Wroth 1968; Atkinson & Bransby 1978; Jackson 1983). Central to this theory is the concept of 'critical' states, which permit isochoric deformation at constant values of σ and τ. The value of the mean stress σ at a critical state, henceforth denoted by σ_c, is found to be a function of the density ρ. Noting that the yield condition (10) may be represented by yield loci or contours of constant ρ in the (σ, τ)-plane, and assuming that these loci are similar in shape (see for example Roscoe *et al.* 1958), (10) may be rewritten as

$$f \equiv \frac{\tau}{\sigma_c(\rho)} - h(\alpha) = 0; \quad \alpha \equiv \frac{\sigma}{\sigma_c(\rho)}. \tag{17}$$

The yield condition (17) maps as a single curve in the $(\alpha, \tau/\sigma_c)$-plane, with the critical state given by the point $\alpha = 1, \tau/\sigma_c = h(1)$. The segment of the yield locus with $\alpha < 1$ is called the dilation branch, since it is found that for stress states in this segment, deformation is accompanied by a decrease in density. Similarly, the segment with $\alpha > 1$ is called the compaction branch, since deformation leads to an increase in density.

The functions $\sigma_c(\rho)$ and $h(\alpha)$ are taken to be

$$\sigma_c(\rho) \equiv p_a \exp\left[\frac{\Gamma_1\rho-\rho_s}{\lambda_1\rho}\right] \tag{18}$$

or equivalently
$$\frac{1}{\epsilon_s} = \Gamma_1 - \lambda_1 \ln\left[\frac{\sigma_c}{p_a}\right] \tag{19}$$

and
$$h(\alpha) \equiv \sin\phi[n\alpha - n_1(\alpha)^{n/n_1}]; \quad n_1 \equiv n-1, \tag{20}$$

where p_a is the atmospheric pressure, used as a convenient non-dimensionalizing parameter (since wall stress in laboratory-scale bunkers rarely exceeds p_a in magnitude, Bridgwater & Scott 1983). The parameters Γ_1, λ_1, n and the angle of internal friction ϕ are material parameters. Equation (18) is taken from soil mechanics literature (see for example, Atkinson & Bransby 1978, pp. 190, 191), while some justification for (20) is given in our earlier work (Prakash & Rao 1988).

Turning to the choice of the plastic potential q, we note that (14) represents an 'associated' flow rule (Naylor 1978) if
$$q = f, \tag{21}$$
where f is the yield condition. Otherwise it represents a 'non-associated' flow rule. The following points may be noted regarding these two types of flow rules: (*a*) data on the stress–strain behaviour of clays such as Kaolin and Weald clay (Roscoe & Burland 1968) support the use of the associated flow rule for the compaction branch of the yield locus, (*b*) the behaviour of dense specimens of sand (Lade & Duncan 1975; Bolton 1986) suggests the use of a non-associated flow rule for the dilation branch, (*c*) the dilatancy of certain rocks can be modelled using the associated flow rule for the dilation branch (Gerogiannopoulos & Brown 1978), and (*d*) by definition, the rate of dilation must vanish at a critical state, regardless of the choice of flow rules. Thus solutions obtained with associated and non-associated flow rules are likely to be close together in the vicinity of critical states.

The above discussion suggests that the choice of plastic potentials depends on the nature of the material, and, for a given material, on whether it is compacting or dilating. To simplify the analysis, and to avoid switching frequently between the two types of flow rules, only one will be used for both the branches. At present, very little is known about the nature of solutions to bunker problems, under either type of flow rule.

We start with an associated flow rule, given by (14), (17)–(21), and later modify it because of computational difficulties. As discussed later, the modified equations are effectively equivalent to those based on a non-associated flow rule.

2.4. *Equations in dimensionless form*

It is convenient to express the stress components in terms of the Sokolovskii variables σ, τ and γ:
$$\sigma_{rr} = \sigma - \tau\cos 2\gamma; \quad \sigma_{r\theta} = -\tau\sin 2\gamma; \quad \sigma_{\theta\theta} = \sigma + \tau\cos 2\gamma, \tag{22}$$
where σ and τ are defined by (9), and γ is the orientation of the major principal stress axis relative to the circumferential direction.

Introducing dimensionless variables
$$r^* = \frac{r}{L}, \quad \rho^* = \frac{\rho}{\rho_{max}}, \quad v_r^* = \frac{v_r}{(gL)^{\frac{1}{2}}}, \quad v_\theta^* = \frac{v_\theta}{(gL)^{\frac{1}{2}}}, \quad \sigma^* = \frac{\sigma}{\rho_{max} gL},$$
$$\tau^* = \frac{\tau}{\rho_{max} gL}, \quad \sigma_c^* = \frac{\sigma_c}{\rho_{max} gL},$$
where L is the half-width of the bin (figure 1), $\rho_{max} \equiv \rho_s \epsilon_{s,max}$, and $\epsilon_{s,max}$ is the volume

fraction of the solid corresponding to close packing of uniform spheres (=0.74; Brown & Richards 1970, p. 17), the basic equations (1)–(3) and (15), (16) may be written as follows:

Continuity
$$\frac{1}{r^*}\frac{\partial}{\partial r^*}(r^*\rho^* v_r^*)+\frac{1}{r^*}\frac{\partial}{\partial\theta}(\rho^* v_\theta^*)=0; \tag{23}$$

Momentum balance (r-component)
$$\rho^*\left[v_r^*\frac{\partial v_r^*}{\partial r^*}+\frac{v_\theta^*}{r^*}\frac{\partial v_r^*}{\partial\theta}-\frac{(v_\theta^*)^2}{r^*}\right]+\frac{1}{r^*}\frac{\partial}{\partial r^*}\left[r^*(\sigma^*-\tau^*\cos 2\gamma)\right]-\frac{1}{r^*}\frac{\partial}{\partial\theta}[\tau^*\sin 2\gamma]$$
$$-\frac{\sigma^*+\tau^*\cos 2\gamma}{r^*}+\rho^*\cos\theta=0; \tag{24}$$

Momentum balance (θ-component)
$$\rho^*\left[v_r^*\frac{\partial v_\theta^*}{\partial r^*}+\frac{v_\theta^*}{r^*}\frac{\partial v_\theta^*}{\partial\theta}+\frac{v_r^* v_\theta^*}{r^*}\right]-\frac{1}{(r^*)^2}\frac{\partial}{\partial r^*}\left[(r^*)^2\tau^*\sin 2\gamma\right]$$
$$+\frac{1}{r^*}\frac{\partial}{\partial\theta}[\sigma^*+\tau^*\cos 2\gamma]-\rho^*\sin\theta=0; \tag{25}$$

Coaxiality
$$\cos 2\gamma\left[\frac{\partial v_\theta^*}{\partial r^*}+\frac{1}{r^*}\frac{\partial v_r^*}{\partial\theta}-\frac{v_\theta^*}{r^*}\right]-\sin 2\gamma\left[\frac{\partial v_r^*}{\partial r^*}-\frac{1}{r^*}\frac{\partial v_\theta^*}{\partial\theta}-\frac{v_r^*}{r^*}\right]=0; \tag{26}$$

Flow rule
$$\cos 2\gamma\left[\frac{\partial v_r^*}{\partial r^*}+\frac{1}{r^*}\frac{\partial v_\theta^*}{\partial\theta}+\frac{v_r^*}{r^*}\right]-\sin\nu\left[\frac{\partial v_r^*}{\partial r^*}-\frac{1}{r^*}\frac{\partial v_\theta^*}{\partial\theta}-\frac{v_r^*}{r^*}\right]=0; \tag{27}$$

Yield condition
$$f^*\equiv\frac{\tau^*}{\sigma_c^*(\rho^*)}-\sin\phi[n\alpha-n_1(\alpha)^{n/n_1}]=0, \tag{28}$$

where
$$\alpha=\frac{\sigma}{\sigma_c(\rho)}=\frac{\sigma^*}{\sigma_c^*(\rho^*)}, \tag{29}$$

$$\sigma_c^*(\rho^*)=\beta^*\exp\left[\frac{\Gamma\rho^*-1}{\lambda\rho^*}\right];\quad \beta^*\equiv\frac{p_a}{\rho_{\max}gL};\quad \Gamma=\Gamma_1\epsilon_{s,\max};\quad \lambda=\lambda_1\epsilon_{s,\max}; \tag{30}$$

Associated flow rule
$$\sin\nu=n\sin\phi[1-(\alpha)^{1/n_1}]. \tag{31}$$

2.5. *Structure of the basic equations*

The basic equations constitute a set of five first-order, quasi-linear partial differential equations in the dependent variables σ^*, γ, ρ^*, v_r^* and v_θ^*. They may be written in matrix form as

$$\boldsymbol{A}\frac{\partial \boldsymbol{w}}{\partial r^*}+\frac{\boldsymbol{B}}{r^*}\frac{\partial \boldsymbol{w}}{\partial\theta}+\boldsymbol{C}=0 \tag{32}$$

where $\boldsymbol{w}^{\mathrm{T}}\equiv(\rho^*, v_\theta^*, v_r^*, \sigma^*, \gamma)$, $\boldsymbol{A}$ and $\boldsymbol{B}$ are matrices whose elements are functions of $\boldsymbol{w}$, and $\boldsymbol{C}$ is a column vector containing the non-homogeneous terms in (23)–(27).

The classification of the system (32) is based on the nature of the roots (eigenvalues) of the characteristic equation

$$\det(\boldsymbol{B}-\lambda\boldsymbol{A})=0. \tag{33}$$

The system (32) is said to be hyperbolic (Courant & Hilbert 1962, pp. 173, 425; Prasad & Ravindran 1985, pp. 152, 153) if (33) has five real roots $\{\lambda_j\}$, and there are five linearly independent eigenvectors $\{\boldsymbol{l}_j\}$ such that

$$\boldsymbol{l}_j^{\mathrm{T}}(\boldsymbol{B}-\lambda_j\boldsymbol{A}) = 0; \quad j = 1,5. \tag{34}$$

In the present case, (33) has five real roots, only three of which are distinct. Denoting the distinct roots by λ_1, λ_2 and λ_3, and introducing angles ψ_i, defined by

$$\cot\psi_i \equiv \lambda_i; \quad i = 1,3, \tag{35}$$

it is found that

$$\psi_1 = \cot^{-1}(v_\theta^*/v_r^*); \quad \psi_2 = -[\gamma-(\tfrac{1}{4}\pi-\tfrac{1}{2}\nu)] \text{ (double root)};$$

$$\psi_3 = -[\gamma+(\tfrac{1}{4}\pi-\tfrac{1}{2}\nu)] \text{ (double root)}. \tag{36a, b, c}$$

It is also found that there are only three linearly independent eigenvectors corresponding to these eigenvalues. Hence the system is not hyperbolic; indeed it cannot be classified as any of the standard types.

However, some insight into its structure can be gained by decoupling the 'stress' equations (24) and (25) from the 'velocity' equations (23), (26), and (27), as follows. If the density and velocity fields are assumed to be known functions of position, it can be shown that (24) and (25) are hyperbolic. Similarly, if the mean stress σ^* and the orientation γ of the major principal stress axis are assumed to be known functions of position, (23), (26), and (27) are also hyperbolic. Thus we have two sets of hyperbolic equations, which, when coupled together by the inertial terms in (24) and (25), lead to a non-hyperbolic system. This conclusion is based on the use of an associated flow rule; as discussed later, non-associated flow rules may permit the hyperbolic character of the stress and velocity equations to be retained by the complete system of equations.

From a computational viewpoint, a non-associated flow rule appears preferable, as it leads to a hyperbolic system for which standard numerical methods are available. However, it was difficult to guess *a priori* the form of the non-associated flow rule. Further, having used an associated flow rule in our earlier work on a one-dimensional problem, we wished to study its performance in two-dimensional flows. After most of the present work was completed, a paper by Bolton (1986) was spotted, which provides a simple correlation for the angle of dilation ν. This is effectively equivalent to a non-associated flow rule, and merits consideration in hopper flows.

As explained above, we start with an associated flow rule. Though the system is not hyperbolic, its 'quasi-hyperbolic' nature suggests that numerical methods devised for hyperbolic systems may be adapted to generate solutions to initial-boundary-value problems. This is discussed in detail in §4.

3. Problem formulation

3.1. *Introduction*

In view of the structure of the basic equations, it is natural to formulate an initial-boundary-value problem, with initial conditions specified along a curve spanning the bunker, and boundary conditions specified along the walls. The experimental work reported in the literature provides valuable clues towards the specification of initial and boundary conditions. As discussed in §1, the following features may be noted: (i) In the bin section, the material descends in plug flow, with an approximately constant density. (ii) There is a transition region between the bin and the hopper

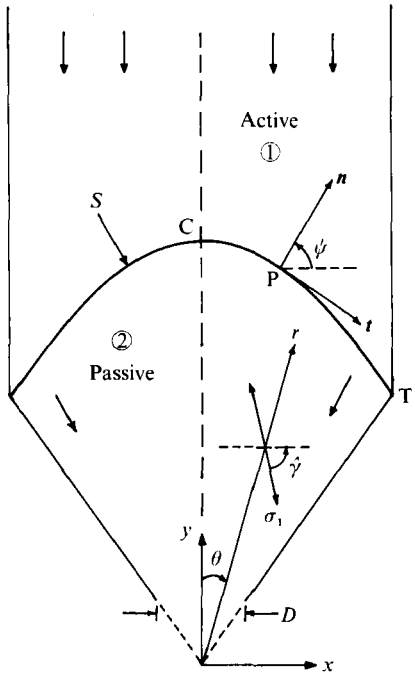

FIGURE 3. Shock separating active and passive regions.

sections, across which the density, velocity, and stresses change sharply. (iii) The state of stress is believed to be 'active' above the transition region and 'passive' below it. (iv) The normal stress on the bin walls tends to attain a constant value on moving downwards from the free surface. The data of Clague (quoted in Blight 1986) suggests that wall stresses in the bin section are largely unaffected by whether the material is flowing or not. However, for flat-bottomed bins, the data of Tüzün, Adams & Briscoe (1988) suggest that dynamic wall stresses exceed static values. These observations will now be used to formulate suitable initial and boundary conditions. It is convenient to use Cartesian coordinates (x, y) in the bin, and polar coordinates (r, θ) in the hopper, as indicated in figure 1.

3.2. *Boundary conditions*

As in earlier works (see for example Brennen & Pearce 1978), it will be assumed that the solution is symmetric about the centreline $\theta = 0$ (figure 1). Therefore, the normal component of velocity must vanish along the centreline, i.e.

$$v_x(x = 0, y) = 0 \quad \text{(bin)}; \quad v_\theta(r, \theta = 0) = 0 \quad \text{(hopper)}, \tag{37}$$

where v_x is the component of the velocity vector in the x-direction. Similarly, the shear stress must vanish, i.e.

$$\sigma_{xy}(x = 0, y) = 0 \quad \text{(bin)}, \tag{38}$$

$$\sigma_{r\theta}(r, \theta = 0) = 0 \quad \text{(hopper)}. \tag{39}$$

Here σ_{xy} is the relevant Cartesian component of the stress tensor. If $\hat{\gamma}$ is the orientation of the major principal stress axis relative to the horizontal direction (figure 3), then in terms of Sokolovskii variables

$$\sigma_{xx} = \sigma + \tau \cos 2\hat{\gamma}; \quad \sigma_{xy} = -\tau \sin 2\hat{\gamma}. \tag{40}$$

Using (22) and (40), it follows that (38) and (39) have two solutions each:

(i) $\hat{\gamma} = 0$ (which is called the passive state),

(ii) $\hat{\gamma} = \frac{1}{2}\pi$ (which is called the active state);

and (i) $\gamma = 0$ (passive state); (ii) $\gamma = \frac{1}{2}\pi$ (active state).

In view of the experimental observation (iii) in §3.1, we set

$$\hat{\gamma}(x = 0, y) = \tfrac{1}{2}\pi \quad \text{(bin)}; \quad \gamma(r, \theta = 0) = 0 \quad \text{(hopper)}. \tag{41}$$

The location of the exact point on the centreline where the switch in the orientation of the σ_1 axis occurs is discussed later.

Let us now consider the boundary conditions along the hopper wall. As the normal component of velocity must vanish along the wall, we have

$$v_x(x = L, y) = 0 \quad \text{(bin)}; \quad v_\theta(r, \theta = \theta_w) = 0 \quad \text{(hopper)}. \tag{42}$$

The other condition follows from the usual assumption (Brennen & Pearce 1978; Savage & Sayed 1979) that the ratio of the shear to normal stress is a constant along the wall. If T and N are the shear and normal stresses, respectively, exerted on the powder by the wall, (40) imply that on the bin wall

$$\frac{T}{N} = \frac{-\sigma_{xy}}{\sigma_{xx}} = \frac{\tau \sin 2\hat{\gamma}}{\sigma + \tau \cos 2\hat{\gamma}} = \tan \delta, \tag{43}$$

while (22) imply that on the hopper wall,

$$\frac{T}{N} = \frac{-\sigma_{r\theta}}{\sigma_{\theta\theta}} = \frac{\tau \sin 2\gamma}{\sigma + \tau \cos 2\gamma} = \tan \delta, \tag{44}$$

where δ is a material constant called the angle of wall friction.

The value of δ is usually determined from experiments conducted in a Jenike shear cell (Jenike 1964*a*; Brown & Richards 1970, p. 113). Though the state of the material in the shear cell is not well defined, previous investigators have used this value of δ in the boundary conditions (43) and (44). It was found that the dependence of the predicted discharge rate on the wall roughness was qualitatively similar to that observed, at least for steep hoppers. However, most of the earlier analyses were confined to incompressible flow. It is not clear whether (44) can be used intact for compressible flow. The work of Tüzün *et al.* (1988) sheds some light on this point. They have attempted to predict the angle of wall friction δ in a bin, from single-particle frictional properties and a geometric description of the particle assembly near the wall. For particles with a relatively rough surface, such as mustard seeds, δ is independent of the bed height and the bulk density. For particles with smoother surfaces, such as glass beads, δ depends on the bulk density. To simplify the analysis, it will be assumed here that δ is a constant.

Using the yield condition (17), (43) and (44) reduce to

$$\frac{\sin \bar{\phi} \sin 2\gamma_w}{1 + \sin \bar{\phi} \cos 2\gamma_w} = \tan \delta; \quad \sin \bar{\phi} = \frac{h(\alpha)}{\alpha}, \tag{45}$$

where

$$\gamma_w \equiv \begin{cases} \hat{\gamma}(x = L, y) & \text{(bin)} \\ \gamma(r, \theta = \theta_w) & \text{(hopper)}. \end{cases} \tag{46}$$

Equation (45) becomes identical to the incompressible result when $\bar{\phi}$ is replaced by ϕ. It follows that (45) has two roots (see for example Horne & Nedderman 1978; Kaza & Jackson 1982*a*). These are

$$\gamma_w \equiv \gamma_a = \tfrac{1}{2}\pi + \tfrac{1}{2}\delta - \tfrac{1}{2}\sin^{-1}\left[\frac{\sin\delta}{\sin\bar{\phi}}\right]; \quad \gamma_w \equiv \gamma_p = \tfrac{1}{2}\delta + \tfrac{1}{2}\sin^{-1}\left[\frac{\sin\delta}{\sin\bar{\phi}}\right], \quad (47a, b)$$

where the subscripts 'a' and 'p' denote active and passive states, respectively. For the special case of smooth walls, $\delta = 0$, and (47) reduce to the corresponding active and passive values at the centreline, namely $\gamma_a = \frac{1}{2}\pi$ and $\gamma_p = 0$. Consistent with the choice implied by (41), we set

$$\hat{\gamma}(x = L, y) = \gamma_a \quad \text{(bin)}; \quad \gamma(r, \theta = \theta_w) = \gamma_p \quad \text{(hopper)}, \tag{48}$$

where γ_a and γ_p are defined by (47).

3.3. *Initial conditions*

In view of the experimental observation (i) in §3.1, we might choose the initial curve to be a horizontal line, located some distance above the bin–hopper transition, and specify the following initial conditions:

$$\rho^* = \text{constant} \equiv \rho_b^*; \quad v_x^* \equiv \frac{v_x}{(gL)^{\frac{1}{2}}} = 0; \quad v_y^* \equiv \frac{v_y}{(gL)^{\frac{1}{2}}} = \text{constant} \equiv -u. \tag{49}$$

Values of σ^* and $\hat{\gamma}$ must also be specified along the initial curve. To do this, it may be noted that the mass balance, the coaxiality condition, and the flow rule are identically satisfied by a solution of the form (49), and the momentum balances admit an exact solution of the form

$$\sigma^* = \sigma^*(x/L); \quad \hat{\gamma} = \hat{\gamma}(x/L). \tag{50}$$

Here the functions $\sigma^*(x/L)$ and $\hat{\gamma}(x/L)$ can be determined by integrating ordinary differential equations, as discussed in Appendix A. Note that the stress field so obtained is independent of the magnitude of the plug flow velocity u, in accord with experimental observations.

In the static case, Horne & Nedderman (1978), Wilms & Schwedes (1985) and others have integrated the force balances in the bin, using the assumptions of incompressibility and the Mohr–Coulomb yield condition

$$\tau^* = \sigma^* \sin\phi. \tag{51}$$

Their computations have shown that the stress field (50) is approached asymptotically on moving downwards from the free surface of the fill. It seems reasonable to expect that this feature will be preserved when (51) is replaced by the yield condition (28).

3.4. *The transition region*

The above discussion suggests that (49) and (50) constitute a plausible set of initial conditions, which are compatible with the experimental observations (i), (iii) and (iv) in §3.1. It remains to account for observation (ii). This is a difficult problem, for which a satisfactory treatment is not available at present. Some attempts are indicated below.

Though the initial conditions (49) and (50) constitute a particular solution of the basic equations, this solution is not valid in the hopper section as it does not satisfy

the appropriate boundary conditions. The latter imply that the velocity and stress fields are discontinuous both at the bin–hopper transition, and at the point on the centreline, as yet undetermined, where the state of stress switches from active to passive. It seems unlikely that a solution can be found that is continuous in the interior of the region bounded by the centreline and the wall, and discontinuous only at the boundaries. Hence the possibility of a discontinuous solution must be considered.

In hyperbolic systems, discontinuous solutions are permissible, but only in regions where characteristics of the same family cross or overlap. The characteristics defined by (36*a*) are streamlines, and hence do not overlap, whereas those defined by (36*b*, *c*) may overlap. The slopes of the latter depend on γ and ν, and ν in turn is a function of $\alpha = \sigma/\sigma_c(\rho)$. Thus the slopes are not known *a priori*. However, prescription of α suffices to determine them, both at the centreline and the wall. With the yield locus used here, the values of α must lie in the interval $[0, \alpha_{\max}]$, where

$$\alpha_{\max} = \left[1 + \frac{1}{n \sin \phi}\right]^{n_1}.$$

For $\alpha > \alpha_{\max}$, there are no real characteristics, save the streamline. (In all the computations discussed here, α was found to be $< \alpha_{\max}$.) With this interval for α, the orientations of the characteristics may be plotted as a function of α.

For typical parameter values, it is found that at the centreline, the characteristics of one family overlap, while those of the other family form a fan. On the other hand, at the bin–hopper transition, the inverse situation prevails for most values of α. This is discussed in greater detail in Prakash (1989).

Given the complex behaviour exhibited by the characteristics, it is not clear how one should proceed. Therefore, it is helpful to first summarize earlier attempts. These may be divided into two groups: (*a*) where attention is confined to the stresses in the transition region, and (*b*) where only the kinematics of this region are considered. The above two groups are discussed in turn below.

Let us first consider the stress aspects of the transition region. All the work described here is based on incompressible powders obeying the Mohr–Coulomb yield condition. With these assumptions, the force balances constitute a hyperbolic system whose characteristics are inclined at angles $\pm(\frac{1}{4}\pi - \frac{1}{2}\phi)$ relative to the σ_1 axis. In the 'differential slice' approach of Walker (1966) and Walters (1973), the transition region was idealized as a horizontal line, which separated an active region above from a passive region below. The requirement of continuity of the mean normal (vertical) stress sufficed to construct the stress field below the transition. In a more rigorous analysis, Jenike & Johanson (1968) made use of the fact that one family of characteristics forms a fan at the bin–hopper transition. Using this feature, the value of N_h/N_b could be estimated, where N_h and N_b denote the normal stresses exerted on the hopper and bin walls, respectively, at the transition point. Subsequently, Bransby & Blair-Fish (1974) and Horne & Nedderman (1978) noted that the other family of characteristics overlap at this point. Hence an alternative solution involving a discontinuity or shock issuing from the transition point into the bunker, is also possible. Bransby & Blair-Fish (1974) computed N_h/N_b for both types of solutions, but did not determine the shape of the shock at interior points. In fact, as noted by Horne & Nedderman (1978), it is impossible to build the shock into the bunker without prescribing additional information. Thus Savage & Yong (1970) assumed the shock to be a circular arc, and used jump balances or discontinuity relations (Courant & Hilbert 1962, p. 489; Sokolovskii 1965, p. 100; Slattery 1981,

p. 41) to obtain the stress field on the downstream side. Similarly, Enstad (1975) assumed a form for the γ-field below the shock, and used the jump balances to determine the shape of the shock.

On the other hand, Horne & Nedderman (1978) used the fan-type solution near the bin–hopper transition, but found that this would destroy the symmetry of the solution in the region where the fan intersected the centreline. Symmetry was preserved by introducing a discontinuity at the intersection of the upper boundary of the fan and the centreline. This could be continued downwards without making any additional assumptions, enabling the stress field in the hopper to be found. The analysis of Horne & Nedderman (1978) is perhaps the most satisfactory treatment of the stresses in the transition region. However, the peak in the normal stress on the wall does not occur at the bin–hopper transition, as has been observed (Rao & Venkateswarlu 1974; Clague (quoted in Blight 1986)), but at some distance below it.

Let us now consider the kinematic aspects. If the stress field is assumed to be known, the coaxiality condition (26) and the flow rule (27) form a hyperbolic system whose characteristics are inclined at $\pm(\frac{1}{4}\pi - \frac{1}{2}\nu)$ relative to the σ_1 axis. Further, if the angle of dilation ν is taken as a constant, the equations are linear; hence velocity discontinuities can occur only across the characteristics (Shield 1953; Courant & Hilbert 1962, p. 488). The identification of velocity discontinuities with characteristics is central to the work of Drescher, Cousens & Bransby (1978) and Michalowski (1987). For instance, Michalowski assumes that the velocity field changes discontinuously across a characteristic issuing from the bin–hopper transition, from plug flow in the bin to one whose velocity vector at the transition is parallel to the hopper wall. Since the slope of the characteristics depends on γ, he also prescribes a form for the γ-field.

It is evident from the above discussion that there has been no attempt to treat the stress and the kinematic aspects of the transition region simultaneously. At the moment, it is not clear how the approach of Horne & Nedderman (1978) should be extended to incorporate variations in density and velocity. Another approach has been suggested by R. Jackson (1987, private communication) and by one of the referees. This requires a jump in stress across a 'switch surface', and a jump in velocity (and hence in density) across a velocity characteristic. Unfortunately, with the present constitutive equations, a jump in density will in general induce jumps in both the state of stress and the angle of dilation ν. Thus the jump in stress is not confined to the switch surface alone; further, the slope of the velocity characteristic is not uniquely defined, since it depends on ν. Hence this approach will not be pursued, even though it is intuitively more appealing than the one used here. Perhaps the constitutive equations have to be modified before it can be implemented satisfactorily. Here we adopt the simpler alternative of permitting all the field variables to change discontinuously across a shock or discontinuity curve, the stress field from active to passive, and the velocity field from vertical to one compatible with the boundary conditions in the hopper. Thus the present work represents an extension of the work of Savage & Yong (1970).

As in their work, jump conditions must hold across the shock (Courant & Hilbert 1962, p. 489; Slattery 1981, p. 41). In the literature, jump conditions have been derived for two cases: (i) linear hyperbolic systems, and (ii) quasi-linear hyperbolic systems of conservation laws, which are of the form

$$\frac{\partial \boldsymbol{a}_1}{\partial x} + \frac{\partial \boldsymbol{a}_2}{\partial y} + \boldsymbol{a}_3 = 0. \tag{52}$$

Here the $\boldsymbol{a}_i$ are vector functions of x, y, and the field variables. The mass and momentum balances (equations (23)–(25)) may be expressed in the form (52), and hence there are three jump conditions corresponding to them. On the other hand, the coaxiality condition (26) and the flow rule (27) are not in conservation law form; neither are they linear, since γ and ν are not known *a priori*.

The difficulty is overcome by specifying additional conditions on the downstream side of the shock. This *ad hoc* procedure has been adopted for want of a better alternative; it is hoped that a more satisfactory treatment will emerge eventually.

It has been tacitly assumed that the basic equations behave like a hyperbolic system, but this is not strictly true. Their quasi-hyperbolic nature provides some justification, albeit weak. In addition, it will be seen later that they have to be modified slightly in order to alleviate computational difficulties, and the modified equations are hyperbolic.

The stage has now been set for the construction of the shock, details of which are discussed below. Since the values of the field variables on its downstream side will be used as initial conditions for the hopper problem, the shock will be referred to as the initial curve.

3.5. *The initial curve*

Referring to figure 3, let n be the unit normal to the shock S, at a point P. For a stationary shock, the jump mass and momentum balances take the form (Slattery 1981, pp. 25, 41)

$$J[\rho v_n] = 0; \quad J[\rho v_n \boldsymbol{v} + \boldsymbol{\sigma}\cdot\boldsymbol{n}] = 0, \tag{53a, b}$$

where $J[\Phi] \equiv \Phi_{(2)} - \Phi_{(1)}$ is the jump in any quantity Φ on crossing S, $v_n \equiv \boldsymbol{n}\cdot\boldsymbol{v}$ is the component of velocity normal to S, and all quantities are evaluated at the point P. Henceforth subscripts 1 and 2 will denote conditions on the upstream and downstream sides of S, respectively. It is convenient to express the stress tensor $\boldsymbol{\sigma}$ in terms of Sokolovskii variables σ, τ and $\hat{\gamma}$ (figure 3). Resolving (53*b*) into components normal and tangential to the shock, (53) may be written in dimensionless form as

$$\rho^*_{(1)} v^*_{n(1)} - \rho^*_{(2)} v^*_{n(2)} = 0, \tag{54}$$

$$\rho^*_{(2)}[v^*_{n(2)}]^2 - \rho^*_{(1)}[v^*_{n(1)}]^2 + [\sigma^*_{(2)} - \sigma^*_{(1)}] + [\tau^*_{(2)} \cos(2\hat{\gamma}_{(2)} + 2\psi) - \tau^*_{(1)} \cos(2\hat{\gamma}_{(1)} + 2\psi)] = 0, \tag{55}$$

$$\text{and} \quad [\rho^*_{(2)} v^*_{n(2)} v^*_{t(2)} - \rho^*_{(1)} v^*_{n(1)} v^*_{t(1)}] + [\tau^*_{(2)} \sin(2\hat{\gamma}_{(2)} + 2\psi) - \tau^*_{(1)} \sin(2\hat{\gamma}_{(1)} + 2\psi)] = 0, \tag{56}$$

where $v^*_n \equiv v_n/(gL)^{\frac{1}{2}}$; $v^*_t \equiv v_t/(gL)^{\frac{1}{2}}$ and $v_t = \boldsymbol{t}\cdot\boldsymbol{v}$ is the component of velocity tangential to S (figure 3). The angle ψ, which gives the orientation of the shock, is defined as indicated in figure 3.

The upstream variables $v^*_{n(1)}$ etc. are assumed to be given by the initial conditions (49) and (50), i.e. plug flow with an active stress field. In (49), the value of the constant u is unknown *a priori*; it will be determined iteratively as described later.

Equations (54)–(56) contain the seven unknowns $\rho^*_{(2)}$, $v^*_{n(2)}$, $v^*_{t(2)}$, $\sigma^*_{(2)}$, $\tau^*_{(2)}$, $\hat{\gamma}_{(2)}$, and ψ, but $\tau^*_{(2)}$ is related to $\sigma^*_{(2)}$ through the yield condition (28). Thus three additional equations are needed to close the set. Here, these are obtained by making the following plausible physical assumptions:

(i) On the downstream side of S, the velocity vector is directed radially towards the apparent vertex of the hopper section. This ensures that the velocity field is compatible with the boundary conditions (37) and (42). By way of additional justification, we turn to the experimental observations of Lee *et al.* (1974), Bransby

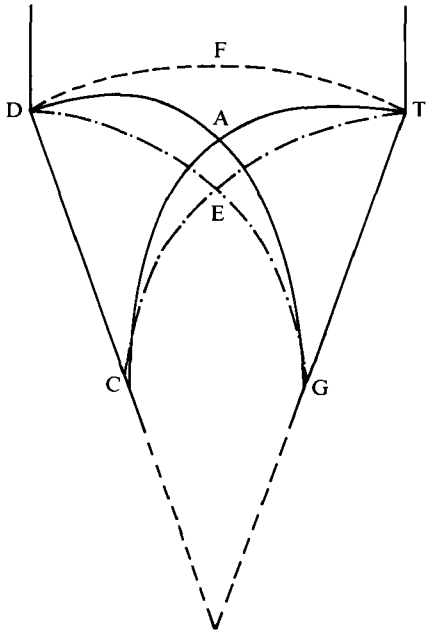

FIGURE 4. Comparison of the shock profile predicted by the present theory (– – –) with the rupture layer observed by Michalowski (1987) (——) and the prediction of Michalowski (1987) (— · —). The parameters $\phi = 32°$, $\delta_b = \delta_h = 11°$, $\theta_w = 20°$, $\beta^* = 35$, and $\rho_b^* = 0.78$ are reported in Michalowski (1987). Here, the remaining parameters are assumed to be: $\Gamma = 1.34$, $\lambda = 0.02$, $n = 1.05$, and $u = 0.0125$.

& Blair-Fish (1975) and Michalowski (1987). With reference to figure 4, these suggest that the material moves vertically in the bin section, parallel to the hopper wall in the triangular region bounded by the rupture layers AD and AC and the wall DC, and radially below AC. Michalowski (1987) concurs with these findings, but his data for $\theta_w = 20°$ (figure 10 of his paper) can be approximated well by the assumption of radial flow, even in the region ADC. Thus this assumption may be reasonable for small values of θ_w; for larger values, a realistic model must allow for two or more rupture layers, so that a region of flow parallel to the walls can be accommodated. Here the problem has been simplified by ignoring this region, and considering only a single rupture layer or shock.

(ii) The next assumption is that the material on the downstream side is at a critical state, i.e.

$$\tau_{(2)}^* = \sigma_{(2)}^* \sin\phi; \quad \sigma_{(2)}^* = \sigma_{c(2)}^* = \beta^* \exp\left[\frac{\Gamma\rho_{(2)}^* - 1}{\lambda\rho_{(2)}^*}\right]. \tag{57}$$

With the parameter values used, the material on the upstream side is found to be 'denser than critical', in the terminology of Schofield & Wroth (1968, p. 21). Hence it dilates across the shock to attain the critical state (57). Such behaviour is evident in the radiographs of Lee *et al.* (1974), Bransby & Blair-Fish (1975), and Michalowski (1987). However, it is not clear from the literature that downstream conditions necessarily correspond to a critical state.

It may be noted that assumptions (i) and (ii) have been used earlier by Drescher *et al.* (1978), in their analysis of the kinematics of rupture surfaces in hoppers. Using the above two assumptions together with the jump balances (54)–(56) and the stress

boundary conditions (41) and (48), the values of all the downstream variables can be found at both the wall and the centreline, as discussed shortly.

(iii) Elsewhere an additional condition is needed; here we use the *ad hoc* assumption that $\rho^*_{(2)}$ is a quadratic function of θ, which takes on the known values at $\theta = 0$ and θ_w. The basis for this choice is that symmetric solutions of the basic equations (23)–(27) can be ensured by requiring ρ^*, v^*_r and σ^* to be even functions of θ, and v^*_θ and γ to be odd functions of θ. The proposed functional form is merely a simple example of an even function. Clearly, other choices are possible. Indeed, this non-uniqueness is a shortcoming of the present theory.

Let u and $u_{(2)}$ denote the magnitudes of the vertical velocity in the bin section and the radial velocity in the hopper section, respectively. Then the normal and tangential components of velocity are given by

$$v^*_{n(1)} = -u\sin\psi; \quad v^*_{t(1)} = u\cos\psi \tag{58}$$

and

$$v^*_{n(2)} = -u_{(2)}\sin(\theta+\psi); \quad v^*_{t(2)} = u_{(2)}\cos(\theta+\psi). \tag{59}$$

Using the jump mass balance (54), $u_{(2)}$ may be eliminated to get

$$u_{(2)} = \frac{\rho^*_{(1)}\, u\sin\psi}{\rho^*_{(2)}\sin(\theta+\psi)}. \tag{60}$$

With the help of (58)–(60), the jump momentum balances may be rewritten as

$$\rho^*_{(1)}\, u^2\sin^2\psi\left[\frac{\rho^*_{(1)}}{\rho^*_{(2)}}-1\right]+[\sigma^*_{(2)}-\sigma^*_{(1)}]+[\tau^*_{(2)}\cos(2\hat{\gamma}_{(2)}+2\psi)-\tau^*_{(1)}\cos(2\hat{\gamma}_{(1)}+2\psi)] = 0 \tag{61}$$

and

$$-\rho^*_{(1)}\, u^2\sin^2\psi\left[\frac{\rho^*_{(1)}}{\rho^*_{(2)}}\cot(\theta+\psi)-\cot\psi\right]+[\tau^*_{(2)}\sin(2\hat{\gamma}_{(2)}+2\psi)-\tau^*_{(1)}\sin(2\hat{\gamma}_{(1)}+2\psi)] = 0. \tag{62}$$

All the downstream variables at the wall and centreline are determined as follows. At the centreline, $\theta = 0$, $\hat{\gamma}_{(1)} = \frac{1}{2}\pi$ and $\hat{\gamma}_{(2)} = 0$. Hence (62) reduces to

$$\left[-\tfrac{1}{2}\rho^*_{(1)}\, u^2\left(\frac{\rho^*_{(1)}}{\rho^*_{(2)}}-1\right)+\tau^*_{(2)}+\tau^*_{(1)}\right]\sin 2\psi = 0. \tag{63}$$

Since the expression in square brackets does not vanish in general, (63) implies that

$$\psi = 0; \quad \text{or} \quad \psi = \tfrac{1}{2}\pi. \tag{64}$$

The root $\psi = 0$ corresponds to a shock which is vertical at the centreline. In this case, the value of $u_{(2)}(\theta = 0)$ is arbitrary, since the jump mass balance is identically satisfied at $\theta = 0$. Of course, $\psi \neq 0$ for $\theta > 0$, and $u_{(2)}(\theta = 0)$ could possibly be set equal to $\lim_{\theta\to 0}[u_{(2)}(\theta)]$. Here we choose the other root, $\psi = \frac{1}{2}\pi$, which corresponds to a shock which is horizontal at the centreline. This choice permits $u_{(2)}(\theta)$ to be determined for all values of $\theta, 0 \leqslant \theta \leqslant \theta_w$. On setting $\psi = \frac{1}{2}\pi$ in (61) and using (41) and (57), a nonlinear equation results for $\rho_0 \equiv \rho^*_{(2)}(\theta = 0)$, which is solved iteratively using the Newton–Raphson method. At the wall, $\theta = \theta_w$, $\hat{\gamma}_{(1)} = \gamma_a$, and $\hat{\gamma}_{(2)} = \gamma_p + \theta_w$. Hence (61) and (62) are two nonlinear equations for $\rho_w \equiv \rho^*_{(2)}(\theta = \theta_w)$ and $\psi_w \equiv \psi(\theta = \theta_w)$, which are also solved iteratively using the Newton–Raphson method.

At interior points $0 < \theta < \theta_w$, $\rho^*_{(2)}$ is assumed to be given by

$$\rho^*_{(2)} = \rho_0 + [\rho_w - \rho_0]\left(\frac{\theta}{\theta_w}\right)^2 \tag{65}$$

as indicated earlier. On substituting for $\rho^*_{(2)}$ from (65) into (61) and (62), these reduce to a pair of nonlinear equations, which are solved iteratively for $\hat{\gamma}_{(2)}$ and ψ. Finally, the shape of the shock is found by integrating the equation

$$\frac{1}{r^*}\frac{\mathrm{d}r^*}{\mathrm{d}\theta} = -\cot(\theta + \psi) \tag{66}$$

subject to the initial condition $r^*(\theta = \theta_w) \equiv r^*_w = 1/\sin\theta_w$. At every stage of the integration, the value of ψ is taken from the solution of (61) and (62).

This completes the specification of the initial curve, and the initial data along it. As mentioned earlier, the velocity data depend on u, the magnitude of the plug flow velocity in the bin section. To determine u, an additional 'exit' condition must be specified. This is discussed below.

3.6. *The exit condition*

Following Savage (1965) and Davidson & Nedderman (1973), it has been common practice (Brennen & Pearce 1978; Savage & Sayed 1979; Kaza & Jackson 1982*a*; Meric & Tabarrok 1982) to assume that the material in the hopper is bounded from below by a traction-free surface spanning the exit slot. Along this surface, the shear and normal stresses vanish; below it, the material is assumed to fall freely under gravity, with zero frictional stresses. For cohesionless materials, the mean stress σ^* vanishes along this surface. In particular, we require

$$\sigma^*(r^* = r^*_e, \theta = \theta_w) = 0; \quad r^*_e = \frac{r_e}{L} = \frac{D}{2L\sin\theta_w}. \tag{67}$$

Here r_e is the radial coordinate corresponding to the hopper exit (figure 1), and D is the width of the exit slot (figure 3).

It appears that (67) suffices to determine u – guessing a value for u, and integrating the basic equations down the hopper section, it may be checked whether (67) holds to within a prescribed accuracy. If not, the procedure may be repeated with another value of u. However, there are two obstacles to this approach, one related to the unattainability of the exit condition (67), and the other to the unrealistic consequences of this condition. These are discussed below, followed by an alternative proposal for the exit condition.

(*a*) The momentum balances (24) and (25) are singular on the traction-free surface $\sigma^* = 0$, since σ^* multiplies all the derivatives of γ. Hence it is extremely difficult to approach this surface from above, at least with the present numerical method. This problem was encountered earlier by Savage & Yong (1970) and Kaza & Jackson (1982*a*) in their incompressible analyses of hopper statics and hopper flow, respectively.

(*b*) In the incompressible case, it has been shown (Kaza & Jackson 1984) that material on the downstream side of the traction-free compacts if

$$\frac{\partial \sigma_{ww}}{\partial w} > 0$$

where w is the distance measured along the upward normal to this surface. The existing approximate solutions (see, for example, Savage 1965; Brennen & Pearce 1978; Savage & Sayed 1979) predict a traction-free surface which lies above the plane of the exit slot, and along which the above inequality holds. Thus particles below this surface tend to press against each other, leading to a buildup of frictional stresses. This is inconsistent with the assumption of free fall with zero frictional stresses, and hence the exit condition (67) must be abandoned. This conclusion is reinforced by the density measurements of Bosley *et al.* (1969), Van Zuilichem *et al.* (1974), and Fickie *et al.* (1989), which show a strong dilation, rather than compaction, near the exit slot. Indeed Fickie *et al.* (1989) have suggested that there is no traction-free surface of the type discussed above. If so, the constitutive equations may have to be modified suitably, such that at the exit plane, $\sigma^* > 0$ except possibly at the edge of the slot, i.e. at $(r^* = r_e^*, \theta = \theta_w)$. As the form of the modified constitutive equations is not clear at present, the existing ones will be retained, and the exit condition will be altered instead.

So far, the discussion has been confined to the case of incompressible flow in the hopper section. It was conjectured (Kaza & Jackson 1984) that if this assumption were relaxed, dilation of the material might be strong enough to prevent compaction on the downstream side of the traction-free surface. In the present work, this could not be checked because of numerical problems encountered in approaching $\sigma^* = 0$. However, in the special case of compressible flow through a hopper with smooth walls and radially directed gravity, there is no such singularity in the basic equations. Hence they can be integrated all the way to the traction-free surface, as discussed elsewhere (Prakash & Rao 1988). Using the results presented there for three materials, it can be shown that the exit condition is still inconsistent, in spite of dilation above the traction-free surface.

In view of the problems associated with a traction-free surface, the exit condition (67) will be abandoned in favour of an alternative one proposed by Kaza & Jackson (1982*b*). This assumes that the hopper terminates at a 'surface of free fall', or 'exit shock', which spans the exit slot. The field variables change discontinuously across it, attaining a state of vertical velocity and zero frictional stress ($\sigma^* = 0$) on the downstream side. This ensures that the material dilates as it falls vertically under the influence of gravity, while σ^* vanishes throughout. Thus the inconsistency referred to earlier is avoided. However, a new problem arises, as explained below.

It can be shown (Kaza & Jackson 1982*b*) that the shape of the exit shock is determined by integrating the equation

$$\frac{1}{r^*}\frac{\mathrm{d}r^*}{\mathrm{d}\theta} \equiv \tan\psi' = \frac{[\sigma^*\sin\theta - \tau^*\sin(2\gamma+\theta)] + \rho^* v_r^*[v_r^*\sin\theta + v_\theta^*\cos\theta]}{[\sigma^*\cos\theta + \tau^*\cos(2\gamma+\theta)] + \rho^* v_\theta^*[v_r^*\sin\theta + v_\theta^*\cos\theta]} \tag{68}$$

subject to the initial condition $r^*(\theta_w) = r_e^*$. Here ψ' is the angle measured anticlockwise from the radial direction to the upward normal to the shock.

For any specified values of the exit radius r_e^* and the bin velocity u, the exit shock can be constructed using (68). While r_e^* is known *a priori*, u is not; hence the exit condition does not determine u uniquely. However, an upper bound on u may be constructed by appealing to the hyperbolic nature of the basic equations, as indicated below.

The slope of the shock depends on the values of the upstream variables, which are known only within the domain of determinacy ABC of the exit slot AB (figure 5). At the point B, if the shock lies outside ABC, as in figure 5, it cannot be continued towards the centreline. It can be shown that this first occurs when u exceeds a critical

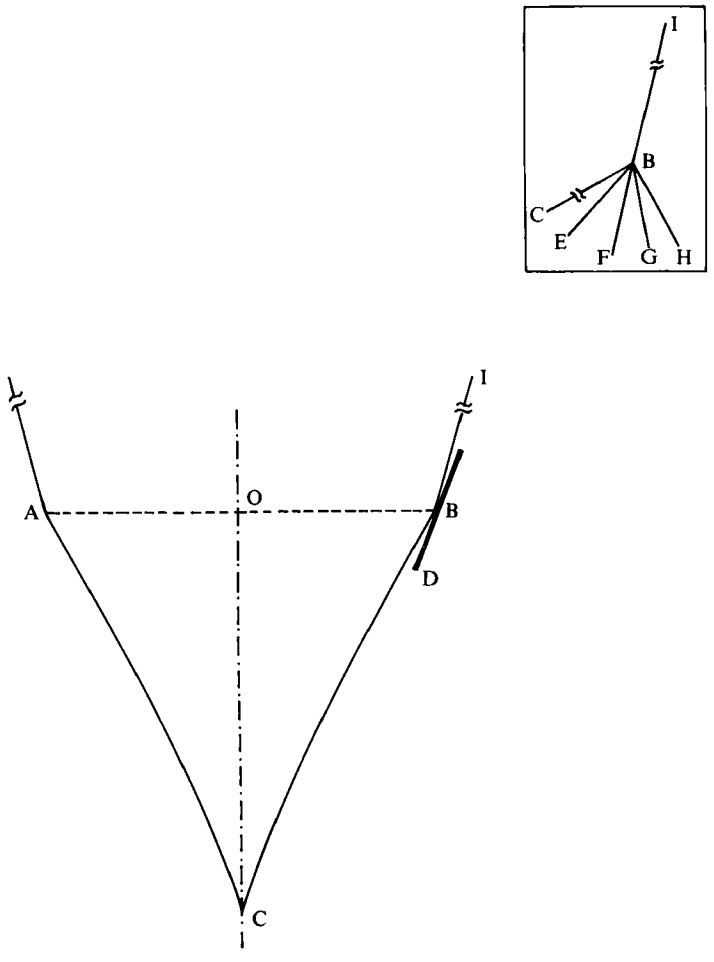

FIGURE 5. Domain of determinacy of exit slot: AB, exit slot; AC, BC, 'outermost' characteristics at C; BD, tangent to the shock at B; BI, hopper wall. Inset: typical characteristics BC, BE, BF, BG, and BH corresponding to the roots ψ_4, ψ_2, ψ_1, ψ_3, and ψ_5, respectively of (83).

value u_c; with $u = u_c$, the exit shock is tangential to the characteristic BC at the point B. In all the cases investigated here, this suffices to ensure that the shock lies within ABC (see, for example, figure 20). Thus the shock can be constructed for any value of $u \leqslant u_c$, and u_c is an upper bound on the discharge rate for all solutions satisfying the exit condition at $r^* = r_e^*$.

4. Solution procedure

The procedure for numerical integration of the basic equations (32) will now be described. As the initial curve defined by (66) is not a circular arc in general, it is convenient to use new coordinates (t, η), defined by

$$t = \frac{\ln[1-\xi(r^*,\theta)]}{\ln[1-\xi_e]}; \quad \eta = \frac{\theta}{\theta_w}, \tag{69}$$

where $\xi_e \equiv \xi(r_e^*, \theta_w)$. The function $\xi(r^*, \theta)$ is chosen so that $\xi = 0$ coincides with the

initial curve (66) and $\xi = 1$ corresponds to $r^* = 0$. The specific form used for $\xi(r^*, \theta)$ is given in §5.1.

Computations were originally performed with ξ and η as the independent variables. While using a difference scheme and marching downwards from the initial curve, it was found that the step size $\Delta\xi$ had to be decreased as r^* decreased, in order to ensure convergence. On the other hand, a constant value of Δt sufficed when t and η were used as the independent variables.

Equations (32) may be regarded as comprising two sets of hyperbolic systems, as noted in §2.5. Considering the velocity equations (23), (26) and (27) first, there are three characteristics $C_i, i = 1, 3$, whose slopes ψ_i are given by (36). The characteristic curves may be represented in parametric form by

$$\left(\frac{\mathrm{d}t}{\mathrm{d}s}\right)_i = \frac{-1}{(1-\xi)\ln[1-\xi_e]}\left\{\frac{\partial\xi}{\partial r^*} + \frac{\cot\psi_i}{r^*}\frac{\partial\xi}{\partial\theta}\right\},$$
$$\left(\frac{\mathrm{d}\eta}{\mathrm{d}s}\right)_i = \frac{\cot\psi_i}{r^*\theta_w}; \quad i = 1, 3. \tag{70}$$

Along these curves, the compatibility conditions, or equations in characteristic normal form, may be found using standard techniques (Courant & Hilbert 1962, pp. 424, 426; Prasad & Ravindran 1985, pp. 151, 153). They take the form

(i) along C_1

$$v_r^*\frac{\mathrm{D}_1\rho^*}{\mathrm{D}s} - \left[\frac{\rho^*\sin\nu\sin 2\psi_1}{\cos(2\gamma+2\psi_1)-\sin\nu}\right]\frac{\mathrm{D}_1 v_\theta^*}{\mathrm{D}s} + \left[\frac{\rho^*\sin\nu(\cos 2\psi_1 - 1)}{\cos(2\gamma+2\psi_1)-\sin\nu}\right]\frac{\mathrm{D}_1 v_r^*}{\mathrm{D}s}$$
$$= \left[\frac{\rho^*\sin\nu[v_r^*(\cos 2\psi_1+1) - v_\theta^*\sin 2\psi_1]}{r^*[\cos(2\gamma+2\psi_1)-\sin\nu]}\right]; \tag{71}$$

(ii) along C_2, C_3

$$\sin 2\psi_i\frac{\mathrm{D}_i v_\theta^*}{\mathrm{D}s} + 2\sin^2\psi_i\frac{\mathrm{D}_i v_r^*}{\mathrm{D}s} = \left[\frac{v_\theta^*\sin 2\psi_i - 2v_r^*\cos^2\psi_i}{r^*}\right]; \quad i = 2, 3, \tag{72}$$

where

$$\frac{\mathrm{D}_i}{\mathrm{D}s} \equiv \left(\frac{\mathrm{d}t}{\mathrm{d}s}\right)_i\frac{\partial}{\partial t} + \left(\frac{\mathrm{d}\eta}{\mathrm{d}s}\right)_i\frac{\partial}{\partial\eta} \tag{73}$$

is the directional derivative along the ith characteristic.

Turning to the stress equations (24) and (25), the characteristics are given by (36*b*, *c*), and the compatibility conditions take the form

$$[\cos(2\gamma+\psi_i) - \sin\nu\cos\psi_i]\frac{\mathrm{D}_i\sigma^*}{\mathrm{D}s} - [2\tau^*\sin\psi_i]\frac{\mathrm{D}_i\gamma}{\mathrm{D}s} + \left[\frac{\partial\tau^*}{\partial\rho^*}\frac{\sin^2\psi_i}{\cos\psi_i}\right]\frac{\mathrm{D}_i\rho^*}{\mathrm{D}s}$$
$$= \frac{\partial\tau^*}{\partial\rho^*}\frac{1}{r^*\cos\psi_i\ln(1-\xi_e)}\frac{\partial\rho^*}{\partial t} - \rho^* v_r^*\sin(2\gamma+\psi_i)\frac{\mathrm{D}_1 v_\theta^*}{\mathrm{D}s}$$
$$- \rho^* v_r^*\cos(2\gamma+\psi_i)\frac{\mathrm{D}_1 v_r^*}{\mathrm{D}s} - \frac{\rho^* v_\theta^*}{r^*}[v_r^*\sin(2\gamma+\psi_i) - v_\theta^*\cos(2\gamma+\psi_i)]$$
$$+ \frac{2\tau^*\cos\psi_i}{r^*} - \rho^*\cos(2\gamma+\psi_i+\theta); \quad i = 2, 3, \tag{74}$$

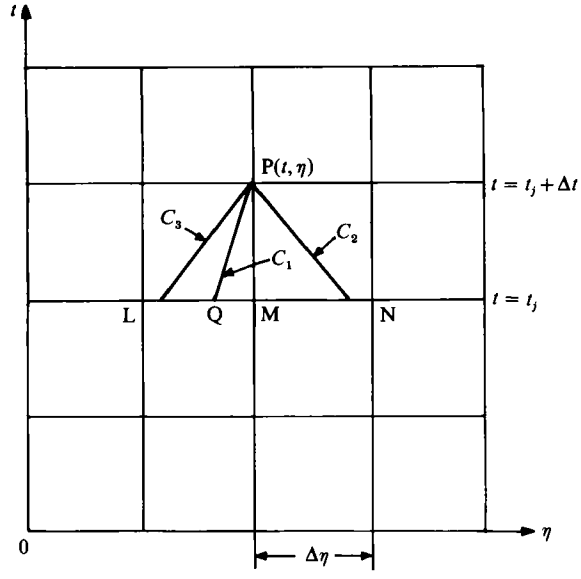

FIGURE 6. Grid for the inverse marching scheme.

along the C_2 and C_3 characteristics. Equations (74) are not true compatibility conditions, since they contain the derivatives $\partial/\partial t$ and $\mathrm{D}_1/\mathrm{D}s$ in addition to $\mathrm{D}_i/\mathrm{D}s$.

Having obtained the compatibility conditions, it remains to discuss the numerical method used to integrate them. This is based on an inverse marching scheme (Zucrow & Hoffman 1976, p. 336), wherein characteristics are drawn backwards from any point $\mathrm{P}(t, \eta)$ at which the solution is desired, to the previous 'time' level $(t-\Delta t)$ where the solution is known (figure 6). Along the characteristics, which are approximated by straight line segments, the compatibility conditions are integrated using a modified Euler predictor-corrector method. The reader is referred to Zucrow & Hoffman (1976, p. 341) for a detailed discussion of this method.

At the point of intersection of the initial curve with the wall, both initial and boundary conditions have been specified for v_θ and γ. This invariably leads to discontinuities in the values of their derivatives, which propagate into the hopper along characteristics issuing from this point or corner. The inverse marching scheme used here cannot follow these discontinuities as it does not track specific characteristics. In retrospect, it appears that a direct marching scheme (Zucrow & Hoffman 1976, p. 333), wherein some characteristics are tracked, may have been more suitable. However, this scheme also has two defects: (i) it leads to non-uniformly spaced grid points, which are more difficult to handle, and (ii) most of our results are based on a modified set of equations (§5.2.2), for which two characteristics issue from the corner into the hopper, and cannot be tracked simultaneously. It is hoped that this issue will receive greater attention in future.

The peculiar nature of our equations warrants a few additional remarks. Referring to figure 6, suppose the values of all the field variables are known along the line $t = t_j$, and it is desired to find the solution at the point P. The velocity compatibility conditions (71) and (72) are first integrated to obtain ρ^*, v_θ^* and v_r^* at P. Using the value of ρ^* at P, the stress compatibility conditions (74) are then integrated to obtain σ^* and γ at P, treating all the terms on the right-hand side as the non-homogeneous part of these equations. This implies that the derivatives $\mathrm{D}_1 v_\theta^*/\mathrm{D}s$, $\mathrm{D}_1 v_r^*/\mathrm{D}s$ and

$\partial\rho^*/\partial t$ are required at the points L, M and N in the predictor stage, and, in addition, at the point P in the corrector stage of the integration. Here, they are estimated by using a backward difference scheme. For example, at point P

$$\frac{\partial\rho^*}{\partial t} = \frac{\rho^*_{\mathrm{P}} - \rho^*_{\mathrm{M}}}{\Delta t}; \quad \frac{\mathrm{D}_1 v^*_r}{\mathrm{D}s} = \frac{v^*_{r\mathrm{P}} - v^*_{r\mathrm{Q}}}{\Delta s_1}; \quad \frac{\mathrm{D}_1 v^*_\theta}{\mathrm{D}s} = \frac{v^*_{\theta\mathrm{P}} - v^*_{\theta\mathrm{Q}}}{\Delta s_1}, \tag{75}$$

where Δs_1 is the distance PQ (figure 6). Clearly (75) cannot be used for points on the initial curve $t = 0$. Here it is assumed that

$$\left.\frac{\partial\rho^*}{\partial t}\right|_{t=0} = \left.\frac{\mathrm{D}_1 v^*_r}{\mathrm{D}s}\right|_{t=0} = \left.\frac{\mathrm{D}_1 v^*_\theta}{\mathrm{D}s}\right|_{t=0} = 0. \tag{76}$$

Since the initial conditions correspond to a critical state, and since the inertial terms are small in the vicinity of the initial curve, (76) is perhaps not unreasonable.

As a test case, the problem of compressible flow through a hopper with smooth walls and with radially directed gravity was examined. Here the basic equations reduce to ordinary differential equations, which were integrated using a semi-implicit Runge–Kutta method (Prakash & Rao 1988). The results were found to be in good agreement with those obtained using the present difference scheme.

5. Results

Results will now be presented from two angles: (i) to illustrate some aspects of the theory, and (ii) to compare with experiments. In case (i), computations are largely confined to Leighton Buzzard sand. Here the values of the material parameters in the yield locus (28) and the flow rule (31) are taken to be $\phi = 37°$, $\Gamma = 1.34$, $\lambda = 0.02$, and $n = 1.05$. The first three values are obtained from plots of τ *vs.* σ (at critical state), and σ_{c} *vs.* $1/\epsilon_{\mathrm{s}}(=\rho_{\mathrm{s}}/\rho)$ reported in Atkinson & Bransby (1978, p. 240), and n is estimated from the data of Airey, Budhu & Wood (1985) (see Appendix B). In case (ii), only the values of ϕ could be obtained from the literature, and, for want of data, the other parameters are assumed to have the same values as for Leighton Buzzard sand.

The results may be divided into four parts: (i) the entry shock or initial curve, (ii) a bunker with smooth hopper walls, (iii) a bunker with rough hopper walls, and (iv) the incompressible approximation. These are discussed in turn below.

Most of the computations are based on $\rho^*_{(1)} = 0.82$, which is in the range of poured bulk densities for sands (Atkinson & Bransby 1978, p. 10). The dependence of the values of the variables on the downstream side of the entry shock on upstream ones is examined below.

5.1. *The entry shock*

The full curves in figures 7 and 8 show profiles of $\rho^*_{(2)}$, $\sigma^*_{(2)}$, $\gamma_{(2)}$, and $v^*_{r(2)}$ for Leighton Buzzard sand, with $\beta^* = 5.25$, $u = 0.0125$, $\delta_{\mathrm{b}} = 16°$, $\delta_{\mathrm{h}} = 16°$ and $\theta_{\mathrm{w}} = 10°$. The value of β^* corresponds to a bin width of about 2 m, and u has been chosen so that the ratio of bin width to exit slot width is about 30–40. (A large value of this ratio facilitates the search for asymptotic stress and density fields, as discussed later.) The quantities δ_{b} and δ_{h} represent the angle of wall friction between the material and the bin wall, and that between the material and the hopper wall, respectively. For example, the angle of wall friction between sand and a lucite wall is 15° (Nguyen *et al.* 1980).

The profile of $\sigma^*_{(2)}$, obtained from (57) is similar in shape to that of $\rho^*_{(2)}$ (figure 7)

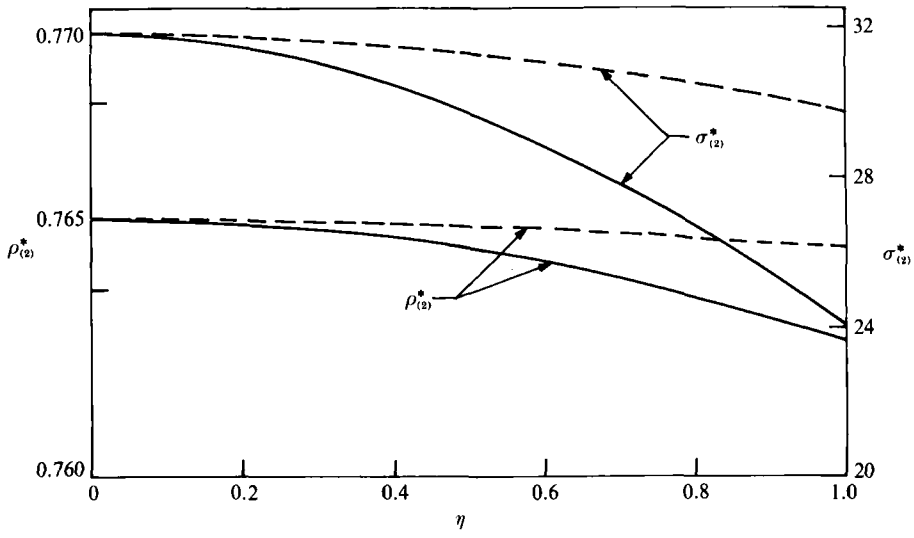

FIGURE 7. Stress and density profiles on the downstream side of the entry shock: ---, smooth-walled hopper with $\delta_h = 0°$; ——, rough-walled hopper with $\delta_h = 16°$. Other parameter values are: $\Gamma = 1.34$, $\lambda = 0.02$, $n = 1.05$, $\beta^* = 5.25$, $\rho_b^* = 0.82$, $u = 0.0125$, $\phi = 37°$, $\delta_b = 16°$ and $\theta_w = 10°$.

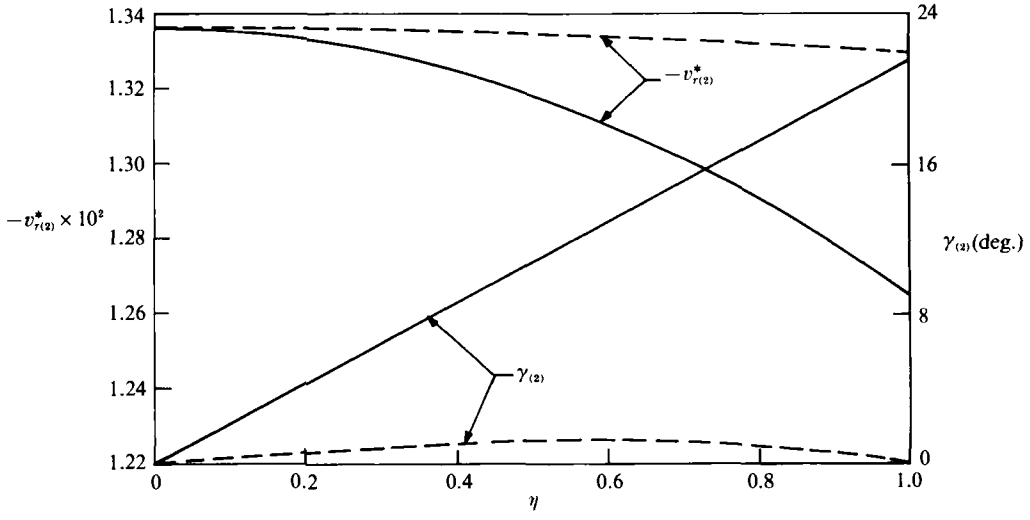

FIGURE 8. Radial velocity and γ-profiles on the downstream side of the entry shock: ---, smooth-walled hopper with $\delta_h = 0°$; ——, rough-walled hopper with $\delta_h = 16°$. Other parameters are as in figure 7.

because the range of densities is small. The profile of $\gamma_{(2)}$ is virtually linear (figure 8); this is found to be true for other parameter values also, provided that δ_h is not too small. It is seen that the magnitude of $v^*_{r(2)}$ is greater at the centreline than at the wall, as expected on account of wall roughness.

The circles in figure 9 show the entry shock obtained by numerical integration of (66), while the full curve is a parabolic fit, given by

$$r^* = a\left\{1 + m\left[\frac{\theta}{\theta_w}\right]^2\right\}. \tag{77}$$

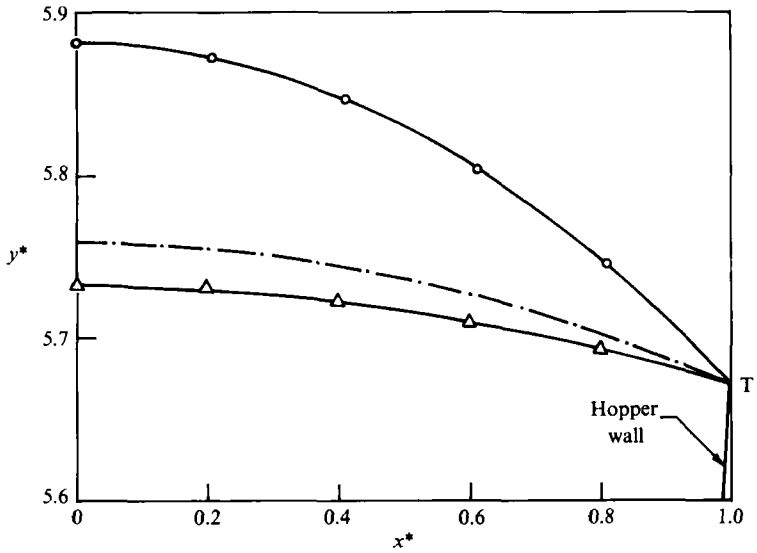

FIGURE 9. Shock profiles obtained by numerical integration of (66): △, smooth-walled hopper with $\delta_h = 0°$; ○, rough-walled hopper with $\delta_h = 16°$. Other parameters are as in figure 7. The full curves are least-square fits, and the dot-dashed curve is a circular arc at the bin–hopper transition T.

Here
$$m \equiv \left(\frac{r_w^*}{a}\right) - 1\,; \quad r_w^* = \frac{1}{\sin\theta_w} \tag{78}$$

is chosen to ensure that the curve (77) passes through the bin–hopper transition T. The parameter a is determined using the method of least squares; it is seen from figure 9 that (77) provides a good fit to the data. This is found to be true in all the cases considered here.

In §4, new coordinates (t, η) were introduced in place of the polar coordinates (r^*, θ). Using (77), the function $\xi(r^*, \theta)$ in (69) may now be chosen as

$$\xi(r^*, \theta) \equiv 1 - \frac{r^*}{a\{1 + m[\theta/\theta_w]^2\}}. \tag{79}$$

Thus $\xi = 0$ along the initial curve, and it increases on moving down the hopper.

We now discuss the effect of inertial terms and some of the material parameters on the downstream variables and the shock shape. The inertial terms in (61) and (62) are found to be small compared to the other terms. Hence a good approximation to the exact solution may be obtained by dropping the inertial terms. Making an additional assumption that $\tau_{(1)}^* = \sigma_{(1)}^* \sin\phi$, which is reasonable if $n \approx 1$, (61) and (62) can be manipulated to obtain

$$\cos(\hat{\gamma}_{(1)} + \hat{\gamma}_{(2)} + 2\psi) = -\sin\phi \cos(\hat{\gamma}_{(2)} - \hat{\gamma}_{(1)}). \tag{80}$$

The variable $\hat{\gamma}_{(2)}$ is known *a priori* only at the centreline and the wall, and is unknown elsewhere on the shock. Equation (80) may therefore be used to obtain an estimate for the orientation of the shock at the wall $\psi_w \equiv \psi(\theta = \theta_w)$. Equation (80) has two roots for ψ_w. It can be shown that, while one of the roots implies that the shock always lies outside the bunker, the other ensures that it always lies inside (Prakash 1989). Choosing the latter, we obtain an explicit relation for ψ_w, which may be used as an initial guess for the iteration scheme.

	$\rho^*_{(1)} = 0.82$		$\rho^*_{(1)} = 0.78$	
	$u = 0.0125$	$u = 0.125$	$u = 0.0125$	$u = 0.125$
ψ (deg.)	78.0	78.0	78.0	78.0
$\rho^*_{(2)}$	0.7661	0.7661	0.7655	0.7655
$\sigma^*_{(2)}$	29.7	29.7	28.3	28.3
$\gamma_{(2)}$ (deg.)	10.8	10.8	10.8	10.8
$-v^*_{r(2)}$	1.32×10^{-2}	1.32×10^{-1}	1.26×10^{-2}	1.26×10^{-1}

TABLE 1. Effect of variation in $\rho^*_{(1)}$ and u on shock slope and the downstream variables for Leighton Buzzard sand, with $\phi = 37°$, $\Gamma = 1.34$, $\lambda = 0.02$, $n = 1.05$, $\delta_b = \delta_h = 16°$, $\theta_w = 10°$, $\beta^* = 5.25$, and $\rho^*_b = 0.82$, at $\eta = 0.5$

n	N_h/N_b
1.05	12.1
1.20	17.3
1.50	55.6

TABLE 2. Effect of n on the ratio of normal stresses at the bin–hopper transition. Here N_h = normal stress on the hopper wall, and N_b = normal stress on the bin wall. Parameters values are as in table 1

As shown in table 1, the shock slope ψ and the downstream variables $\rho^*_{(2)}$, $\sigma^*_{(2)}$ and $\gamma_{(2)}$ are weak functions of u. This may be anticipated on account of the smallness of the inertial terms. On the other hand, $v^*_{r(2)}$ is approximately proportional to $\rho^*_{(1)} u$, in view of (60). Further, the variation of bin density $\rho^*_{(1)}$ from 0.82 to 0.78 does not significantly affect the downstream variables ψ, $\rho^*_{(2)}$ and $\gamma_{(2)}$.

It is interesting to note that the parameter n, which determines the shape of the yield locus (28) strongly affects the value of the ratio N_h/N_b (table 2). Here N_h and N_b are the normal stresses on the hopper and bin walls, respectively, at the bin–hopper transition. Measured values of N_h/N_b are in the range 2–13 (Jenike & Johanson 1968; Rao & Venkateswarlu 1974; Sundaram & Cowin 1979), suggesting that values of n close to 1 give more realistic estimates of N_h/N_b.

Figure 4 compares the predicted shape of the shock (DFT) with the rupture layer DAT observed by Michalowski (1987), and also his predicted rupture layer DET. It is seen that the actual rupture layer lies in between both the theoretical curves, but its shape resembles Michalowski's curve more closely. The rupture layers AC and AG, which separate material moving parallel to the wall from that moving radially, cannot be predicted with the present assumptions.

5.2. *The smooth-walled hopper*

Though the ultimate aim is to predict stress and velocity fields in a bunker with rough walls, it is instructive to first consider the special case of a bunker with rough bin walls ($\delta_b > 0$), and smooth hopper walls ($\delta_h = 0$). As computational times are found to be shorter in the latter case, certain features of theory may be explored in greater detail. In a similar vein, it is tempting to consider the simpler case of a smooth-walled bunker ($\delta_b = 0, \delta_h = 0$). However, with $\delta_b = 0$, the stress field (50), which provides values of σ^* and $\hat{\gamma}$ on the upstream side of the shock, is not approached asymptotically on moving downwards from the free surface of the fill.

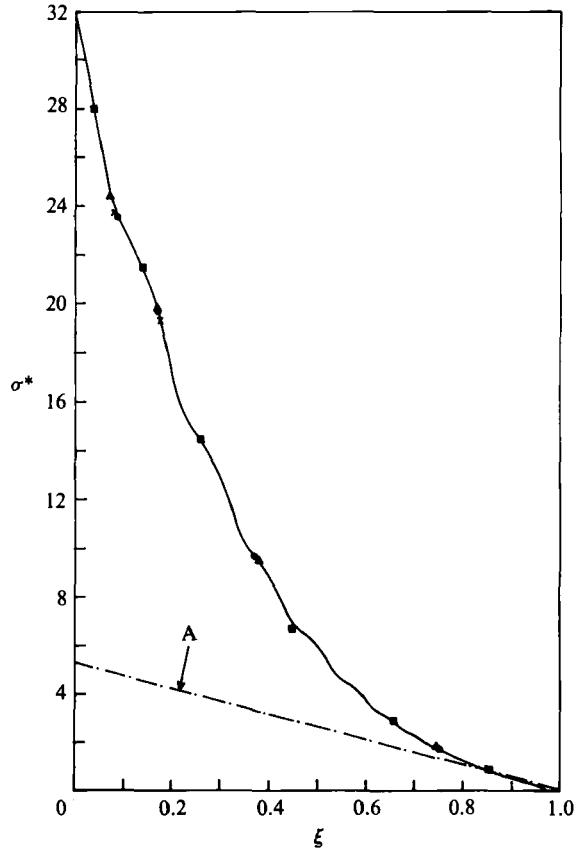

FIGURE 10. Stress profile along the centreline for a smooth-walled hopper: ——, ■, basic equations with ($\Delta t = 10^{-4}$, $\Delta\eta = 0.05$), ($\Delta t = 5 \times 10^{-5}$, $\Delta\eta = 0.025$), respectively; ●, ▲, ×, Mohr–Coulomb approximation with ($\Delta t = 2.5 \times 10^{-4}$, $\Delta\eta = 0.05$), ($\Delta t = 10^{-4}$, $\Delta\eta = 0.02$), ($\Delta t = 5 \times 10^{-5}$, $\Delta\eta = 0.01$), respectively. The dot-dashed curve (A) is the asymptotic stress field. The parameter values are: $\Gamma = 1.34$, $\lambda = 0.02$, $n = 1.05$, $\beta^* = 5.25$, $\rho_b^* = 0.82$, $u = 0.0125$, $\xi_e = 0.975$, $a = 5.733$, $\phi = 37°$, $\delta_b = 16°$, $\delta_h = 0°$ and $\theta_w = 10°$.

5.2.1. *Preliminary results*

The basic equations (23)–(27) are integrated numerically using the method outlined in §4, with the values of the variables on the downstream side of the entry shock as initial conditions. The results in figures 10–12 are for Leighton Buzzard sand, with $\beta^* = 5.25$, $u = 0.0125$ and $\xi_e = 0.975$. The latter corresponds to an exit slot radius $r_e^* = 0.144$, or a slot width of $D = 0.05$ m. This is only a nominal figure, for use with (69). The actual value of r_e^*, at which the exit condition is satisfied, may be determined as described in §5.2.3.

The full curve in figure 10 shows the profile of the mean stress σ^* along the centreline of the hopper, with a grid size of $\Delta t = 10^{-4}$ and $\Delta\eta = 0.05$. The squares, obtained with a finer grid size of $\Delta t = 5 \times 10^{-5}$, $\Delta\eta = 0.025$, are in close agreement with the full curve; this suggests convergence of the solution. The waviness in the stress profile has been observed in the incompressible case also (Savage & Yong 1970; Kaza 1982), where it was thought to be a genuine feature of the governing equations and not an artefact of the numerical method used.

Figure 11 shows the profile of γ, the orientation of the σ_1 axis, along the radial line

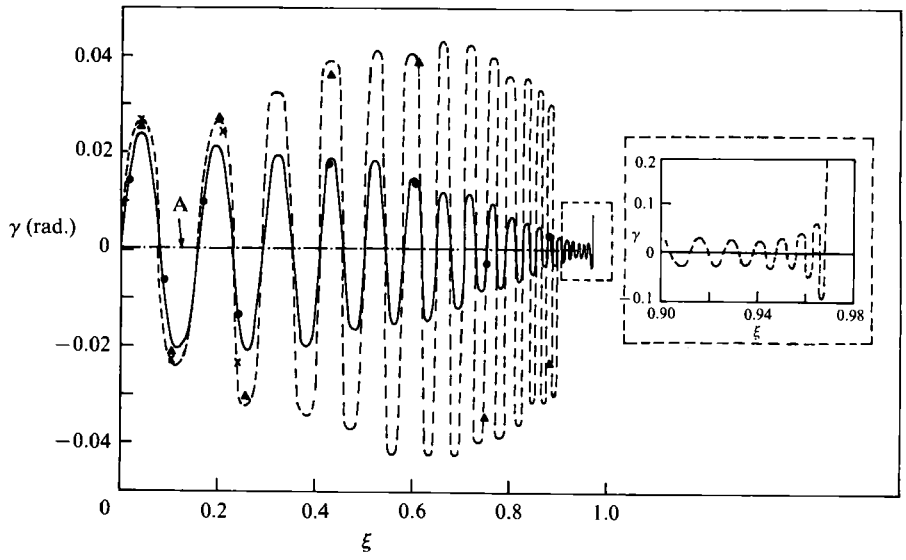

FIGURE 11. γ-profile along a radial line at $\eta = 0.5$ for a smooth-walled hopper: ——, – – –, basic equations with ($\Delta t = 10^{-4}$, $\Delta\eta = 0.05$), ($\Delta t = 5 \times 10^{-5}$, $\Delta\eta = 0.025$), respectively; ●, ▲, ×, Mohr–Coulomb approximation with ($\Delta t = 2.5 \times 10^{-4}$, $\Delta\eta = 0.05$), ($\Delta t = 10^{-4}$, $\Delta\eta = 0.02$), ($\Delta t = 5 \times 10^{-5}$, $\Delta\eta = 0.01$), respectively. The dot-dashed curve (A) is the asymptotic γ-profile. Oscillations observed on approaching the exit with the fine grid are shown in the inset. Parameter values are as in figure 10.

$\eta = 0.5$ (full curve). The oscillations decrease in amplitude on moving downwards, i.e. as ξ increases. However, the amplitude begins to increase rapidly in the vicinity of the exit slot, making it difficult to continue the integration. As discussed in §3.6, this behaviour is presumably due to the singularity in the momentum balances, which is manifested when $\sigma^* \to 0$ (figure 10). The broken curve in figure 11 shows the profile obtained with a finer grid size of $\Delta t = 5 \times 10^{-5}$, $\Delta\eta = 0.025$. Here the oscillations are relatively undamped, and the profile differs markedly from that obtained with the coarser grid (full curve). As indicated later, in §5.2.2, there is reason to believe that the broken curve represents the converged γ-profile. Thus the coarse grid is adequate for σ^* (figure 10), but not for γ. As the magnitude of γ is close to zero, small errors in γ do not affect the σ^* profile appreciably. Close to the exit slot, the amplitude of the oscillations increases rapidly, even with the fine grid, as shown in the inset to figure 11. Once again, this reflects the singularity in the momentum balances.

Figure 12 shows the density profile along the wall. The material dilates continuously on moving downwards, but the effect is most pronounced near the exit slot. This behaviour is qualitatively in accord with available data (Bosley *et al.* 1969; Van Zuilichem *et al.* 1974; Fickie *et al.* 1989).

While the present numerical scheme gives reasonable results, the computational time is excessive – with $\Delta t = 5 \times 10^{-5}$ and $\Delta\eta = 0.025$, a run in single precision takes about 3 hours on the DEC 1090 computer. The source of the difficulty appears to be the term $\partial\tau^*/\partial\rho^*$, which multiplies the derivatives of density in the compatibility condition (74). With the yield condition given by (28),

$$\frac{\partial\tau^*}{\partial\rho^*} = \frac{\sigma_c^* \sin\phi(\alpha)^{n/n_1}}{\lambda(\rho^*)^2}.$$

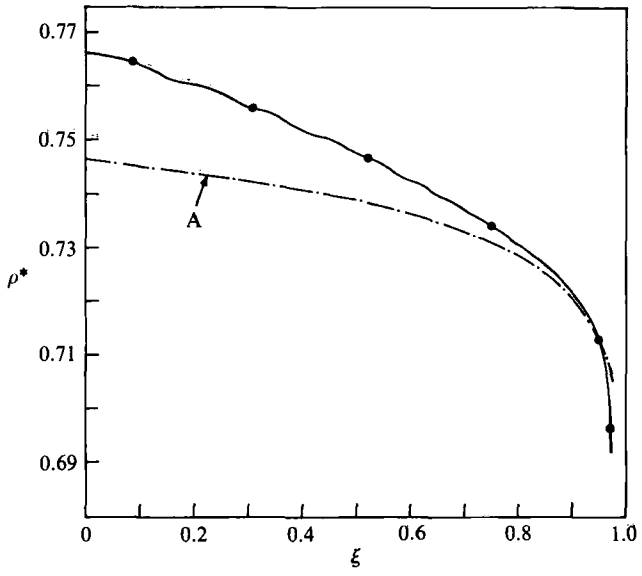

FIGURE 12. Density profile along the wall for a smooth-walled hopper: ——, basic equations with ($\Delta t = 10^{-4}$, $\Delta\eta = 0.05$); ●, Mohr–Coulomb approximation with ($\Delta t = 2.5 \times 10^{-4}$, $\eta = 0.05$). The dot-dashed curve (A) is the asymptotic density field. Parameter values are as in figure 10.

If α remains close to unity, as is the case in all the results presented here, $\partial\tau^*/\partial\rho^*$ becomes unbounded as $\lambda \to 0$. For example, using the parameter values listed in figure 10, the value of this term at $\xi = 0, \eta = 1$ is 1246. Thus small errors in evaluating the density field are amplified by this factor, and hence a fine grid is needed to ensure convergence.

5.2.2. *The Mohr–Coulomb approximation*

In this section an approximation is introduced, which reduces the computational time significantly. The basis for this approximation is the observation that the material remains close to the critical state $\alpha = 1$ over most of the hopper. For example, $\alpha(t = 0.98, \eta = 1.0) = 0.9909$. When $\alpha = 1$, the yield condition (28) reduces to the Mohr–Coulomb yield condition (51). Since $\alpha \approx 1$, it is proposed to use (51) in place of the actual yield condition throughout the hopper. Since τ^* does not then depend explicitly on ρ^*, density derivatives do not appear in the compatibility condition, and the source of stiffness is eliminated.

Using (51), the momentum balances (24) and (25) take the form

$$\rho^*\left[v_r^*\frac{\partial v_r^*}{\partial r^*}+\frac{v_\theta^*}{r^*}\frac{\partial v_r^*}{\partial\theta}-\frac{(v_\theta^*)^2}{r^*}\right]+[1-\sin\phi\cos 2\gamma]\frac{\partial\sigma^*}{\partial r^*}+2\sigma^*\sin\phi\sin 2\gamma\frac{\partial\gamma}{\partial r^*}$$
$$-\frac{\sin\phi\sin 2\gamma}{r^*}\frac{\partial\sigma^*}{\partial\theta}-\frac{2\sigma^*\sin\phi\cos 2\gamma}{r^*}\frac{\partial\gamma}{\partial\theta}-\frac{2\sigma^*\sin\phi\cos 2\gamma}{r^*}+\rho^*\cos\theta=0 \quad (81)$$

and

$$\rho^*\left[v_r^*\frac{\partial v_\theta^*}{\partial r^*}+\frac{v_\theta^*}{r^*}\frac{\partial v_\theta^*}{\partial\theta}+\frac{v_r^*v_\theta^*}{r^*}\right]-\sin\phi\sin 2\gamma\frac{\partial\sigma^*}{\partial r^*}-2\sigma^*\sin\phi\cos 2\gamma\frac{\partial\gamma}{\partial r^*}$$
$$+\frac{1+\sin\phi\cos 2\gamma}{r^*}\frac{\partial\sigma^*}{\partial\theta}-\frac{2\sigma^*\sin\phi\sin 2\gamma}{r^*}\frac{\partial\gamma}{\partial\theta}-\frac{2\sigma^*\sin\phi\sin 2\gamma}{r^*}-\rho^*\sin\theta=0. \quad (82)$$

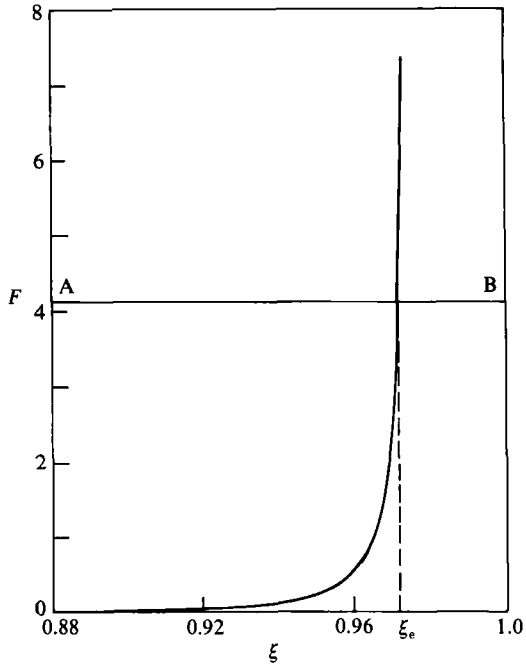

FIGURE 13. Plot of F as a function of ξ for a smooth-walled hopper: ——, $u = 0.0125$. Mohr–Coulomb approximation with ($\Delta t = 2.5 \times 10^{-4}$, $\Delta\eta = 0.05$). Other parameter values are as in figure 10. AB represents the right-hand side of (88).

Equations (81) and (82), together with (23), (26) and (27) constitute the governing equations for the Mohr–Coulomb approximation (MCA).

Unlike the basic equations (23)–(27), the equations of the MCA are hyperbolic, with five real and distinct characteristic roots $\lambda_i = \cot\psi_i$. These are given by

$$\psi_1 = \cot^{-1}(v_\theta^*/v_r^*); \quad \psi_{2,3} = -[\gamma \mp (\tfrac{1}{4}\pi - \tfrac{1}{2}\nu)]; \quad \psi_{4,5} = -[\gamma \mp (\tfrac{1}{4}\pi - \tfrac{1}{2}\phi)]. \tag{83}$$

The first three roots are identical to the roots of the basic equations, while the other two arise because of the MCA. Since the equations are hyperbolic, the modified Euler predictor-corrector method of Zucrow & Hoffman (1976, p. 341) can be used without making any changes. The initial and boundary conditions are also unaffected, except that $\bar{\phi}$ is replaced by ϕ in (47*b*).

The MCA has been introduced to mitigate computational difficulties associated with the basic equations. From another viewpoint, the equations of the MCA may be regarded as representing a model with a non-associated flow rule. This is because the angle of dilation ν is still computed from the old yield condition (28), which now plays the role of a plastic potential, and not from the Mohr–Coulomb yield condition (51).

We now discuss the results obtained with the MCA. The circles, triangles, and crosses in figure 10 represent the σ^* profiles for three different grid sizes. The profiles appear to have converged, and are in good agreement with the results obtained using the basic equations. In the case of the γ-profiles (figure 11), the circles lie close to the full curve, and the triangles and crosses are close to the broken curve. Thus the latter are likely to represent converged profiles. It is interesting to note that the MCA faithfully mimics the oscillations in the basic equations. The circles in figure 12 provide further evidence of the agreement between the basic and approximate equations. Regarding the velocity profiles, in both cases the circumferential velocity

v_θ^* is of order 10^{-4}, and oscillates about zero, while the radial velocity v_r^* grows like $(1/r^*)$ on moving downwards.

Turning to the issue of computational time, it is found that integration of the MCA equations in single precision, with a grid size of $\Delta t = 10^{-4}$ and $\Delta\eta = 0.02$, takes about 2 h and 12 min. This is significantly lower than the time of 3 h, which is needed to achieve comparable accuracy with the basic equations. If small errors in γ and v_θ^* can be tolerated, a coarser grid of $\Delta t = 2.5 \times 10^{-4}$, $\Delta\eta = 0.05$ suffices for the MCA (see figures 10–12). With this grid, it takes only about 28 min for a single run.

Since the MCA has been shown to be a good approximation, and it requires less computational time than the basic equations, all the results presented henceforth will be based on the MCA, unless otherwise indicated.

5.2.3. *The exit shock*

As discussed in §3.6 the following exit condition will be used: at the edges A and B of the exit slot (figure 5), the exit shock should be tangential to the characteristics AC and BC, which define the domain of determinacy of AB. Referring to (83) and figure 5, the root corresponding to the characteristic BC is given by

$$\psi_4 = -[\gamma - (\tfrac{1}{4}\pi - \tfrac{1}{2}\phi)]. \tag{84}$$

For the parameter values used here the other roots are excluded, since computations show that the characteristics corresponding to them are disposed to the right of BC. This is shown schematically by the lines BE, BF, BG, and BH in the inset to figure 5.

At the smooth hopper wall, $\gamma = 0, v_\theta^* = 0$, and hence (68), which determines the slope of the exit shock, reduces to

$$\frac{1}{r^*}\frac{\mathrm{d}r^*}{\mathrm{d}\theta}\bigg|_{\theta=\theta_w} = \tan\psi'_w = a_0 F(\zeta; r_e^*) + b_0, \tag{85}$$

where
$$a_0 \equiv \frac{\tan\theta_w}{1+\sin\phi}; \quad b_0 \equiv a_0(1-\sin\phi); \quad \psi'_w \equiv \psi'(\theta = \theta_w) \tag{86}$$

and
$$F(\zeta; r^*) \equiv \frac{\rho^*(v_r^*)^2}{\sigma^*}\bigg|_{\theta=\theta_w}; \quad \zeta^{\mathrm{T}} \equiv (\phi, n, \Gamma, \lambda, \delta_b, \delta_h, \rho_b^*, \theta_w, \beta^*, u). \tag{87}$$

The dependence of F on ζ follows from the governing equations (23), (26)–(28), (81), (82), the boundary conditions (48), and the initial conditions (49). In deriving (85), the Mohr–Coulomb yield condition (51) has been used. In view of (84) and (85), the exit condition is given by $\psi'_w = \psi_4$ or

$$F(\zeta; r_e^*) = \frac{\tan(\frac{1}{4}\pi - \frac{1}{2}\phi) - b_0}{a_0}. \tag{88}$$

For a given material, and a specified wall angle θ_w, (86) and (87) imply that (88) provides a relation between the density ρ_b^*, the reciprocal bin width β^*, the velocity u of the material in the bin, and the exit slot radius r_e^*. Since the range of poured densities is small, ρ_b^* will henceforth be treated as a fixed parameter, and (88) will be used to explore the interrelationships between the three parameters β^*, u and r_e^*.

For fixed values of β^* and u, the value of r_e^* may be determined by plotting $F(\zeta; r^*)$, obtained from (87), vs. r^*, or equivalently *vs.* ξ. On this plot, the right-hand side of (88) may be represented by a horizontal line, and its intersection with the curve $F(\zeta; \xi)$ fixes $\xi_e \equiv \xi(r_e^*, \theta_w)$ (see (79)).

The full curve in figure 13 shows a plot of F *vs.* ξ, for $u = 0.0125$ and $\beta^* = 5.25$. The value of F is small over most of the hopper, but it rises sharply near the exit slot. This

is caused by an increase in the inertial terms, and a decrease in σ^* as the exit is approached; indeed F may be regarded as a ratio of inertial to frictional effects. The monotonic increase of F with ξ results in a unique value $\xi_e = 0.972$, which corresponds to $r_e^* = 0.162$, or a slot width of 0.056 m. (Note that the value of ξ_e is slightly different from the nominal value $\xi_e = 0.975$, which has been used in (69) to generate the results shown in figures 10–13.) In all the cases examined here, a unique value of r_e^* is obtained for every pair of values of β^* and u.

Having located the exit slot corresponding to $u = 0.0125$ and $\beta^* = 5.25$, the exit shock is found by integrating (68), using an Euler scheme with a step size $|\Delta\eta| = 0.01$. It is found to lie below the plane of the exit slot, but within the desired domain of determinacy.

5.2.4. *Discharge rates*

A parameter of great interest in studies on hopper flow is the discharge rate or mass flow rate $\dot{M}$. In fact, an accurate prediction of $\dot{M}$ has been the cherished (and often unfulfilled) goal of most attempts. Results presented in this section are confined to smooth hopper walls, and hence cannot be compared directly with experiments. However, the dependence of $\dot{M}$ on some of the parameters may be examined. It is convenient to introduce a dimensionless discharge rate V_D based on the width D of the exit slot, and the thickness B of the bunker perpendicular to the plane of flow:

$$V_D \equiv \frac{\dot{M}}{\rho_{max} BD(gD)^{\frac{1}{2}}} = \frac{\rho_b^* u}{\sqrt{2}(r_e^* \sin\theta_w)^{\frac{3}{2}}}. \tag{89}$$

In the previous section, the value of r_e^* corresponding to specified values of u and β^* has been determined. However, the inverse situation is encountered while attempting to compare measured and predicted discharge rates, since both r_e^* and β^* are specified, and u has to be estimated. This involves an iterative procedure, as discussed in Prakash (1989).

For ease of exposition, it is helpful to replace u, β^* and r_e^* by three other parameters V_D, $\bar{\beta}$ and Ω respectively, where V_D is defined by (89), and

$$\bar{\beta} \equiv \frac{\beta^*}{r_e^*} = \frac{p_a}{\rho_{max} g r_e}; \quad \Omega \equiv \frac{r_w^*}{r_e^*} = \frac{1}{r_e^* \sin\theta_w} = \frac{2L}{D}. \tag{90}$$

Here $\bar{\beta}$ is inversely proportional to the exit slot radius, and Ω represents the ratio of the bin width to exit slot width. Based on earlier work (Davidson & Nedderman 1973; Prakash & Rao 1988), it may be anticipated that the discharge rate V_D is (i) independent of Ω for deep hoppers, i.e. for $\Omega \gg 1$, and (ii) a weak function of $\bar{\beta}$. Computations show that this is indeed the case, as discussed in Prakash (1989).

A similar behaviour is exhibited by the stress profiles along the hopper wall, corresponding to two different values of Ω, but virtually identical values of $\bar{\beta}$ (figure 14). Though the profiles differ markedly near the top of the hopper sections, they converge to a common asymptotic field near the exit. It is in this region that the profiles become independent of the height of fill.

The circles and crosses in figure 14 denote $\bar{\sigma}$-values on the upstream and downstream sides, respectively, of the shock at the bin–hopper transition. Though the jump in $\bar{\sigma}$ depends on the value of Ω, this is merely an artefact of the scaling used. In terms of $\sigma^* \equiv \sigma/(\rho_{max} gL)$, the stress jump $\sigma^*_{(2)} - \sigma^*_{(1)} = 22.2$, both for $\Omega = 32.9$ and for $\Omega = 16.5$. Thus $\sigma^*_{(2)} - \sigma^*_{(1)}$ is virtually independent of Ω. This result may be inferred from (61) and (62), provided the inertial terms are negligible. It would be interesting

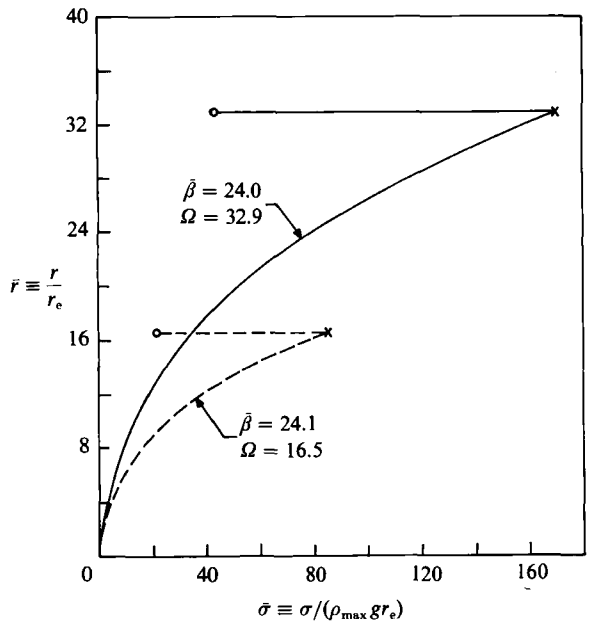

FIGURE 14. Dimensionless stress $\bar{\sigma} = \sigma/(\rho_{max} g r_e)$ along the wall, for two values of Ω: ---, $\beta^* = 8.4$, $u = 0.04$, $\xi_e = 0.96$; ——, $\beta^* = 4.2$, $u = 0.01414$, $\xi_e = 0.98$. Mohr–Coulomb approximation, with ($\Delta t = 2.5 \times 10^{-4}$, $\Delta\eta = 0.05$). Remaining parameter values are as in figure 10. The circles and crosses denote the bin stress and hopper stress, respectively, at the bin–hopper transition.

to measure $\sigma^*_{(2)} - \sigma^*_{(1)}$ in geometrically similar bunkers of various sizes, and check this conclusion.

5.2.5. *Comparison with the smooth wall, radial gravity problem*

For the special case of a hopper with smooth walls and gravity directed radially towards the vertex of the hopper, the basic equations admit a cylindrically symmetric solution of the form $\rho = \rho(r)$, $v_r = v_r(r)$, $v_\theta = 0$, $\sigma = \sigma(r)$ and $\gamma \equiv 0$. The functions $\rho(r)$ etc. may be determined by integrating ordinary differential equations in r (Prakash & Rao 1988). In that work initial conditions were specified along a traction-free surface. Here, for purposes of comparison with the vertical gravity results, the initial curve is assumed to be a circular arc through the bin–hopper transition T (figure 4). Along this curve, the field variables are set equal to the corresponding values for the vertical gravity problem, at the point T.

For $\bar{\beta} = 24.7, \Omega = 23.0$, and the other parameter values as listed in the caption of figure 10, it is found that for Leighton Buzzard sand flowing through a smooth-walled hopper, the assumption of radial gravity leads to a discharge rate V_D which is within 1% of the actual value. Similarly, the stress and density profiles do not differ significantly from those for the case of vertical gravity, as may be expected for small values of θ_w. However, one important difference must be noted. With vertical gravity, computations breakdown as $\sigma^* \to 0$, whereas this problem is not encountered with radial gravity. Hence, in the latter case, two discharge rates V_D and V_{Dt} can be computed, where V_D is based on the exit shock, and V_{Dt} is based on the traction-free surface. It is found that V_D is about 13% less than V_{Dt}; thus the use of the exit shock effects a significant reduction in the discharge rate.

For $\theta_w = 10°$, the exit shock can be constructed, but for $\theta_w = 30°$ it descends

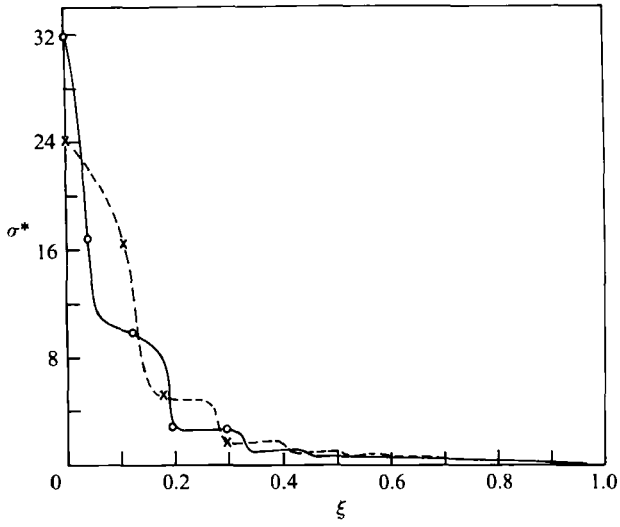

FIGURE 15. Stress profiles for a rough-walled hopper: ——, – – –, Mohr–Coulomb approximation along the centreline and wall, respectively, with ($\Delta t = 10^{-4}$, $\Delta\eta = 0.05$); ○, ×, basic equations along the centreline and wall, respectively, with ($\Delta t = 10^{-5}$, $\Delta\eta = 0.05$). The parameter values are $\Gamma = 1.34$, $\lambda = 0.02$, $n = 1.05$, $\beta^* = 5.25$, $\rho_b^* = 0.82$, $u = 0.0125$, $\xi_e = 0.975$, $a = 5.881$, $\phi = 37°$, $\delta_b = \delta_h = 16°$ and $\theta_w = 10°$.

steeply from the hopper wall, and intersects the traction-free surface before reaching the centreline. Thus the exit shock cannot be fully realized in this case. Further, the density (ρ^*) on the downstream side of the exit shock is found to be too low – around 0.23–0.38. These features are symptoms of deficiencies in the present exit condition.

5.3. *The rough-walled hopper*

5.3.1. *The Mohr–Coulomb approximation*

In this section, the assumption of smooth hopper walls is relaxed. Thus the effect of wall roughness may be examined, and discharge rates compared with experiments.

As in the case of the smooth-walled hopper, computations with the basic equations turn out to be time consuming. Using the parameters listed in the caption of figure 15, and a grid size of $\Delta t = 10^{-5}$, $\Delta\eta = 0.05$, an integration from $t = 0 (\xi = 0)$ to $t = 0.095 (\xi = 0.296)$ takes about 1 h. Since the hopper exit corresponds roughly to $t = 1$, it is estimated that a run from the entry shock to the exit will take about 10 h of computing time. With the existing facilities, this translates to about 10 days of real time per run. Hence, as before, the basic equations are abandoned, and the Mohr–Coulomb approximation (MCA) is invoked.

As in the case of the smooth-walled hopper, the state of stress remains close to the critical state $\alpha = 1$ for $0 \leqslant t \leqslant 0.095$. For example $\alpha(t = 0.095, \eta = 0.5) = 0.9920$. Further, in this range of t-values, there is satisfactory agreement between results obtained with the basic equations and the MCA equations. This is evident from figures 15–19, where the circles and crosses represent the former, and the full and broken curves the latter.

The time taken to integrate the MCA equations up to $t = 0.095$, with a grid size of $\Delta t = 10^{-4}, \Delta\eta = 0.05$, is about 6 min, as compared to 1 h for the basic equations. The key point to be noted is that the MCA permits a larger value of Δt to be used, without a concomitant reduction in accuracy. The accuracy of the MCA was checked by

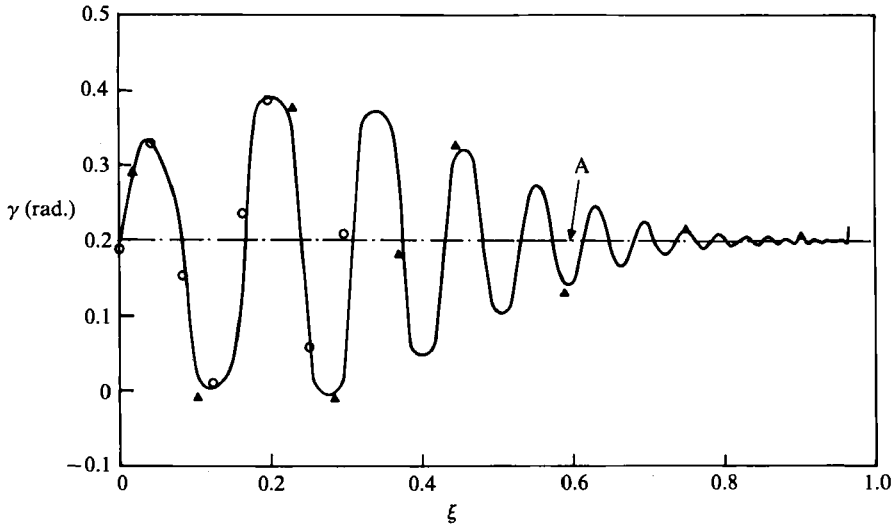

FIGURE 16. γ-profile along a radial line at $\eta = 0.5$ for a rough-walled hopper: ——, ▲, Mohr–Coulomb approximation with ($\Delta t = 10^{-4}$, $\Delta\eta = 0.05$), ($\Delta t = 5 \times 10^{-5}$, $\Delta\eta = 0.025$), respectively; ○, basic equations with ($\Delta t = 10^{-5}$, $\Delta\eta = 0.05$). The dot-dashed curve (A) is the asymptotic γ-field. Parameter values are as in figure 15.

integrating the equations with a finer grid of $\Delta t = 5 \times 10^{-5}$, $\Delta\eta = 0.025$. For instance, figure 16 shows satisfactory agreement between the γ-profiles for the two grid sizes, denoted by the triangles and the full curve.

A run from the initial curve to $t = 0.905$, where the computations break down, takes about 50 min, as compared to an estimated 10 h for the basic equations. Thus the MCA leads to a significant reduction in the computation time, and the effect is more pronounced than in the case of the smooth-walled hopper.

In view of the above discussion, all further results will be based on the MCA only. Figures 15–19 show the profiles of σ^*, γ, ρ^*, v_θ^* and v_r^* along the radial lines. They are qualitatively similar to the profiles for a smooth-walled hopper (figures 10–12), and exhibit a waviness which is damped as ξ increases. A possible reason for this damping is discussed in the section below on asymptotic fields. As before, the solution breaks down when $\sigma^* \to 0$. However, it has been possible to integrate the equations until the value of σ^* is fairly small – about 6.5×10^{-3} (at $\eta = 1$) in the present case, which corresponds to $\sigma = 125\ \mathrm{N/m^2}$. It may be noted that the strain-gauge type of load cells, which are used for wall stress measurements in bunkers, have an accuracy of about 7–60 $\mathrm{N/m^2}$ (Bransby & Blair-Fish 1974; Tüzün & Nedderman 1985).

Figures 18 and 19 show that the circumferential velocity v_θ^* remains small throughout the hopper, and the flow is nearly radial. This conclusion may not hold for large values of θ_w.

Turning to the exit condition, the rough-wall counterpart of (88) is found to be

$$F(\zeta; r_e^*) = \frac{\tan[\frac{1}{4}\pi - \frac{1}{2}\phi - \gamma_w] - b_1}{a_1}, \tag{91}$$

where
$$a_1 \equiv \frac{\sin\theta_w}{\cos\theta_w + \sin\phi\cos(2\gamma_w + \theta_w)}; \quad b_1 \equiv \frac{\sin\theta_w - \sin\phi\sin(2\gamma_w + \theta_w)}{\cos\theta_w + \sin\phi\cos(2\gamma_w + \theta_w)}, \tag{92}$$

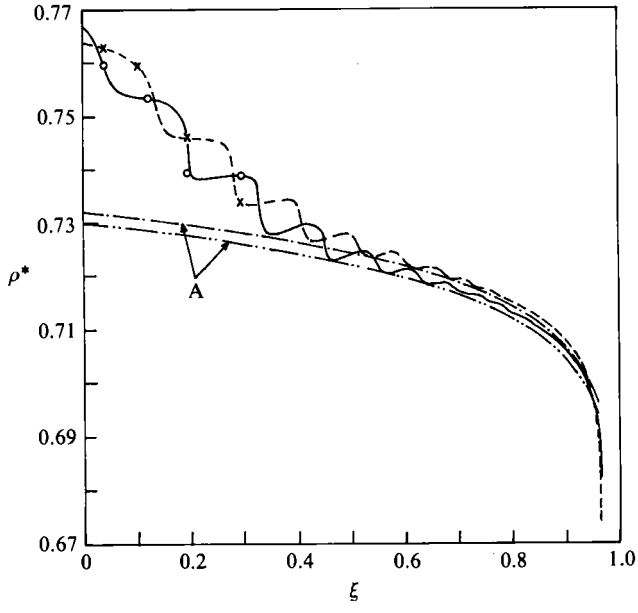

FIGURE 17. Density profiles for a rough-walled hopper: ——, – – –, Mohr–Coulomb approximation along the centreline and wall, respectively, with ($\Delta t = 10^{-4}$, $\Delta\eta = 0.05$); ○, ×, basic equations along the centreline and wall, respectively, with ($\Delta t = 10^{-5}$, $\Delta\eta = 0.05$); – · · —, — · —, asymptotic density fields along the centreline and wall, respectively. Parameter values are as in figure 15.

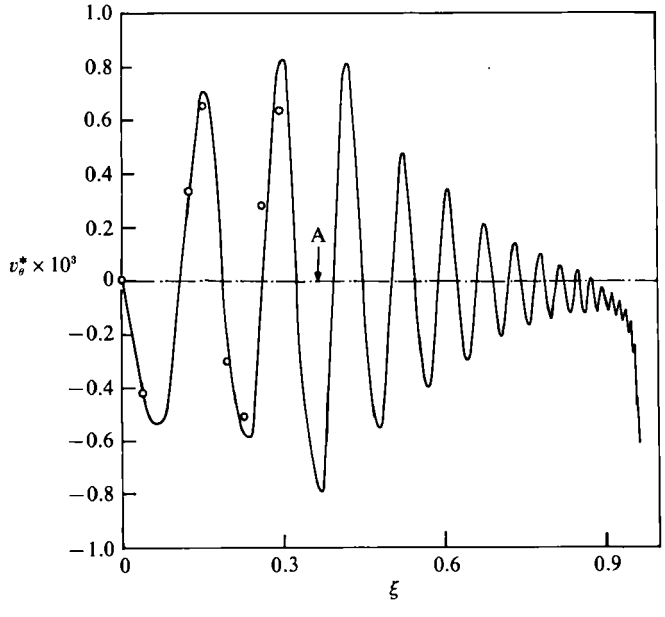

FIGURE 18. Circumferential velocity along a radial line at $\eta = 0.5$ for a rough-walled hopper: ——, Mohr–Coulomb approximation with ($\Delta t = 10^{-4}$, $\Delta\eta = 0.05$); ○, basic equations with ($\Delta t = 10^{-5}$, $\Delta\eta = 0.05$). The dot-dashed curve (A) is the asymptotic velocity field. Parameter values are as in figure 15.

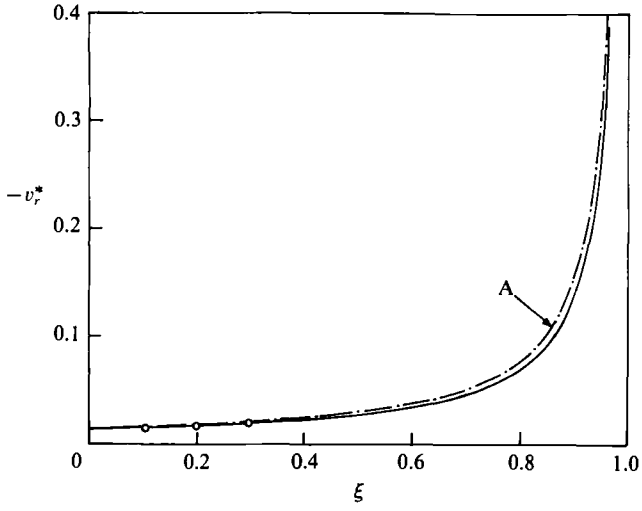

FIGURE 19. Radial velocity along the centreline for a rough-walled hopper: ——, Mohr–Coulomb approximation with ($\Delta t = 10^{-4}$, $\Delta\eta = 0.05$); ○, basic equations with ($\Delta t = 10^{-5}$, $\Delta\eta = 0.05$). The dot-dashed curve (A) is the asymptotic velocity field. Parameter values are as in figure 15.

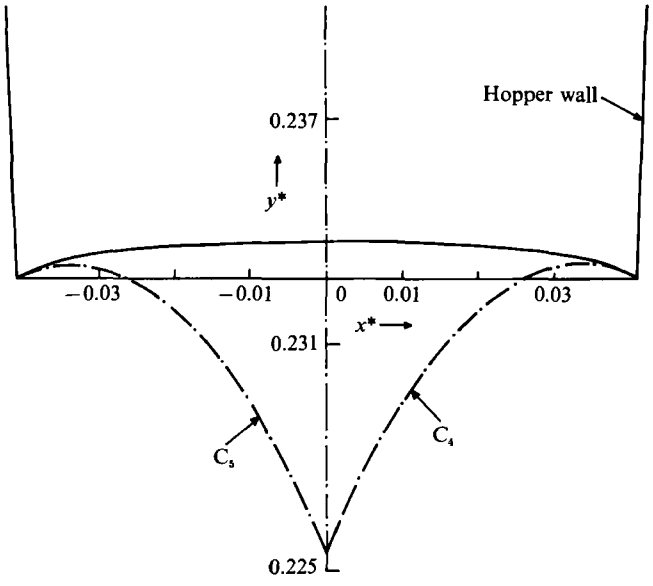

FIGURE 20. Exit shock (——) and 'outermost' characteristics (–·–) for a rough-walled hopper. Mohr–Coulomb approximation with ($\Delta t = 10^{-4}$, $\Delta\eta = 0.05$). Other parameter values are as in figure 15.

$\gamma_w \equiv \gamma(r_e^*, \theta_w)$, and $F(\zeta; r_e^*)$ is defined by (87). Using (91), and following the procedure described in §5.2.3, the exit shock may be constructed. This is shown by the full curve in figure 20; in contrast to the smooth-walled shock, it lies above the plane of the exit slot. However, it is only marginally above, the maximum height relative to the exit slot being about 1 mm.

5.3.2. *Perturbation solution for the asymptotic stress and density fields*

In this section, an attempt is made to deduce certain features of solutions to the basic equations. This is largely motivated by earlier work on incompressible flow, which suggests that stress and velocity fields converge to certain asymptotic fields, as r^* decreases, i.e. as ξ increases (Johanson 1964; Jenike 1965; Pitman 1986). Further, similar behaviour was observed in the compressible, smooth-wall, radial gravity problem, where the existence of an asymptotic density field was also demonstrated (Prakash & Rao 1988). It should be noted that these asymptotic fields are particular solutions of the basic equations, for the special case of negligible inertial effects. Indeed, significant deviations from these fields occur near the exit slot, owing to growing inertial effects. Therefore, the inertial terms will be omitted from the momentum balances in the present analysis also. The incompressible results can be exploited by using a perturbation solution based on a parameter which is a measure of density variation. Thus the base state or zero-order solution represents incompressible flow, whereas higher-order correction terms reflect the effect of compressibility. Details of the procedure are described below.

The parameter λ, which occurs in the relation (30) between the critical-state mean stress σ_c^* and the density ρ^*, is a suitable perturbation parameter. To see this, note that it may be rearranged to get

$$\frac{1}{\rho^*} = \Gamma - \lambda \ln\left[\frac{\sigma_c^*}{\beta^*}\right]. \tag{93}$$

Thus, in the limit $\lambda \to 0, \rho^* \to 1/\Gamma$, which may be regarded as the 'incompressible' density. Further, since λ is expected to be a small parameter – around 0.02 for Leighton Buzzard sand – all the variables may be expanded in powers of λ to get

$$\sigma_c^* = \sigma_{c0}^*(r^*, \theta) + \lambda \sigma_{c1}^*(r^*, \theta) + \ldots \tag{94}$$

and so on.

Substituting expansions of the form (94) into the basic equations (23)–(27) and collecting terms of $O(\lambda^0)$ and $O(\lambda^1)$ gives two sets of equations. Let us first consider the equations of $O(\lambda^0)$:

$$\frac{\partial v_{r0}^*}{\partial r^*} + \frac{1}{r^*}\frac{\partial v_{\theta 0}^*}{\partial \theta} + \frac{v_{r0}^*}{r^*} = 0, \tag{95}$$

$$\frac{\partial}{\partial r^*}(\alpha_0 \sigma_{c0}^* - \tau_0^* \cos 2\gamma_0) - \frac{1}{r^*}\frac{\partial}{\partial \theta}(\tau_0^* \sin 2\gamma_0) - \frac{2\tau_0^* \cos 2\gamma_0}{r^*} + \rho_0^* \cos\theta = 0, \tag{96}$$

$$-\frac{\partial}{\partial r^*}(\tau_0^* \sin 2\gamma_0) + \frac{1}{r^*}\frac{\partial}{\partial \theta}(\alpha_0 \sigma_{c0}^* + \tau_0^* \cos 2\gamma_0) - \frac{2\tau_0^* \sin 2\gamma_0}{r^*} - \rho_0^* \sin\theta = 0, \tag{97}$$

$$\cos 2\gamma_0\left[\frac{\partial v_{\theta 0}^*}{\partial r^*} + \frac{1}{r^*}\frac{\partial v_{r0}^*}{\partial \theta} - \frac{v_{\theta 0}^*}{r^*}\right] - \sin 2\gamma_0\left[\frac{\partial v_{r0}^*}{\partial r^*} - \frac{1}{r^*}\frac{\partial v_{\theta 0}^*}{\partial \theta} - \frac{v_{r0}^*}{r^*}\right] = 0, \tag{98}$$

$$\cos 2\gamma_0\left[\frac{\partial v_{r0}^*}{\partial r^*} + \frac{1}{r^*}\frac{\partial v_{\theta 0}^*}{\partial \theta} + \frac{v_{r0}^*}{r^*}\right] - \sin \nu_0\left[\frac{\partial v_{r0}^*}{\partial r^*} - \frac{1}{r^*}\frac{\partial v_{\theta 0}^*}{\partial \theta} - \frac{v_{r0}^*}{r^*}\right] = 0, \tag{99}$$

where

$$\rho_0^* = \frac{1}{\Gamma}. \tag{100}$$

In (96) and (97), the mean stress σ^* has been replaced by $\alpha\sigma_c^*$. It is convenient to do so, since the yield condition (28) involves α, rather than σ^*.

Equations (95) and (99) imply

$$\sin\nu_0 \frac{\partial v_{r0}^*}{\partial r^*} = 0$$

or, since $\partial v_{r0}^*/\partial r^* \neq 0$ in general, $\sin\nu_0 = 0$. Therefore, it follows from (31) that

$$\alpha_0 = 1 \tag{101}$$

and hence from (29) and (28)

$$\sigma_0^* = \sigma_{c0}^*; \quad \tau_0^* = \sigma_{c0}^* \sin\phi = \sigma_0^* \sin\phi. \tag{102}$$

Thus the Mohr–Coulomb approximation (51) is recovered in the incompressible limit $\lambda \to 0$, and (95)–(98) are identical in form to the commonly used incompressible equations (see, for example, Jenike 1964*b*).

It is well known that the incompressible equations admit an exact solution of the form (Jenike 1964*b*)

$$\sigma_0^* = \sigma_{c0}^* = r^* b_0(\theta); \quad \gamma_0 = g_0(\theta), \tag{103}$$

$$v_{r0}^* = \frac{w_0(\theta)}{r^*}; \quad v_{\theta 0}^* = 0, \tag{104}$$

where the functions b_0, g_0, and w_0 are determined by integrating ordinary differential equations in θ. Equations (103) represent the 'radial stress field', and (104) the 'radial velocity field'; these are the incompressible asymptotic fields referred to earlier.

Having solved the equations of $O(\lambda^0)$, we turn to the equations of $O(\lambda^1)$. These are given by

$$\frac{\partial v_{r1}^*}{\partial r^*} + \frac{1}{r^*}\frac{\partial v_{\theta 1}^*}{\partial \theta} + \frac{v_{r1}^*}{r^*} + \frac{\rho_0^* w_0}{(r^*)^2} = 0, \tag{105}$$

$$\frac{\partial}{\partial r^*}[\sigma_1^* - \tau_1^* \cos 2g_0 + 2r^* b_0 \gamma_1 \sin\phi \sin 2g_0] - \frac{1}{r^*}\frac{\partial}{\partial\theta}[\tau_1^* \sin 2g_0 + 2r^* b_0 \gamma_1 \sin\phi \cos 2g_0]$$

$$- \frac{2}{r^*}[\tau_1^* \cos 2g_0 - 2r^* b_0 \gamma_1 \sin\phi \sin 2g_0] + \rho_1^* \cos\theta = 0, \tag{106}$$

$$-\frac{\partial}{\partial r^*}[\tau_1^* \sin 2g_0 + 2r^* b_0 \gamma_1 \sin\phi \cos 2g_0] + \frac{1}{r^*}\frac{\partial}{\partial\theta}[\sigma_1^* + \tau_1^* \cos 2g_0 - 2r^* b_0 \gamma_1 \sin\phi \sin 2g_0]$$

$$- \frac{2}{r^*}[\tau_1^* \sin 2g_0 + 2r^* b_0 \gamma_1 \sin\phi \cos 2g_0] - \rho_1^* \sin\theta = 0, \tag{107}$$

$$\cos 2g_0\left[\frac{\partial v_{\theta 1}^*}{\partial r^*} + \frac{1}{r^*}\frac{\partial v_{r1}^*}{\partial\theta} - \frac{v_{\theta 1}^*}{r^*}\right] - \sin 2g_0\left[\frac{\partial v_{r1}^*}{\partial r^*} - \frac{1}{r^*}\frac{\partial v_{\theta 1}^*}{\partial\theta} - \frac{v_{r1}^*}{r^*}\right] + \frac{4 w_0 \gamma_1}{(r^*)^2 \cos 2g_0} = 0, \tag{108}$$

and

$$\alpha_1 = \frac{-\rho_0^*(n-1)\cos 2g_0}{2n \sin\phi}. \tag{109}$$

The zero-order solution has been used to simplify (105)–(109). Further, (93) and (103) imply

$$\rho_1^* = \frac{1}{\Gamma^2}\ln\left(\frac{\sigma_{c0}^*}{\beta^*}\right) = \rho_{11}(\theta) + \rho_{12}\ln r^*, \tag{110}$$

where

$$\rho_{11}(\theta) = \frac{1}{\Gamma^2}\ln\left(\frac{b_0(\theta)}{\beta^*}\right); \quad \rho_{12} = \frac{1}{\Gamma^2}. \tag{111}$$

For typical parameter values, $g_0(\theta)$ is found to increase monotonically from zero at $\theta = 0$ to $\gamma_{0w} \equiv \gamma_p(\bar{\phi} = \phi)$ (see (47*b*)) at $\theta = \theta_w$. Since $n > 1$, and $2g_0(\theta_w) < \frac{1}{2}\pi$, it follows from (109) that (i) $\alpha_1 < 0$, and (ii) the largest value of $|\alpha_1|$ occurs at the centreline.

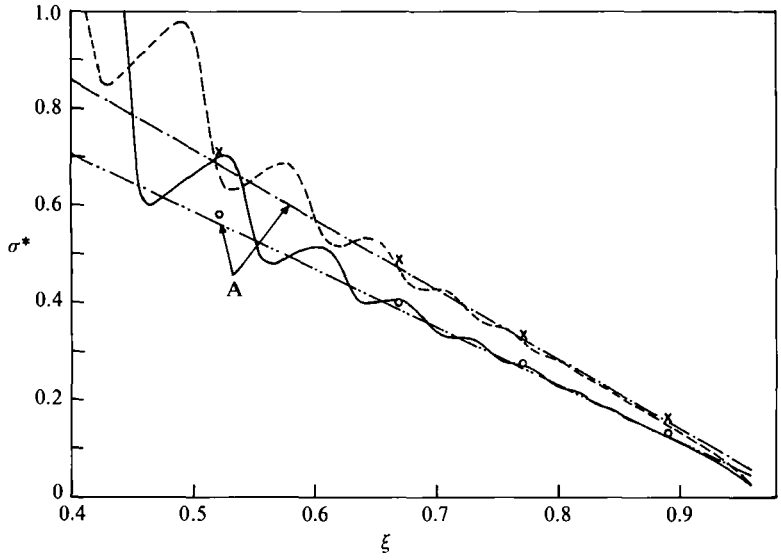

FIGURE 21. Stress profiles obtained by numerical integration of the Mohr–Coulomb approximation with ($\Delta t = 10^{-4}$, $\Delta\eta = 0.05$), along the centreline (——) and wall (– – –), compressible asymptotic stress fields along the centreline (—··—) and wall (—·—), and radial stress fields along the centreline (○) and wall (×), for a rough-walled hopper. Parameter values are as in figure 15.

Thus $\alpha = 1+\lambda\alpha_1 < 1$, and hence the material dilates as it flows down the hopper; further the dilation is expected to be more at the centreline than at the wall.

With ρ_1^* given by (110), the momentum balances (106) and (107) admit a solution of the form

$$\sigma_{c1}^* = b_{11}(\theta)\, r^* + b_{12}(\theta)\, r^* \ln r^*; \quad \gamma_1 = g_{11}(\theta) + g_{12}(\theta) \ln r^*. \tag{112a, b}$$

Substituting (112b) into the coaxiality condition (108), it is found that the equation of continuity (105) and the coaxiality condition (108) admit a solution of the form

$$v_{r1}^* = \frac{w_{11}(\theta)}{r^*} + \frac{w_{12}(\theta) \ln r^*}{r^*}; \quad v_{\theta 1}^* = -\frac{h(\theta)}{r^*}, \tag{113}$$

where

$$h(\theta) \equiv \int_0^\theta [\rho_0^*\, w_0(\theta') + w_{12}(\theta')]\, \mathrm{d}\theta' \tag{114}$$

and the functions b_{11}, b_{12}, g_{11}, g_{12}, w_{11} and w_{12} are determined by integrating ordinary differential equations, as discussed in Appendix C. It is interesting to note that $b_{12} = \rho_0^* b_0$; $g_{12} = 0$; $w_{12} = -\rho_0^* w_0$. Hence (113) and (114) imply $v_{\theta 1}^* = 0$, and consequently the velocity field is radial to $O(\lambda)$.

The functions w_0 and w_{11} are of the form $w_0 = w_0(\theta; P_1)$; $w_{11} = w_{11}(\theta; P_1, P_2)$, where P_1 and P_2 are integration constants. Within the context of the asymptotic fields, the boundary conditions that must be prescribed for w_0 and w_{11} are not evident. Here we choose the values of P_1 and P_2 so that the exit condition (91) is satisfied approximately at the desired exit slot radius $r^* = r_e^*$, as explained in Appendix C.

The curves marked A in figures 16, 17, and 21 show the asymptotic fields for γ, ρ^*, and σ^*. As ξ increases, the profiles obtained by numerical integration of the MCA tend to converge to these fields. Though $\sigma^*(\theta = 0) > \sigma^*(\theta = \theta_w)$ at the top of the hopper section $\xi = 0$ (figure 15), the trend is reversed for $\xi > 0.542$ (figure 21), in keeping with the behaviour predicted by the asymptotic fields. Similarly, for

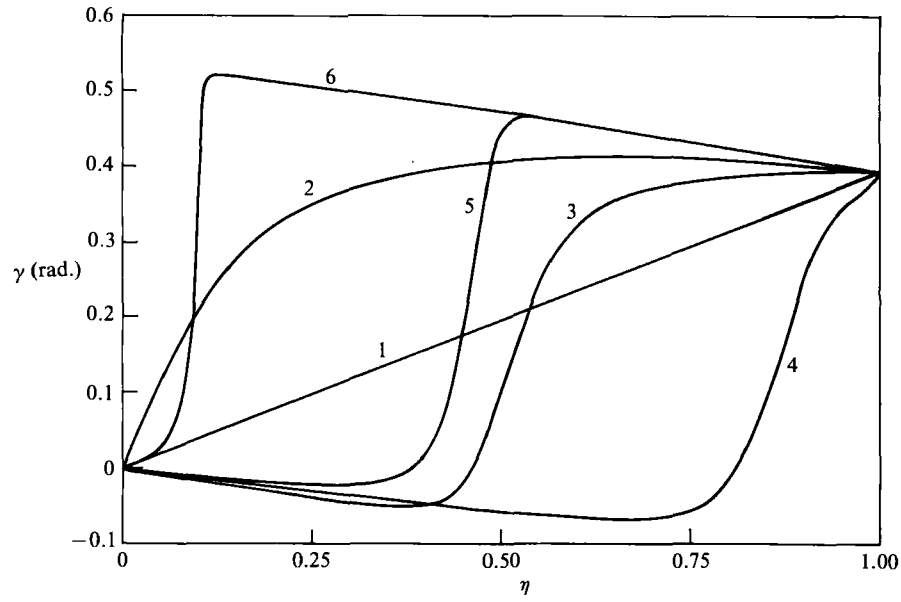

FIGURE 22. Profiles of γ across the hopper at various values of t: curve 1, $t = 0$; 2, $t = 0.03$; 3, $t = 0.06$; 4, $t = 0.1$; 5, $t = 0.12$; 6, $t = 0.13225$. Mohr–Coulomb approximation with ($\Delta t = 5 \times 10^{-5}$, $\Delta\eta = 0.025$). Parameter values are: $\Gamma = 1.34$, $\lambda = 0.02$, $n = 1.05$, $\beta^* = 35$, $\rho_b^* = 0.82$, $u = 0.04$, $\xi_e = 0.92$, $a = 3.96$, $\phi = 31°$, $\delta_b = \delta_h = 15°$ and $\theta_w = 15°$.

$\xi > 0.542$ the density at the centreline is lower than that at the wall (figure 17), as expected. Figure 21 shows that the σ^* profiles deviate from the asymptotic fields in the region $0.88 < \xi < 0.96$, which corresponds to about three exit slot radii. Thus inertial effects are confined to a small region near the exit slot. The asymptotic radial velocity field, estimated by the procedure discussed in Appendix C, lies within 16% of the profile obtained by numerical integration of the MCA (figure 19). For $\lambda = 0.02$, the compressible asymptotic stress field and the incompressible radial stress field [equation (103)] do not differ significantly, as shown by the curves marked A, and the crosses and circles in figure 21. However, for $\lambda = 0.05$ there is a marked difference between the two, and the actual stress profile converges to the compressible asymptotic field (Prakash 1989).

Figures 10 and 12 show that in the smooth-walled hopper case also, stress and density profiles obtained by numerical integration of the basic equations converge to the asymptotic fields as ξ increases. However the γ-profile in figure 11 (broken curve) does not converge to the asymptotic field, unlike in the rough-walled case (figure 16). It should be noted that in the incompressible case, Kaza (1982) has shown by examining an approximate version of the governing equations, that for a smooth-walled hopper, perturbations to the radial stress field are downward unstable for $\phi < 42°$.

5.3.3. *Computational difficulties with larger wall angles*

All the results presented so far have been confined to $\theta_w = 10°$. For a larger wall angle of $\theta_w = 15°$, attempts to integrate downwards from the entry shock were not successful. For example, the γ-profiles in figure 22 display a 'travelling wave' type of behaviour. The waves move across the hopper rapidly, and it is difficult to

integrate the equations beyond $t = 0.13225\,(\xi = 0.284)$. The reason for the difficulty becomes apparent on examining the directions of the C_4 characteristics at various locations on the line $t = 0.13225$. Close to $\eta = 0.125$, the characteristics change direction sharply and become nearly parallel to the η-axis. Thus the solution cannot be continued further with the present coordinate system. In addition, the characteristics appear to converge in this region, suggesting the formation of a shock.

It is interesting to note that similar problems also arise in the incompressible case for $\theta_w = 15°$, when a modified form of the entry shock is used as the initial condition. The incompressible approximation is discussed later, in §5.4.

If a shock does form, a method has to be devised to locate the point at which it forms, and then track it through the hopper. As we do not know how this is to be done, a simpler alternative is adopted here, as indicated below.

Initial conditions based on the entry shock are abandoned, and conditions based on the asymptotic fields are adopted in both the compressible and the incompressible cases. Details are given in Appendix C. A similar procedure was used by Kaza & Jackson (1982*a*) in the incompressible case. It is hoped that the actual solution will converge to the asymptotic fields, after experiencing rapid changes in the upper part of the hopper. Clearly this modification of the initial conditions is not a satisfactory resolution of the problem, but merely one that permits a solution to be obtained. It is hoped that the entry region will be examined more carefully in future, with reference to: (i) numerical integration using an alternative system of coordinates; for example, if the trajectory of the major principal stress axis is used as a coordinate curve, then the characteristics always have a constant orientation relative to it, (ii) the possible development of shocks from smooth initial data, and (iii) the convergence of solutions to the asymptotic fields.

5.3.4. *Discharge rates*

In this section, discharge rates predicted by the present theory will be compared with the experimental results of Nguyen *et al.* (1980), for the flow of sand through a plane bunker with lucite walls.

The quantity of interest is the dimensionless discharge rate V_D, defined by (89). It is convenient to rewrite this as

$$V_D = \frac{-\int_0^{\theta_w} \rho^* v_r^* r^* \,\mathrm{d}\theta}{\sqrt{2}(r_e^* \sin\theta_w)^{\frac{3}{2}}}, \tag{115}$$

where the integration is performed across any circular arc.

Nguyen *et al.* (1980) report discharge rates for wall angles in the range $15 \leqslant \theta_w \leqslant 90°$. As mentioned in the previous section, the use of initial conditions based on the entry shock led to computational difficulties for $\theta_w = 15°$. Since these are likely to persist for larger wall angles, alternative initial conditions based on the asymptotic fields will be used here, as explained in Appendix C. Using the equations for the asymptotic fields, (115) may be rewritten as

$$V_D = V_{D0} + \lambda V_{D1} \equiv V_{Da}, \tag{116}$$

where

$$V_{D0} = \frac{-\rho_0^*}{\sqrt{2}(r_e^* \sin\theta_w)^{\frac{3}{2}}} \int_0^{\theta_w} w_0 \,\mathrm{d}\theta; \quad V_{D1} = \frac{-1}{\sqrt{2}(r_e^* \sin\theta_w)^{\frac{3}{2}}} \int_0^{\theta_w} (\rho_0^* w_{11} + \rho_{11} w_0) \,\mathrm{d}\theta. \tag{117}$$

θ_w (deg.)	r_e^*	P_0	$P_0 V_{Da}$	r^*
15	0.322	1.0	0.801	0.343
15	0.322	0.89	0.713	0.317
22	0.222	1.0	0.645	0.234
22	0.222	0.92	0.593	0.222
32	0.157	1.0	0.415	0.162
32	0.157	0.92	0.382	0.154

TABLE 3. Compressible discharge rates ($P_0 V_{Da}$) corresponding to various exit slot radii (r^*). Mohr–Coulomb approximation. Parameter values and grid sizes are as in figure 23

With $w_0(\theta)$ and $w_{11}(\theta)$ obtained as described in Appendix C, the integrals in (117) may be evaluated by quadrature. Here it is found convenient to use the following alternative procedure, for the reason discussed below. Introducing new variables z_0 and z_1, defined by the differential equations

$$\frac{dz_0}{d\theta} = w_0; \quad \frac{dz_1}{d\theta} = (\rho_0^* w_{11} + \rho_{11} w_0) \tag{118}$$

and satisfying the initial conditions

$$z_0(0) = 0; \quad z_1(0) = 0 \tag{119}$$

it follows that $$V_{D0} = \frac{-\rho_0^* z_0(\theta_w)}{\sqrt{2}(r_e^* \sin\theta_w)^{\frac{3}{2}}}; \quad V_{D1} = \frac{-z_1(\theta_w)}{\sqrt{2}(r_e^* \sin\theta_w)^{\frac{3}{2}}}. \tag{120}$$

Thus the use of the functions z_0 and z_1 permits the evaluation of V_{D0} and V_{D1} simultaneously with w_0 and w_{11}, when (118) are integrated numerically along with the differential equations for w_0 and w_{11}.

For a specified value of r_e^*, (116)–(120) determine an approximate discharge rate $V_{Da} = V_{D0} + \lambda V_{D1}$. The value is not exact, since evaluation of the constants P_1 and P_2 in the expressions for w_0 and w_{11} involves simplifying assumptions (see Appendix C). The procedure for obtaining the actual discharge rate V_D which corresponds to r_e^* will be discussed shortly.

It is found that $V_{D1} < 0$ for the parameter values used here. Thus the approximate analysis suggests that inclusion of density variation reduces the discharge rate; this is borne out by the results presented later.

To determine the actual discharge rate V_D, the asymptotic fields are used as initial conditions along the entry shock, and the MCA equations are integrated downwards. The exit condition will be satisfied at some point $r^* = r_1^*$, which is $\neq r_e^*$ in general. Thus the discharge rate V_{Da} (equation (116)) corresponds to r_e^* when approximate analysis is used, and to r_1^* when the MCA equations are integrated. Multiplying the constants P_1 and P_2 by a common factor P_0, and repeating the procedure, a discharge rate $P_0 V_{Da}$ and an exit slot radius $r^* = r_2^*$ are obtained. A suitable choice of P_0 (typically in the range 0.85–0.92) ensures that r_1^* and r_2^* bracket the desired value r_e^*, as shown in table 3. The discharge rate V_D is then found from V_{Da} and $P_0 V_{Da}$ by linear interpolation. A similar procedure is adopted in the incompressible case also.

Let us briefly consider the choice of parameter values. The angle of internal friction ϕ, and the angle of wall friction δ, are taken to be 31° and 15°, respectively, as given by Nguyen *et al.* (1980). The precise values of the bin width $2L$, the slot width D, and the particle density ρ_s, have not been reported by Nguyen *et al.* (1980). Here we

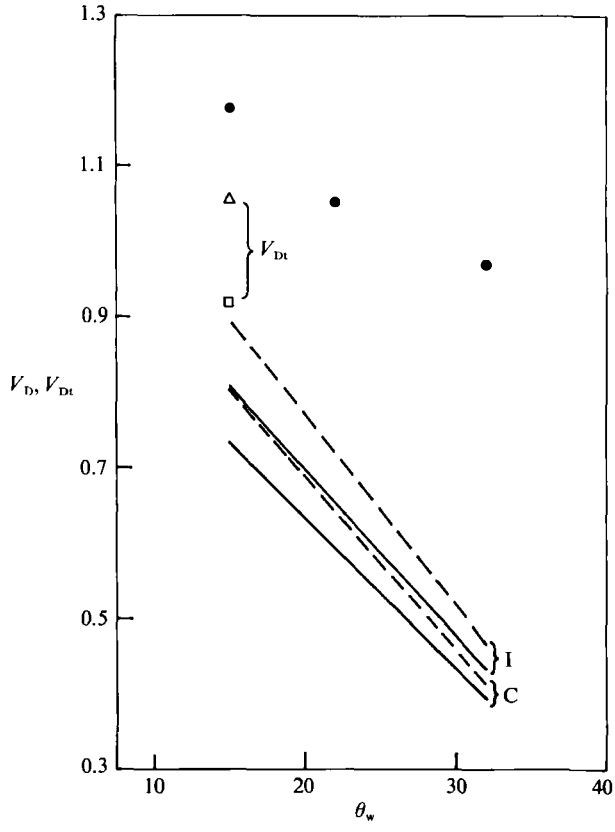

FIGURE 23. Comparison of predicted and measured discharge rates: —— (labelled C), and □, Mohr–Coulomb approximation with ($\Delta t = 2 \times 10^{-4}$, $\Delta\eta = 0.05$) for $\theta_w = 22°$ and $\theta_w = 32°$, and ($\Delta t = 10^{-4}$, $\Delta\eta = 0.05$) for $\theta_w = 15°$; —— (labelled I) and △, incompressible approximation with ($\Delta t = 2.5 \times 10^{-4}$, $\Delta\eta = 0.05$) for all wall angles; ●, experiments of Nguyen *et al.* (1980). All computations are based on asymptotic fields as initial conditions. The broken curves – – – (C) and – – – (I) are the compressible and incompressible discharge rates, respectively, obtained by the approximate analysis. Parameter values: $\Gamma = 1.34$, $\lambda = 0.02$, $n = 1.05$, $\beta^* = 35$, $\xi_e = 0.92$, and $a = 3.96$ for $\theta_w = 15°$; $a = 2.747$ for $\theta_w = 22°$; $a = 1.934$ for $\theta_w = 32°$; $\phi = 31°$, $\delta_h = 15°$.

set, $\beta^* = p_a/(\rho_{max} gL) = 35 (L \approx 0.15$ m), $\Omega = r_w^*/r_e^* = 2L/D = 12 (D \approx 25$ mm), and $\rho_s = 2670$ kg/m^3 (the value reported in Brennen & Pearce (1978) for a sand with similar material properties). The values of L and D are within the range of values used by Nguyen *et al.* (1980). Recently R. H. Sabersky (1989, private communication) has indicated that the experiments were performed with $L = 0.14$ m and D-values in the range 25.4–31.8 mm. Based on earlier results, it is expected that the difference between the parameter values used in the computations and the experiments will not affect the predicted discharge rates significantly.

We are now in a position to compare measured and predicted discharge rates, for both compressible ($\lambda > 0$) and incompressible ($\lambda = 0$) cases. Details of the latter computations are given in §5.4. The predicted compressible discharge rates are shown by the full curve labelled C in figure 23. They are well below the measured values, and the error increases with θ_w, from 38% of the latter at $\theta_w = 15°$ to 59% at $\theta_w = 32°$. It is interesting to note that the incompressible results, shown by the full curve labelled I in figure 23, also underestimate discharge rates. In this case,

however, the error is less – about 31 % to 55 %. This is surprising, as the compressible model is believed to be more realistic, and the density measurements of Bosley *et al.* (1969), Van Zuilichem *et al.* (1974), and Fickie *et al.* (1989) reveal a strong dilation near the exit slot. Perhaps there is some deficiency in the manner in which density variation has been incorporated here.

For a smooth-walled hopper with $\theta_w = 30°$, the exit shock could not be constructed, as mentioned in §5.2.5. The problem disappears when wall roughness is included; the exit shock is then fully realized for all the wall angles considered here, namely $15° \leqslant \theta_w \leqslant 32°$, and its shape is similar to that of the shock down in figure 20.

The broken curve labelled C in figure 23 shows approximate compressible discharge rates, computed using (116)–(120) and (C 10). These are within 9 % of the exact (numerical) values, and have been obtained with far less computational effort. These remarks also apply in the incompressible case, where the difference between approximate and exact values is about 11 %.

When the traction-free surface is used as the exit condition, approximate analyses of the incompressible equations usually overestimate discharge rates for small values of θ_w (Brennen & Pearce 1978; Savage & Sayed 1979; Kaza & Jackson 1982*a*; Meric & Tabarrok 1982). However, the converse is true when the surface of vertical free fall is used as the exit condition (Kaza & Jackson 1982*b*). The full curves in figure 23 are based on the exit shock, and conform to the latter trend. As explained earlier, it is not possible to integrate the equations down to the traction-free surface and check whether the discharge rates are overestimated.

All the same, the equations can be integrated until $\sigma_w^* \equiv \sigma^*(r^*, \theta_w)$ is fairly small – about 0.0194 to 3.96×10^{-3} for $15° \leqslant \theta_w \leqslant 32°$. It is interesting to consider the implications of a hypothetical and arbitrary exit condition

$$\sigma_w^* = 0.0194. \tag{121}$$

In the compressible case, with $\theta_w = 15°$, this condition is satisfied at $r_1^* = 0.294$ and $r_2^* = 0.273$ for the prescribed discharge rates $V_{Da} = 0.801$ and $P_0 V_{Da} = 0.713$, respectively. The discharge rate V_{Dt} corresponding to the exit condition (121), and exit slot radius $r_e^* = 0.322$ (table 3) is then found from V_{Da} and $P_0 V_{Da}$ by linear extrapolation. A similar procedure is also adopted in the incompressible case. The compressible and incompressible values of V_{Dt} so obtained are shown in figure 23 by the square and triangle, respectively. Two features are noteworthy: (i) the discrepancy between theory and experiment is now reduced to about 22 % in the compressible case and about 10 % in the incompressible case, and (ii) the difference in the values of σ_w^* at the edge of the exit slot, as obtained with different exit conditions (91) and (121), is only about 0.044.

The above discussion suggests that the exit condition (91) should be modified, but the form this should take is not clear at the moment. It appears that future attempts to refine discharge rate predictions should concentrate on the region close to the exit slot. It is conceivable that the appropriate equations for this region differ markedly from those used higher up in the bunker.

5.3.5. *Comparison of predicted density profiles with experiments*

In this section, we present a preliminary comparison of the predicted density profiles with the measurements of Fickie *et al.* (1989) for glass beads flowing through a wedge-shaped hopper with $\theta_w = 23°$ and $D = 1.3$ cm. The values of ϕ and δ_h have not been reported in their paper, but R. Jackson (1989, private communication) has indicated that $\phi = 32.4°$, and $\delta_h = 15.1°$.

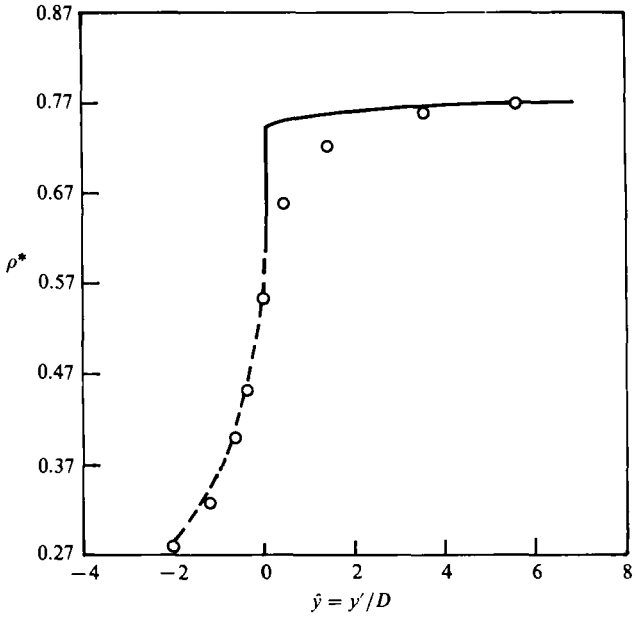

FIGURE 24. Comparison of predicted and measured density profiles along the centreline of a hopper: ——, Mohr–Coulomb approximation with ($\Delta t = 2 \times 10^{-4}$, $\Delta\eta = 0.05$); ○, experiments of Fickie *et al.* (1989). The broken curve represents free fall under zero stresses. Parameter values are: $\Gamma = 1.2$, $\lambda = 0.02$, $n = 1.05$, $\beta^* = 118.6$, $\xi_e = 0.84$, $a = 2.559$, $\phi = 32.4°$, $\delta_h = 15.1°$, $\theta_w = 23°$.

To proceed with the comparison, the initial curve is chosen as a circular arc passing through $r = r_w = 10.4$ cm and $\theta = \theta_w$. This corresponds roughly to the highest level at which the density has been reported. The value of the parameter Γ is chosen by trial and error so that the initial density at $\theta = 0$ is $\rho^* = 0.77$, which is close to the measured value. The procedure described in Appendix C and §5.3.4 is then used to generate the asymptotic fields, and adjust the discharge rate to ensure that the exit shock passes through the edge of the physical exit slot.

The circles in figure 24 show the measured density profile along the centreline of the hopper, while the predicted profile is shown by the full curve. Here $\hat{y} \equiv y'/D$, where y' is the vertical distance measured upwards from the plane of the exit slot. The exit shock intersects the centreline at $\hat{y} = 0.046$, and hence ρ^* jumps from a value of 0.744 above to 0.605 below. The broken curve represents the density profile obtained by assuming free fall under gravity with zero frictional stresses. We note that Fickie *et al.* (1989) have also predicted the density profile below the exit slot using the assumption of free fall. The only difference is that they appear to have used the measured value of the density at the exit plane as the initial density, whereas here the initial condition is obtained as part of the solution of the hopper problem. Within the hopper, there is more dilation than predicted by the model. It remains to be seen whether the use of a larger value of λ will lead to better predictions. Below the hopper, the agreement is fairly good; this is somewhat surprising, and may be a fortuitous occurrence. Alternatively, it is conceivable that the density on the downstream side of the shock is a weak function of conditions on the upstream side.

Figure 25 shows density profiles measured on horizontal planes above and below the plane of the exit slot, and also the corresponding predictions. Within the hopper, the profiles are almost flat, but the measured density is higher at the centreline than

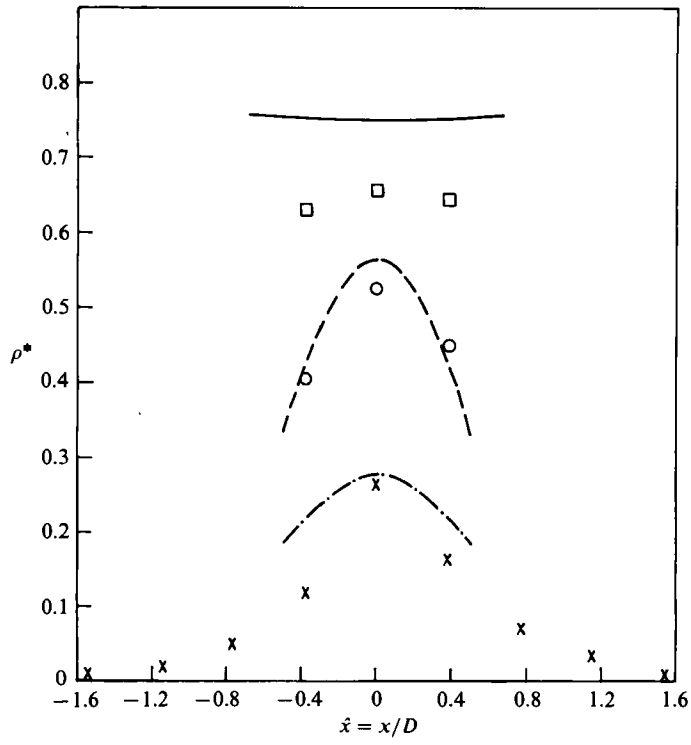

FIGURE 25. Comparison of predicted and measured density profiles on horizontal planes above and below the plane of the exit slot: ——, Mohr–Coulomb approximation with ($\Delta t = 2 \times 10^{-4}$, $\Delta\eta = 0.05$); □, ○, ×, experiments of Fickie *et al.* (1989). The broken curves represent free fall under zero stresses. Parameter values are as in figure 24. ——, □, $\hat{y} = 0.423$; – – –, ○, $\hat{y} = -0.0385$; —·—, ×, $\hat{y} = -2.154$.

at the wall, in contrast to predictions. Below the hopper, there is fair agreement between theory and experiment for $\hat{y} = -0.0385$, and the density is now much higher at the centreline than at the edge of the jet of particles. The crosses in figure 25 show that at a lower value of $\hat{y}(= -2.154)$, the jet has spread laterally. Thus the assumption of vertical fall is not valid here.

5.4. *The incompressible approximation*

If the sizes of the yield loci increase rapidly with increasing density, i.e. if $\partial\tau^*/\partial\rho^* \gg 1$, then a wide range of stresses correspond to a narrow range of densities, and the assumption of incompressible flow may be reasonable (Jackson 1983). It is of interest to compare the incompressible and compressible solutions, so that the importance of density variations may be assessed.

The incompressible equations may be obtained from the compressible equations (23)–(27) by expanding all the field variables in powers of λ, and collecting terms of $O(\lambda^0)$. The latter are given by the continuity equation

$$\frac{\partial v_r^*}{\partial r^*} + \frac{1}{r^*}\frac{\partial v_\theta^*}{\partial \theta} + \frac{v_r^*}{r^*} = 0, \tag{122}$$

the coaxiality condition (26), and the momentum balances (81) and (82). As mentioned earlier, (93) provides the incompressible density $\rho_i^* = 1/\Gamma$, in the limit

$\lambda \to 0$. For an alternative derivation of these equations from the compressible equations, see Jackson (1983). In the limit $\lambda \to 0, \alpha \to 1$, as noted earlier in the subsection on asymptotic fields. Hence the incompressible equations may be regarded as the outcome of the 'critical-state approximation' (Jackson 1983). It should be noted that the momentum balances are identical in form to those of the Mohr–Coulomb approximation.

The incompressible equations have been examined in detail elsewhere (see for example, Jenike 1964*a*; Savage & Yong 1970; Brennen & Pearce 1978; Kaza & Jackson 1982*a*; Meric & Tabarrok 1982). Here we merely note that they have four real and distinct characteristics, and are hyperbolic. In contrast, the basic (compressible) equations (23)–(27) have only three real and distinct characteristics, and are not hyperbolic. Further, these characteristics do not go over smoothly to those of the incompressible equations as $\lambda \to 0$. These two features of the basic equations, which appear to be unsatisfactory, may be eliminated by using MCA equations (23), (26), (27), (81) and (82).

Numerical integration of the MCA, with $\theta_w = 32°$, $\beta^* = 35.0$, and the asymptotic fields as the initial condition leads to a discharge rate $V_D = 0.382$, and a reciprocal exit slot radius $\bar{\beta} = 227.3$. For the same values of θ_w, β^* and $\bar{\beta}$, numerical integration of the incompressible approximation with the radial stress and velocity fields as initial conditions leads to a discharge rate $V_D = 0.422$. Thus the incompressible approximation overestimates the discharge rate by 10%. Figure 23 shows that, at other values of θ_w also, discharge rates are overestimated by roughly the same amount. Similarly, for $\theta_w = 32°$, the incompressible approximation overestimates the mean stress by 5–10%.

6. Discussion

Continuum models have been used here to predict the stress, density, and velocity fields in wedge-shaped bunkers. The principal results obtained, and the limitations of this work are summarized below with reference to

(i) The transition region between the bin and hopper sections,
(ii) the hopper section,
(iii) the exit region,
(iv) discharge rates,
(v) density profiles, and
(vi) the incompressible approximation.

6.1. *The transition region*

This has been idealized as a single rupture layer or shock across which the density decreases, the state of stress switches from active above to passive below, and the velocity vector from vertical above to radial below. Because the flow rule and the coaxiality conditions are not in conservation-law form, the jump balances have been supplemented by additional assumptions. The predicted shape of the shock differs markedly from that observed by Michalowski (1987), particularly near the centreline (figure 4). It appears that the use of a single rupture layer is not justified in this region.

At the bin–hopper transition, the ratio of the normal stress on the bin wall to that on the hopper wall, N_h/N_b, is found to be a strong function of the parameter n, which determines the slope of the yield locus (table 2). With n close to 1, the value of N_h/N_b lies in the range of measured values.

6.2. *The hopper section*

While it is well known that the incompressible equations are hyperbolic, the nature of the compressible equations does not appear to have been examined in literature. Here it is shown that the basic equations are not hyperbolic, even though they have real characteristics. This stems from the use of an associated flow rule; it is shown in §5.2.2 that hyperbolicity may be restored by using a non-associated flow rule. More experimental data are needed to choose between these two types of flow rules.

Though the basic equations are not hyperbolic, they may, in a certain sense, be split into two systems of hyperbolic equations as explained in §2.5. However, the computational time is large, owing to the large magnitude of the term $\partial\tau^*/\partial\rho^*$, which occurs in the compatibility condition (74).

The above problem is alleviated by noting that the material remains close to the critical state $\alpha = 1$ over most of the hopper section. In the limit $\alpha \to 1$, the yield condition (28) reduces to the Mohr–Coulomb yield condition (51). Using the latter as the yield condition, but retaining (28) as the plastic potential, we obtain the governing equations of the Mohr–Coulomb approximation (MCA). These may be regarded as representing a material with a non-associated flow rule. Unlike the basic equations, they are strictly hyperbolic, and yield comparable results (figures 10–12, and 15–19) with much lower computational times. Further, the characteristics of the MCA equations go over smoothly to those of the incompressible equations in the limit $\lambda \to 0$, again unlike the basic equations.

A perturbation method has been used to derive expressions for the asymptotic stress, density, and velocity fields. Figures 10, 21, 12, 17 and 16 demonstrate convergence of the actual σ^*, ρ^*, and γ-fields to the asymptotic fields as ξ increases. In contrast, the γ-field for a smooth-walled hopper (figure 11) does not converge to the asymptotic γ-field. As indicated in §5.3.2, there is reason to believe that the radial stress field is unstable to perturbations, for the parameter values used here. The asymptotic velocity field is found to be radial to $O(\lambda)$, and the profile of v_θ^* (figure 18) does show a tendency to approach the asymptotic value $v_\theta^* \approx 0$ as ξ increases. The profile of v_r^* remains close to the asymptotic field (figure 19); however, this cannot be regarded as evidence of convergence, since the initial values at $\xi = 0$ do not differ appreciably. Close to the exit slot, growing inertial terms cause the profiles of all the variables to deviate from the asymptotic fields.

While attempting to integrate the MCA equations downwards from the entry shock, computational difficulties were encountered for $\theta_w \geqslant 15°$. These arise because the C_4 characteristics become nearly parallel to the η-axis, and appear to converge, suggesting the formation of a shock. The difficulty is overcome here by abandoning the initial conditions based on the entry shock, and using alternative initial conditions based on the asymptotic fields (Appendix C, §C.2). This ensures that the MCA equations can be integrated downwards in all the cases examined. Of course, the original problem remains unsolved. It is not clear at present whether the behaviour exhibited by the profiles in figure 22 is genuine, or is a reflection of some unnatural assumptions made while constructing the entry shock. This cannot be ascertained since stress measurements in the interior of bunkers are as yet unavailable.

6.3. *The exit region*

Most analyses of hopper flow have assumed that the hopper ends at a traction-free surface $\sigma^* = 0$, which spans the exit slot. As noted by Kaza & Jackson (1982*a*), it is difficult to approach this surface from above, owing to a singularity in the

momentum balances. Further, with the assumption of incompressible flow in the hopper, use of this exit condition leads to an unrealistic compaction of material on the downstream side of the traction-free surface (Kaza & Jackson 1982*b*). For the special case of the smooth-wall, radial gravity problem, it can be shown that this conclusion is unaffected by the inclusion of density variation. Hence an alternative exit condition, suggested by Kaza & Jackson (1982*b*) is used here. This assumes that the exit slot is spanned by a shock, below which the material falls vertically with zero frictional stresses. As these conditions are insufficient to determine the bin velocity u uniquely, the following additional constraint is imposed in the present work. It is assumed that at the edge of the exit slot, the shock is tangential to the characteristic which determines the domain of determinacy of the exit slot (figure 5). As discussed in §3.6, this prescription determines an upper bound on u for a given exit slot width, and, for the parameter values used here, ensures that the shock lies within the domain of determinacy of the exit slot everywhere (figure 20).

Clearly, the condition described above for locating the exit shock along the wall has no physical basis. Further, the following problems have been encountered while using this condition. For any chosen values of the angle of internal friction ϕ and the angle of wall friction δ, there exists a critical wall angle θ_{wc}, such that the exit shock cannot be constructed for $\theta_w > \theta_{wc}$ (see Prakash 1989). If $\theta_w < \theta_{wc}$, it may be possible to construct the shock, as in the case of a rough-walled hopper (§5.3.1). However, for a smooth-walled hopper with $\theta_w = 30°$, and gravity directed radially towards its vertex, the shock issuing from the edge of the exit slot descends steeply and intersects the traction-free surface before reaching the centreline. Thus the shock cannot be fully realized in this case, even though $\theta_w < \theta_{wc}$.

The *ad hoc* nature of the exit condition, and the problems associated with it, represent the major shortcoming of the present work. It is hoped that future work will focus on the specification of more realistic exit conditions.

6.4. *Discharge rates*

For a rough-walled bunker, discharge rates have been compared with the measurements of Nguyen *et al.* (1980). In the compressible case, predicted values are well below measurements – the error varies from 38% (of the measured value) at $\theta_w = 15°$ to 59% at $\theta_w = 32°$ (figure 23). Note that these figures are based on the use of a shock as the exit condition. For illustrative purposes, an alternative exit condition $\sigma^* = 0.0194$ has also been used here. The alternative condition leads to discharge rates that are within 22% of the measured value. Thus the discharge rate is sensitive to the exit condition used but, unfortunately, a satisfactory condition is lacking. It should be emphasized that other aspects of the theory, such as the treatment of the transition region, and the qualitative behaviour of solutions in the hopper section, are unaffected by the choice of the exit condition.

The asymptotic fields can be used to obtain an approximate semi-analytical expression for the discharge rate, as explained in §5.3.4. Compared to the integration of the MCA equations, the computational effort required is trivial. Further, the difference between approximate and exact (numerical) discharge rates is only about 9% (figure 23).

6.5. *Density profiles*

Comparison with the measurements of Fickie *et al.* (1989) shows that for the parameter values used here, the density profile along the centreline of the hopper is qualitatively similar to that observed, but the latter varies more strongly near the exit slot (figure 24). However, just below the exit slot there is good agreement

between the two, and the error is less than 8% (figure 25). The error increases on moving downwards, presumably due to the lateral spreading of the particle jet. Since the measurements show a smooth density variation across the plane of the exit slot, the exit shock is not realized in practice, but its use permits prediction of some of the observed features.

6.6. *The incompressible approximation*

The incompressible equations are shown to be a special case of the basic equations, obtainable from the latter in the limit $\lambda \to 0$. Results obtained with the compressible (MCA) and incompressible equations are qualitatively similar, but the computational time is shorter in the latter case. For example, with the asymptotic fields as the initial conditions, $\theta_w = 32°$, and parameter values as in figure 23, integration of the MCA requires 26 min while the incompressible approximation requires 16 min.

The difference between incompressible and compressible discharge rates, expressed as a percentage of the latter, is about 10% (figure 23). These results have been obtained for a material with $\lambda = 0.02$; it is likely that the difference will increase with λ. As shown in figure 23, the incompressible values are closer to the measurements than the compressible values. This is a paradoxical result, as there is strong experimental evidence of dilation near the exit slot, suggesting that a compressible model should be more realistic. Therefore, it may be necessary to modify the manner in which density variation has been incorporated in the present work, and perhaps, also the exit condition.

The approximate analysis referred to above predicts incompressible discharge rates that are within 11% of exact (numerical) values. Further, it suggests that inclusion of density variation causes a reduction in the discharge rate, and this is borne out by the results shown in figure 23.

We are grateful to Professors Renuka Ravindran and Phoolan Prasad for helpful suggestions regarding numerical computations, and to Professor Roy Jackson for sending us a copy of the article by Fickie *et al.* (1989) prior to publication.

Appendix A.† The asymptotic stress field in the bin

Appendix B.† Evaluation of the parameter n

Appendix C. Asymptotic fields

C. 1. *Governing equations for the asymptotic fields*

The momentum balances (106) and (107) admit a solution of the form (112) for σ^*_{c1} and for γ_1. On substituting (112) into (106) and (107), we get two groups of terms: (*a*) one involving functions of θ, and (*b*) one involving functions of θ multiplied by $\ln r^*$. Setting each group of terms to zero leads to ordinary differential equations for b_{11}, g_{11}, b_{12}, and g_{12}. Similarly, the condition of coaxiality and the equation of continuity lead to ordinary differential equations for w_{11} and w_{12}.

Boundary conditions for these equations may be specified as follows. The wall friction condition (44) is expanded in powers of λ to get

$$g_{11}(\theta_w) = \frac{\alpha_1(\theta_w)\sin 2\gamma_{0w}}{2(\sin\phi + \cos 2\gamma_{0w})}; \quad g_{12}(\theta_w) = 0. \tag{C 1a, b}$$

At the centreline, the condition of symmetry implies

$$g_{11}(0) = 0; \quad g_{12}(0) = 0. \tag{C 2}$$

† Copies are available on request either from the editor or from the authors.

Similarly, (113) and (114) imply

$$h(\theta_w) = \int_0^{\theta_w} (\rho_0^* w_0 + w_{12})\, d\theta = 0. \tag{C 3}$$

It is found that the above equations admit an exact solution of the form

$$b_{12} = \rho_0^* b_0; \quad g_{12} = 0; \quad w_{12} = -\rho_0^* w_0. \tag{C 4}$$

The remaining differential equations for b_{11}, g_{11}, and w_{11}, together with the equation for w_0, may be integrated subject to boundary conditions given by (C 1a) and (C 2), and specified values of two constants P_1 and P_2, where

$$P_1 \equiv w_0(\theta_w); \quad P_2 \equiv w_{11}(\theta_w). \tag{C 5}$$

As mentioned in §5.3.2, we estimate P_1 and P_2 approximately by using the exit condition. Details are given below.

Consider the following procedure. The field variables may be expanded in powers of λ, as in (94), and substituted into the basic equations (23)–(27). Setting terms of $O(\lambda^0)$ and of $O(\lambda^1)$ to zero results in two sets of equations. Initial conditions along the entry shock, or for that matter along any smooth curve which is not too close to the hopper exit, are needed to integrate these equations. Here these initial conditions may be taken to be given by the asymptotic fields, generated as described above (see also §C. 2).

The equations of $O(\lambda^0)$ and $O(\lambda^1)$ may then be integrated downwards to obtain $v_{r0}^*(r^*, \theta)$, $v_{r1}^*(r^*, \theta)$ etc. Substituting these functions into the exit condition (91) gives

$$O(\lambda^0): \qquad \frac{\rho_0^*(v_{r0}^*)^2}{\sigma_0^*} - \frac{\{\tan[(\frac{1}{4}\pi - \frac{1}{2}\phi) - \gamma_w] - b_1\}}{a_1} = 0, \tag{C 6}$$

$$O(\lambda^1): \qquad \rho_1^* \sigma_0^* v_{r0}^* + 2\sigma_0^* \rho_0^* v_{r1}^* - \rho_0^* v_{r0}^* \sigma_1^* = 0, \tag{C 7}$$

where a_1 and b_1 are defined by (92), and all the functions are evaluated at the edge of the exit slot ($r^* = r_e^*, \theta = \theta_w$). At this point, $v_{r0}^* = v_{r0}^*(P_1)$, $v_{r1}^* = v_{r1}^*(P_1, P_2)$, and so on. Since the values of P_1 and P_2 have been chosen arbitrarily, (C 6) and (C 7) will not be satisfied in general. Hence these values must be changed, and the above procedure repeated until (C 6) and (C 7) hold to within a prescribed tolerance.

This method is extremely tedious in practice, since an analytical solution is not available even for the equations of $O(\lambda^0)$. Hence the following alternative method is used to estimate the values of P_1 and P_2. Using the Mohr–Coulomb yield condition (51), the asymptotic fields correct to $O(\lambda^1)$ for ρ^*, v_r^* and v_θ^*, and to $O(\lambda^0)$ for $\partial\gamma/\partial\theta$ and $\partial\sigma/\partial\theta$, the r-component of the momentum balance, (24), may be integrated to obtain an analytical expression for $\sigma_w^* \equiv \sigma(r^*, \theta_w)$, as discussed in §C. 3 below. This takes the form

$$\sigma_w^* = \sigma_{w0}^*(r^*, \theta_w; P_1) + \lambda \sigma_{w1}^*(r^*, \theta_w; P_1, P_2) \tag{C 8}$$

where functions σ_{w0}^* and σ_{w1}^* are given by (C 20). Equations (C 5) imply

$$v_{r0}^*(r_e^*, \theta_w) = \frac{P_1}{r_e^*}; \quad v_{r1}^*(r_e^*, \theta_w) = \frac{P_2}{r_e^*} - \left(\frac{\rho_0^* P_1 \ln r_e^*}{r_e^*}\right). \tag{C 9}$$

Replacing σ_0^* and σ_1^* in (C 6) and (C 7) by σ_{w0}^* and σ_{w1}^*, respectively, ρ_0^* and ρ_1^* by (100) and (110), respectively, and using (C 9), we get

$$w_0(\theta_w) \equiv P_1 = k_1 (r_e^*)^{\frac{3}{2}};$$

$$w_{11}(\theta_w) \equiv P_2 = P_1\left[\left\{\frac{\rho_{12}(A_1 - A_2 k_1^2) + \rho_0^*(A_5 + A_4 k_1^2)}{2\rho_0^* A_1}\right\} \ln r_e^* - \left\{\frac{\rho_{11}(A_1 - A_2 k_1^2) - \rho_0^*(A_6 - A_3 k_1^2)}{2\rho_0^* A_1}\right\}\right], \quad \text{(C 10)}$$

where

$$k_1 = -\left\{\frac{A_1[\tan(\tfrac{1}{4}\pi - \tfrac{1}{2}\phi - \gamma_w) - b_1]}{a_1\rho_0^* + A_2[\tan(\tfrac{1}{4}\pi - \tfrac{1}{2}\phi - \gamma_w) - b_1]}\right\}^{\frac{1}{2}}, \quad \text{(C 11)}$$

and the constants $A_1 - A_6$ are given by (C 21). The values of P_1 and P_2 obtained from (C 10) are not exact, since several simplifying assumptions have been used in deriving (C 8)–(C 11).

Using the boundary conditions (C 1), (C 2), and (C 10), the relevant differential equations are integrated numerically using the ST1FF3 routine (Villadsen & Michelsen 1978, pp. 321–323) to obtain $b_{11}(\theta)$, $g_{11}(\theta)$, $w_0(\theta)$ and $w_{11}(\theta)$. This completes the determination of the asymptotic fields.

C.2. Initial conditions

In this section, we construct initial conditions based on the asymptotic fields, and compare them with those obtained earlier using the entry shock.

The initial radial velocity v_r^*, along any smooth curve is obtained by using (C 15*b*), where $w_0(\theta)$ and $w_{11}(\theta)$ are estimated by the procedure described in §C. 1 above.

Regarding the initial stress and density profiles, it turns out that for typical parameter values, the asymptotic fields imply $\alpha(r_w^*, \theta_w) > 1$ when the expansions $\rho^* = \rho_0^* + \lambda\rho_1^*$ and $\sigma^* = \sigma_0^* + \lambda\sigma_1^*$ are used in (29). For example, with the parameter values reported by Nguyen *et al.* (1980), $\alpha(r_w^*, \theta_w) = 1.104$. As discussed in §3.4, this value is greater than the maximum permissible value $\alpha_{max} = 1.054$. The difficulty is circumvented by using the asymptotic fields for σ_c^* ((102) and (112)) and α ((101) and (109)), and evaluating the initial stress and density profiles from

$$\sigma^* = (\alpha_0 + \lambda\alpha_1)(\sigma_{c0}^* + \lambda\sigma_{c1}^*); \quad \rho^* = \frac{1}{\left[\Gamma - \lambda \ln\left(\frac{\sigma_{c0}^* + \lambda\sigma_{c1}^*}{\beta^*}\right)\right]}. \quad \text{(C 12)}$$

Since the numerical integration is based on the MCA equations, the actual value of $\gamma(r_w^*, \theta_w)$ is replaced by $\gamma_{0w}\,(= g_0(\theta_w))$. This is reasonable since the difference in values is $< 0.2\,\%$.

In the present work, the values along the entry shock of the various fields discussed above are used as the initial conditions. When these are compared with the initial conditions based on the entry shock, the profiles of v_r^* and γ are found to be qualitatively similar, while those of σ^* and ρ^* exhibit marked differences. For example, in the former case, σ^* increases from 1.2 at $\theta = 0$ to 1.6 at $\theta = \theta_w = 15°$, whereas in the latter case, it decreases from 21.2 at $\theta = 0$ to 15.0 at θ_w. (These results are based on the parameter values listed in the caption of figure 23.) Perhaps this difference in initial conditions is responsible for the two types of behaviour exhibited by the solutions of the MCA equations. When the asymptotic fields are used as initial conditions, the γ-profiles remain monotonic and the integration proceeds without undue difficulty. In contrast, when the entry shock is used to generate initial conditions, the γ-profiles quickly become non-monotonic and exhibit steep fronts (figure 22). This makes it difficult to integrate the governing equations, as discussed in §5.3.3.

C.3. An approximation for the stress along the wall

The results of numerical integration of the basic equations indicate that the following features are approximately true of the solution deep in the hopper section of a steep-walled bunker:

$$\gamma = \gamma(\theta); \quad v_\theta^* = 0; \quad \tau^* = \sigma^* \sin\phi. \tag{C 13}$$

By incorporating these observations and appropriate asymptotic fields into the momentum balance (24), it is possible to obtain an estimate for the mean stress along the wall $\sigma_w^* \equiv \sigma^*(r^*, \theta_w)$, as described below. In the incompressible case, Williams (1977) has used (C 13) and other assumptions to obtain upper and lower bounds on discharge rates from conical hoppers.

Substituting (C 13) into the r-component of the momentum balance, we get

$$[1-\sin\phi\cos 2\gamma]\frac{\partial\sigma^*}{\partial r^*} - \left[\frac{2\sin\phi\cos 2\gamma}{r^*}\left(1+\frac{\partial\gamma}{\partial\theta}\right)\right]\sigma^* = \frac{\sin\phi\sin 2\gamma}{r^*}\frac{\partial\sigma^*}{\partial\theta} - \rho^* v_r^* \frac{\partial v_r^*}{\partial r^*} - \rho^* \cos\theta. \tag{C 14}$$

The functions ρ^*, v_r^*, $\partial\sigma^*/\partial\theta$ and $\partial\gamma/\partial\theta$ in (C 14) are approximated by using the asymptotic fields, as follows:

$$\rho^* = \rho_0^* + (\rho_{11}(\theta) + \rho_{12}\ln r^*)\lambda; \tag{C 15a}$$

$$v_r^* = \frac{w_0(\theta)}{r^*} + \left(\frac{w_{11}(\theta)}{r^*} + \frac{w_{12}(\theta)}{r^*}\ln r^*\right)\lambda; \tag{C 15b}$$

$$\frac{\partial\sigma^*}{\partial\theta} = r^*\frac{\mathrm{d}b_0}{\mathrm{d}\theta}; \quad \frac{\partial\gamma}{\partial\theta} = \frac{\mathrm{d}g_0}{\mathrm{d}\theta}, \tag{C 15c, d}$$

where b_0 and g_0 are obtained from the radial stress field (Jenike 1964*b*). To simplify the analysis, we have used asymptotic fields correct to $O(\lambda^0)$ for $\partial\sigma^*/\partial\theta$ and $\partial\gamma/\partial\theta$. Computations indicate that this assumption is reasonable, except close to the exit slot (Prakash 1989). Though the error involved in the approximations increases with ξ, the magnitudes of $\partial\sigma^*/\partial\theta$ and σ^* decrease. Hence the error introduced into the solution of (C 14) may be less than expected.

Substituting (C 15) into (C 14), and setting $\theta = \theta_w$, we get a linear ordinary differential equation for $\sigma_w^* \equiv \sigma^*(r^*, \theta_w)$:

$$\frac{\mathrm{d}\sigma_w^*}{\mathrm{d}r^*} - \left(\frac{k}{r^*}\right)\sigma_w^* = q(r^*), \tag{C 16}$$

where

$$k = \frac{2\sin\phi\cos 2\gamma_w(1+\mathrm{d}g_0/\mathrm{d}\theta)}{(1-\sin\phi\cos 2\gamma_w)} \tag{C 17}$$

and

$$q(r^*) = \frac{1}{(1-\sin\phi\sin 2\gamma_w)}\left[\frac{\mathrm{d}b_0}{\mathrm{d}\theta}\sin\phi\sin 2\gamma_w - \rho_0^*\cos\theta_w + \frac{\rho_0^* P_1^2}{(r^*)^3} - \lambda\left\{\frac{\rho_{12}P_1^2}{(r^*)^3}\ln r^* - \frac{1}{(r^*)^3}[2\rho_0^* P_1 P_2 + (\rho_{11}+\rho_{12})P_1^2] + \rho_{11}\cos\theta_w + \rho_{12}\cos\theta_w \ln r^*\right\}\right]. \tag{C 18}$$

Equation (C 16) may be integrated to get

$$\sigma_w^* = \sigma_{w0}^* + \lambda \sigma_{w1}^*, \tag{C 19}$$

where

$$\sigma_{w0}^* = A_1 r^* - \frac{A_2 P_1^2}{(r^*)^2};$$

$$\sigma_{w1}^* = -\frac{A_3 P_1^2}{(r^*)^2} - \frac{2A_2 P_1 P_2}{(r^*)^2} + \frac{A_4 P_1^2 \ln r^*}{(r^*)^2} + A_5 r^* \ln r^* + A_6 r^*. \tag{C 20}$$

Here,

$$A_1 = \frac{\rho_0^* \cos\theta_w - (\mathrm{d}b_0/\mathrm{d}\theta)\sin\phi \sin 2\gamma_w}{(1-\sin\phi\cos 2\gamma_w)(k-1)}; \quad A_2 = \frac{\rho_0^*}{(1-\sin\phi\cos 2\gamma_w)(k+2)};$$

$$A_3 = \frac{(\rho_{11}+\rho_{12})(k+2)-\rho_{12}}{(1-\sin\phi\cos 2\gamma_w)(k+2)^2}; \quad A_4 = \frac{\rho_{12}}{(1-\sin\phi\cos 2\gamma_w)(k+2)}; \tag{C 21}$$

$$A_5 = \frac{\rho_{12}\cos\theta_w}{(1-\sin\phi\cos 2\gamma_w)(k-1)}; \quad A_6 = \frac{(\rho_{11}(k-1)+\rho_{12})\cos\theta_w}{(1-\sin\phi\cos 2\gamma_w)(k-1)^2}.$$

The integration constant has been dropped in (C 19) since the solution is assumed to be independent of initial conditions.

REFERENCES

Ackermann, N. L. & Shen, H. 1982 Stresses in rapidly sheared fluid-solid mixtures. *J. Engng Mech. Div. ASCE* **108**, 95–113.

Airey, D. W., Budhu, M. & Wood, D. M. 1985 Some aspects of the behaviour of soils in simple shear. In *Developments in Soil Mechanics and Foundation Engineering–2* (ed. P. K. Bannerjee & R. Butterfield), pp. 185–213. Elsevier.

Atkinson, J. H. & Bransby, P. L. 1978 *The Mechanics of Soils*. McGraw-Hill.

Bagnold, R. A. 1954 Experiments on a gravity-free dispersion of large solid spheres in a Newtonian fluid under shear. *Proc. R. Soc. Lond.* A **225**, 49–63.

Blair-Fish, P. M. & Bransby, P. L. 1973 Flow patterns and wall stresses in a mass flow bunker. *Trans. ASME* B: *J. Engng Ind.* **95**, 17–26.

Blight, G. E. 1986 Pressures exerted by materials in silos: Part I, coarse materials. *Geotech.* **36**, 33–46.

Bolton, M. D. 1986 The strength and dilatancy of sands. *Geotech.* **36**, 65–78.

Bosley, J., Schofield, C. & Shook, C. A. 1969 An experimental study of granule discharge from model hoppers. *Trans. Inst. Chem. Engrs* **47**, 147–153.

Bransby, P. L. & Blair-Fish, P. M. 1974 Wall stresses in mass flow bunkers. *Chem. Engng Sci.* **29**, 1061–1074.

Bransby, P. L. & Blair-Fish, P. M. 1975 Deformations near rupture surfaces in flowing sand. *Geotech.* **25**, 384–389.

Brennen, C. & Pearce, J. C. 1978 Granular material flow in two-dimensional hoppers. *Trans. ASME* E: *J. Appl. Mech.* **45**, 43–50.

Bridgwater, J. & Scott, A. M. 1983 Flow of solids in bunkers. In *Handbook of Fluids in Motion* (ed. N. P. Chemeserinoff & R. Gupta), pp. 807–846. Butterworths.

Brown, R. L. & Richards, J. C. 1970 *Principles of Powder Mechanics*. Pergamon.

Campbell, C. S. & Brennen, C. E. 1985 Chute flows of granular materials: some computer simulations. *Trans. ASME* E: *J. Appl. Mech.* **52**, 172–178.

Cole, E. R. L. 1967 The behaviour of soils in the simple shear apparatus. Ph.D. thesis, University of Cambridge.

Courant, R. & Hilbert, D. 1962 *Methods of Mathematical Physics*, Vol. 2. Interscience.

DAVIDSON, J. F. & NEDDERMAN, R. M. 1973 The hour-glass theory of hopper flow. *Trans. Inst. Chem. Engrs* **51**, 29–35.

DESAI, C. S. & SIRIWARDANE, H. J. 1984 *Constitutive Laws for Engineering Materials*. Prentice-Hall.

DRESCHER, A., COUSENS, T. W. & BRANSBY, P. L. 1978 Kinematics of the mass flow of granular material through a plane hopper. *Geotech.* **28**, 27–42.

DRUCKER, D. C. & PRAGER, W. 1952 Soil mechanics and plastic analysis or limit design. *Q. Appl. Maths* **10**, 157–165.

ENSTAD, G. 1975 On the theory of arching in mass flow hoppers. *Chem. Engng Sci.* **30**, 1273–1283.

FICKIE, K. E., MEHRABI, R. & JACKSON, R. 1989 Density variations in a granular material flowing from a wedge-shaped hopper. *AIChE J.* **35**, 853–855.

GEROGIANNOPOULOS, N. G. & BROWN, E. T. 1978 The critical state concept applied to rock. *Intl J. Rock Mech. Min. Sci.* (& *Geomech. Abstr.*) **15**, 1–10.

HANDLEY, M. F. & PERRY, M. G. 1967 Stresses in granular materials flowing in converging hopper sections. *Powder Technol.* **1**, 245–251.

HILL, R. 1950 *The Mathematical Theory of Plasticity*. Clarendon.

HORNE, R. M. & NEDDERMAN, R. M. 1978 An analysis of switch stresses in two-dimensional bunkers. *Powder Technol.* **19**, 235–241.

HUNTER, S. C. 1983 *Mechanics of Continuous Media*, 2nd edn. Ellis Horwood.

JACKSON, R. 1983 Some mathematical and physical aspects of continuum models for the motion of granular materials. In *Theory of Dispersed Multiphase Flow* (ed. R. E. Meyer), pp. 291–337. Academic.

JACKSON, R. 1986 Some features of the flow of granular materials and aerated granular materials. *J. Rheol.* **30**, 907–930.

JENIKE, A. W. 1964*a* *Storage and Flow of Solids*. Bulletin 123, Univ. Utah Engng Expt. Station.

JENIKE, A. W. 1964*b* Steady gravity flow of frictional cohesive solids in converging channels. *Trans. ASME* E: *J. Appl. Mech.* **31**, 5–11.

JENIKE, A. W. 1965 Gravity flow of frictional cohesive solids – convergence to radial stress fields. *Trans. ASME* E: *J. Appl. Mech.* **32**, 205–207.

JENIKE, A. W. 1987 A theory of flow of particulate solids in converging and diverging channels based on a conical yield function. *Powder Technol.* **50**, 229–236.

JENIKE, A. W. & JOHANSON, J. R. 1968 Bin loads. *J. Struct. Div. ASCE* **94**, 1011–1041.

JOHANSON, J. R. 1964 Stress and velocity fields in the gravity flow of bulk solids. *Trans. ASME* E: *J. Appl. Mech.* **31**, 499–506.

JOHNSON, P. C. & JACKSON, R. 1987 Frictional–collisional constitutive relations for granular materials, with application to plane shearing. *J. Fluid Mech.* **176**, 67–93.

KAZA, K. R. 1982 The mechanics of flowing granular materials. Ph.D. thesis, University of Houston.

KAZA, K. R. & JACKSON, R. 1982*a* The rate of discharge of coarse granular material from a wedge-shaped mass flow hopper. *Powder Technol.* **33**, 223–237.

KAZA, K. R. & JACKSON, R. 1982*b* A problem in the flow of granular materials. *Proc. 9th US Natl Congress on Applied Mechanics.*

KAZA, K. R. & JACKSON, R. 1984 Boundary conditions for a granular material flowing out of a hopper or bin. *Chem. Engng Sci.* **39**, 915–916.

LADE, P. V. & DUNCAN, J. M. 1975 Elastoplastic stress–strain theory for cohesionless soil. *J. Geotech. Engng Div. ASCE* **101**, 1037–1053.

LEE, J., COWIN, S. C. & TEMPLETON, J. S. 1974 An experimental study of the kinematics of flow through hoppers. *Trans. Soc. Rheol.* **18**, 247–269.

MANJUNATH, K. S. 1988 Silo/feeder interfacing. *Rep.* CMI No. 88/03150-1, Chr. Michelsen Institute, Bergen.

MARCHELLO, J. M. 1976 In *Gas–Solids Handling in the Process Industries* (ed. J. M. Marchello & A. Gomezplata), pp. 1–12. Marcel Dekker.

MERIC, R. A. & TABARROK, B. 1982 On the gravity flow of granular materials. *Intl J. Mech. Sci.* **24**, 469–478.

MICHALOWSKI, R. L. 1984 Flow of granular material through a plane hopper. *Powder Technol.* **39**, 29–40.

MICHALOWSKI, R. L. 1987 Flow of granular media through a plane parallel/converging bunker. *Chem. Engng Sci.* **42**, 2587–2596.

MROZ, Z. & SZYMANSKI, C. 1978 Non-associated flow rules in description of plastic flow of granular materials. In *Limit Analysis and Rheological Approach in Soil Mechanics* (ed. W. Olszak & L. Suklje), pp. 51–94. Springer.

NAYLOR, D. J. 1978 Stress–strain laws for soil. In *Developments in Soil Mechanics* (ed. C. R. Scott), Vol. 1, pp. 39–68. Applied Science Publishers.

NEDDERMAN, R. M. 1988 The measurement of the velocity profile in a granular material discharging from a conical hopper. *Chem. Engng Sci.* **43**, 1507–1516.

NEDDERMAN, R. M. & LAOHAKUL, C. 1980 The thickness of the shear zone of flowing granular materials. *Powder Technol.* **25**, 91–100.

NGUYEN, T. V., BRENNEN, C. E. & SABERSKY, R. H. 1980 Funnel flow in hoppers. *Trans. ASME* E: *J. Appl. Mech.* **47**, 729–735.

PERRY, M. G. & HANDLEY, M. F. 1967 The dynamic arch in free flowing granular material discharging from a model hopper. *Trans. Inst. Chem. Engrs* **45**, 367–371.

PITMAN, E. B. 1986 Stress and velocity fields in two- and three-dimensional hoppers. *Powder Technol.* **47**, 219–231.

PRAKASH, J. R. 1989 Steady compressible plane flow of cohesionless granular materials in hoppers and bunkers. Ph.D. thesis, Indian Institute of Science.

PRAKASH, J. R. & RAO, K. K. 1988 Steady compressible flow of granular materials through a wedge-shaped hopper; the smooth wall, radial gravity problem. *Chem. Engng Sci.* **43**, 479–494.

PRASAD, P. & RAVINDRAN, R. 1985 *Partial Differential Equations.* Wiley Eastern.

RAO, L. & VENKATESWARLU, D. 1974 Static and dynamic wall pressures in experimental mass flow hoppers. *Powder Technol.* **10**, 143–152.

ROSCOE, K. H. 1970 The influence of strains in soil mechanics. *Geotech.* **20**, 129–170.

ROSCOE, K. H. & BURLAND, J. B. 1968 On the generalized stress–strain behaviour of wet clay. In *Engineering Plasticity* (ed. J. Heyman & R. A. Leckie), pp. 535–609. Cambridge University Press.

ROSCOE, K. H., SCHOFIELD, A. N. & WROTH, C. P. 1958 On the yielding of soils. *Geotech.* **8**, 22–53.

SAVAGE, S. B. 1965 The mass flow of granular material derived from coupled velocity–stress fields. *Brit. J. Appl. Phys.* **16**, 1885–1888.

SAVAGE, S. B. 1983 Granular flows at high shear rates. In *Theory of Dispersed Multiphase Flow* (ed. R. E. Meyer), pp. 339–358. Academic.

SAVAGE, S. B., NEDDERMAN, R. M., TÜZÜN, U. & HOULSBY, G. T. 1983 The flow of granular materials – III. *Chem. Engng Sci.* **38**, 189–195.

SAVAGE, S. B. & SAYED, M. 1979 Gravity flow of cohesionless granular materials in wedge shaped hoppers. In *Mechanics Applied to the Transport of Bulk Materials* (ed. S. C. Cowin), pp. 1–24. ASME.

SAVAGE, S. B. & YONG, R. N. 1970 Stresses developed by cohesionless granular materials in bins. *Intl J. Mech. Sci.* **12**, 675–693.

SAYED, M. & SAVAGE, S. B. 1983 Rapid gravity flow of cohesionless granular materials down inclined chutes. *Z. Angew Math. Phys.* **34**, 84–99.

SCHAEFFER, D. G. & PITMAN, E. B. 1988 Ill-posedness in three-dimensional plastic flow. *Commun. Pure Appl. Maths* **41**, 879–890.

SCHOFIELD, A. N. & WROTH, C. P. 1968 *Critical State Soil Mechanics.* McGraw-Hill.

SHAMLOU, P. A. 1988 *Handling of Bulk Solids.* Butterworths.

SHIELD, R. T. 1953 Mixed boundary value problems in soil mechanics. *Q. Appl. Maths* **11**, 61–75.

SLATTERY, J. C. 1981 *Momentum, Energy, and Mass Transfer in Continua*, 2nd edn. Huntington: Robert E. Kreiger.

SOKOLOVSKII, V. V. 1965 *Statics of Granular Media.* Pergamon.

SPENCER, A. J. M. 1982 Deformation of an ideal granular material. In *Mechanics of Solids* (ed. H. G. Hopkins & M. J. Sewell), pp. 607–652. Pergamon.

SPINK, C. D. & NEDDERMAN, R. M. 1978 Gravity discharge rate of fine particles from hoppers. *Powder Technol.* **21**, 245–261.

STROUD, M. A. 1971 The behaviour of sand at low stress levels in the simple shear apparatus. Ph.D. thesis, University of Cambridge.

SUNDARAM, V. & COWIN, S. C. 1979 A reassessment of static bin pressure experiments. *Powder Technol.* **22**, 23–32.

TÜZÜN, U., ADAMS, M. J. & BRISCOE, B. J. 1988 An interface dilation model for the prediction of wall friction in a particulate bed. *Chem. Engng Sci.* **43**, 1083–1098.

TÜZÜN, U., HOULSBY, G. T., NEDDERMAN, R. M. & SAVAGE, S. B. 1982 The flow of granular materials – II. *Chem. Engng Sci.* **37**, 1691–1709.

TÜZÜN, U. & NEDDERMAN, R. M. 1979 Experimental evidence supporting kinematic modelling of the flow of granular media in the absence of air drag. *Powder Technol.* **24**, 257–266.

TÜZÜN, U. & NEDDERMAN, R. M. 1982 An investigation of the flow boundary during steady-state discharge from a funnel flow bunker. *Powder Technol.* **31**, 27–43.

TÜZÜN, U. & NEDDERMAN, R. M. 1985 Gravity flow of granular materials round obstacles – II. *Chem. Engng Sci.* **40**, 337–351.

VAN ZUILICHEM, D. J., VAN EGMOND, N. D. & SWART, J. G. DE 1974 Density behaviour of flowing granular material. *Powder Technol.* **10**, 161–169.

VILLADSEN, J. & MICHELSEN, M. L. 1978 *Solution of Differential Equation Models by Polynomial Approximation.* Prentice-Hall.

WALKER, D. M. 1966 An approximate theory for pressures and arching in hoppers. *Chem. Engng Sci.* **21**, 975–997.

WALTERS, J. K. 1973 A theoretical analysis of stresses in axially-symmetric hoppers and bunkers. *Chem. Engng Sci.* **28**, 779–789.

WILLIAMS, J. C. 1977 The rate of discharge of coarse granular materials from conical mass flow hoppers. *Chem. Engng Sci.* **32**, 247–255.

WILMS, H. & SCHWEDES, J. 1985 Analysis of the active stress field in hoppers. *Powder Technol.* **42**, 15–25.

ZIENKIEWICZ, O. C., HUMPHESON, C. & LEWIS, R. W. 1977 A unified approach to soil mechanics problems (including plasticity and visco-plasticity). In *Finite Elements in Geomechanics* (ed. G. Gudehus), pp. 151–177. John Wiley.

ZUCROW, M. J. & HOFFMAN, J. D. 1976 *Gas Dynamics*, Vol. 2. John Wiley.